

University of Texas at Arlington

MavMatrix

Mechanical and Aerospace Engineering
Dissertations

Mechanical and Aerospace Engineering
Department

2022

Characterization of Fatigue Strength of Additively Manufactured Ti-6Al-4V with Recoater Blade Interference Flaws and Residual Stresses Towards an Enhanced Fatigue Substantiation Methodology for Aerospace Structures Applications

Joshua Manyara Mochache

Follow this and additional works at: https://mavmatrix.uta.edu/mechaerospace_dissertations



Part of the [Aerospace Engineering Commons](#), and the [Mechanical Engineering Commons](#)

Recommended Citation

Mochache, Joshua Manyara, "Characterization of Fatigue Strength of Additively Manufactured Ti-6Al-4V with Recoater Blade Interference Flaws and Residual Stresses Towards an Enhanced Fatigue Substantiation Methodology for Aerospace Structures Applications" (2022). *Mechanical and Aerospace Engineering Dissertations*. 279.

https://mavmatrix.uta.edu/mechaerospace_dissertations/279

This Dissertation is brought to you for free and open access by the Mechanical and Aerospace Engineering Department at MavMatrix. It has been accepted for inclusion in Mechanical and Aerospace Engineering Dissertations by an authorized administrator of MavMatrix. For more information, please contact leah.mccurdy@uta.edu, erica.rousseau@uta.edu, vanessa.garrett@uta.edu.

**Characterization of Fatigue Strength of Additively Manufactured Ti-6Al-4V with Recoater
Blade Interference Flaws and Residual Stresses Towards an Enhanced Fatigue
Substantiation Methodology for Aerospace Structures Applications**

DISSERTATION

by

Joshua Manyara Mochache

Submitted in partial fulfillment of the requirements for the degree of

Doctor of Philosophy, Aerospace Engineering

Mechanical and Aerospace Engineering Department
University of Texas at Arlington

August 2022

Committee

Dr. Robert Taylor (Committee Chair and Supervisor, UTA MAE Faculty)

Dr. Kamesh Subbarao (Committee member and Graduate Advisor, UTA MAE Faculty)

Dr. Ameri Amir (Committee member, UTA MAE Faculty)

Dr. Haiying Huang (Committee member, UTA MAE Faculty)

Dr. Yiran Yang (Committee member, UTA IMSE Faculty)

© Joshua Mochache 2022

All Rights Reserved



Acknowledgements

I begin with thanks to God, for according me an opportunity to reach this important milestone in life. I am dearly grateful to my family: my wife, Dr. Tankiso Mochache, my children, Maxwell and Marion, and my Parents, the Mochaches of Nyansiongo, Kenya, for enabling, supporting, and standing by me to through this pursuit of knowledge, unto attainment of this dream.

I am very grateful to my Supervisor, Dr. Robert Taylor, for guiding me along this academic journey. Indeed without his introduction of the subject of additive manufacturing when I undertook his graduate class at UTA, and the further discussions shared based on his and my similar industry experience, he as a structural engineer at Lockheed Martin among his other aerospace industry experiences shared, together with his on-going research in developing methods to substantiate additively manufactured structural parts, none of these studies would have been initiated. Dr. Taylor also introduced me to AADFW Laboratory, where I was able to work with their technical lead, Mr. Jeremy Wilson, to complete static and fatigue tests, and to perform microstructure analysis. I am extremely indebted to AADFW's support.

I wish to further acknowledge the support of other members of my supervising committee, to include Dr. Amir Ameri and his PhD. students (Bharat and Behzad) at the UTA Metal AM lab, for all their support in helping me with the specimen builds using UTA's EOS M290 machine, and subsequent reviews and discussions held on the same. Much gratitude as well to Dr. Haiying Huang, the fatigue and damage tolerance faculty expert at UTA, for her valuable insights as well as to Dr. Yiran Yang of UTA's Industrial Engineering and Systems Engineering, for her timely and practical applicability lessons on the additive manufacturing process.

Finally, I would like to acknowledge my employer, Bell Flight Textron Inc., for financially supporting my educational journey as well as providing the background through the work I am

currently involved in daily with fatigue and damage tolerance (F&DT) analysis, and the support of my fellow co-workers. I want to especially recognize Dr. Xiaoming Li, the F&DT Technical Fellow at Bell, Mr. Alejandro Barbarin the F&DT Manager of the Bell 525 project that I am currently supporting, and the F&DT Technical Lead Mr. Paul Green, all of whom have been very supportive and taken their time to review my presentations and manuscripts, providing me valuable insights. I also want to recall the support of former Bell colleagues whom, early on, provided me significant contributions; these are Dr. Bogdan Krasnowski and Dr. Didier Duprat, who's works I have referenced in this study – I am forever grateful to their advice along my personal, academic, and professional journey.

Dedication

To my children Maxwell and Marion

May you forever shine!

Abstract

This research characterized the fatigue strength of additively manufactured (AM) Ti-6Al-4V, through fatigue and static tests conducted using specimens with and without recoater blade interference flaws (RBIF), and thus further enhanced the fatigue substantiation methodology for AM parts by using combined fatigue strength knock-down-factors (KDF) developed from this study. Qualification and certification (Q&C) of metallic AM parts, through acceptable methods for fatigue and damage tolerance (F&DT) substantiation, is an area where significant gaps still exist. While progress has been made in design as well as materials and process standardization, Q&C of additively manufactured metallic structural parts, especially those in civil aviation certification termed Principal Structural Elements (PSEs), failure of which is catastrophic, remains the holy grail in aerospace AM application. By characterizing the effects of the mechanically induced RBIF to metallic Laser Powder Bed Fusion (L-PBF) Ti-6Al-4V built parts, and further combining this fatigue strength reduction to include residual stresses, indicates a sufficiently conservative approach while continuing to minimize highlighted causes of RBIF which include: the type of recoater blade used, the aspect ratio of the parts built, optimal use of support structures in heat dissipation and distortion control, layout of the parts on the build plate, and blade interference control settings. Indeed, while RBIF was shown to occur to varying degrees commonly in most metallic AM builds, no specific studies have previously been undertaken to characterize its effect on the fatigue strength of Ti-6Al-4V. Further, the structural integrity assurance baked into the proposed fatigue methodology enhancement presented, where the use of this example Ti-6Al-4V Soderberg characterized with a fatigue KDF for RBIF in combination with the KDF for induced residual stress, will ensure that probabilities of combined worst case mechanical flaws and a heat treatment failures at a critical crack initiation site (CIS), can be

considered extremely remote, and thus this is representative of a *worst-case* effect. Future validation studies propose building full-scale parts in aerospace applications which verify the adequacy of the fatigue margins in the analytical predictions using the proposed enhanced methodology with combined RBIF and residual stress KDFs against full-scale test failure data.

TABLE OF CONTENTS

Acknowledgements	iii
Dedication.....	v
Abstract.....	vi
TABLE OF CONTENTS	viii
LIST OF FIGURES	x
LIST OF TABLES.....	xii
1 Introduction.....	14
1.1 Objective	14
1.2 Motivation	14
1.3 Approach.....	18
2 Background.....	19
2.1 Metal Additive Manufacturing	19
2.1.1 Powder Bed Fusion (PBF) Process	20
2.1.1.1 Laser Powder Bed Fusion (L-PBF) Process	21
2.1.1.1.1 Materials and Process Standardization for L-PBF.....	29
2.1.1.1.2 Design Standardization for L-PBF Process	32
2.1.1.1.3 Review of L-PBF Process Defects	33
2.1.2 Electron Beam Powder Bed Fusion (EB-PBF) Process.....	41
2.1.3 Directed Energy Deposition (DED) Process.....	43
2.1.4 Ultrasonic Additive Manufacturing (UAM) Process	44
2.2 Fatigue and Damage Tolerance Substantiation of Aerospace Structures	45
2.2.1 Classification of Aerospace Critical Structural Parts	48
2.2.2 Fatigue and Damage Tolerance Substantiation Requirements for PSEs.....	49
2.2.2.1 The Rule	50
2.2.2.2 Methods of Compliance for Metallic Structure F&DT Substantiation.....	51
2.2.2.2.1 Crack Initiation Methods (Safe Life) Analysis of AM Metallic Parts	53
2.2.2.2.1.1 Knock-Down-Factors (KDF) based approaches.....	54
2.2.2.2.1.2 Building Block Approach for AM.....	59
2.2.2.2.1.3 Safe Life Inspection for Failed Element.....	61
2.2.2.2.2 Crack Growth Methods for Analysis of Metallic Structures	62
2.2.2.2.2.1 Crack Growth Analysis using Defect modeling	63
2.2.2.2.2.2 Probabilistic Fracture Mechanics Approach.....	66
2.2.2.2.2.3 NDE, Structural Health Monitoring and In-Situ Monitoring Approaches.....	68
3 Methodology Enhancement	71
3.1 Baseline Deterministic Crack Initiation Analysis.....	73
3.2 Enhanced Deterministic Crack Initiation Analysis.....	79
4 Research Test and Data Collection	85
4.1 Project Outline and Execution.....	85
4.1.1 Baseline Specimens Build and Test	87
4.1.2 Flawed Specimens Build and Test.....	89
4.2 Stress and Fracture Failure Location Prediction.....	91
5 Results and Discussion	96
5.1 Results	96
5.1.1 Static Test Results.....	96
5.1.2 Baseline Specimen Fatigue Test Results	97
5.1.3 Flaw Specimen Fatigue Test Results	99
5.2 Discussion	101
5.2.1 Static Strength Results Review.....	101
5.2.2 Soderberg comparison	108
5.3 Fractography.....	111

6 Conclusion 122
6.1 Recommendations 122
6.2 Future work 124
LIST OF REFERENCES 125
Appendix A – Static Test Result Certificate A-131
Appendix B – Fatigue Test Result Certificate A-132

LIST OF FIGURES

Figure 1. Roadmap to achieving structural substantiation of metallic AM critical parts (PSEs/LLPs) [10]	15
Figure 2. Titanium Alloys in Use in an Aerospace Structures Application [144]	17
Figure 3. Metal Additive Manufacturing Technology categories	20
Figure 4. Typical Laser Powder Bed Fusion Process [123]	22
Figure 5. Key steps of the Laser Powder Bed Fusion (L-PBF) Process	22
Figure 6. L-PBF pre-process steps illustrated using EOS equipment [145]	24
Figure 7. Scan velocity vs laser power in Ti-6Al-4V L-PBF [129]	27
Figure 8. Design, Material and Process factors affecting L-PBF Part Quality [129]	32
Figure 9. Illustration of Recoater Blade Interference in a Part (a) and Simulation of Distortion using Netfabb® Simulation [138]	36
Figure 10. Positioning Parts on Build Platform to Prevent RBIF [123]	39
Figure 11. Low Aspect Ratio versus High Aspect Ratio Parts	40
Figure 12. EB-PBF schematic (courtesy GE Additive [5])	42
Figure 13. Schematics of two DED systems (A) uses laser together with powder feedstock and (B) uses electron beam and wire feedstock [131]	44
Figure 14. Ultrasonic Additive Manufacturing Process [133]	45
Figure 15. GE LEAPT TM Engine Nozzle made by Metal L-PBF Process [5]	47
Figure 16. Part Classification (courtesy NASA MSFC [17])	55
Figure 17. Schematic Diagram of Building Block Tests for a Fixed Wing [44]	60
Figure 18. SMART DT Schematic – (Courtesy – Ocampo et. al) [64]	67
Figure 19. Elements of a Safe-Life (Crack Initiation) Analysis [22]	74
Figure 20. Typical S-N curve for Safe Life (Crack Initiation) Evaluation [22]	76
Figure 21. Soderberg Method for Safe-Life (Crack Initiation) Evaluation [22]	78
Figure 22. Normal distribution, mean, and standard deviation	80
Figure 23. Key inputs to F&DT evaluation and effects of Metal AM	80
Figure 24. Combining Material Strength and Load PDF distributions [139]	81
Figure 25. Overall dimensions of Ti-6Al-4V Specimens made using EOS M290	86
Figure 26. Initial Layout of Specimens in Build Chamber	87
Figure 27. Baseline specimen lineup orientation on build plate versus recoater blade	89
Figure 28. As-built test specimens with Recoater Blade Interference Flaws (RBIF)	90
Figure 29. Tolerance setting and high aspect ratio challenge with RBIF	90
Figure 30. FEM Geometry and Modeling of the RBIFs	92
Figure 31. State of Stress in Test Specimens using Cylindrical Coordinates	92
Figure 32. Fatigue Test Specimen with Recoater Blade Interference Flaw (RBIF)	94
Figure 33. FEM showing Increased Mesh Density in Center (Flaw) Section	94
Figure 34. FEM Results at the highest stressed RBIF (Location A)	95
Figure 35. Baseline, Ti-64 Grade 5, As-Built, No-RBIF, with Residual Stress, R=0.1, Maximum Stress (MPa)	98
Figure 36. Baseline, Ti-64 Grade 5, As-Built, No-RBIF, with Residual Stress, R=0.1, Oscillatory Stress (MPa)	98

Figure 37. Fatigue Test Results of Ti-64 Grade 5 with RBIF and Residual Stress, R=0.1, Maximum Stress (MPa)	99
Figure 38. Fatigue Test Results of Ti-64 Grade 5 with RBIF and Residual Stress, R=0.1, Oscillatory Stress (MPa)	100
Figure 39. Fatigue Test Results of Ti-6Al-4V with Baseline and RBIF, R=0.1, Max Stressed	103
Figure 40. Fatigue Test Results of Ti-6Al-4V with Baseline and RBIF, R=0.1, Osc. Stress	104
Figure 41. Ti-6Al-4V L-PBF Fatigue Test Results for as-built specimens at R=0.1, Stress Relieved at 650°C for 3 hours [6]	105
Figure 42. Ti-6Al-4V L-PBF Fatigue Test Results for Polished Surface specimens at R=0.1, Stress Relieved at 650°C for 3 hours [6]	105
Figure 43. Fatigue Test Results comparison of current testing and Ref [6] as-built stress relieved specimens, max stress at R=0.1	106
Figure 44. Wrought Ti-6Al-4V Annealed, smooth specimens (Kt =1.0) [100]	107
Figure 45. Test Results S-N comparisons Ti-6Al-4V annealed bar per AMS4928 vs L- BPF with residual stress	107
Figure 46. Soderberg plot showing values required from Static and Fatigue test results	108
Figure 47. Soderberg plot showing Static and Fatigue test results of RBIF effect	109
Figure 48. Soderberg of the Ti-6Al-4V by L-PBF with residual stress and RBIF	110
Figure 49. Fracture Surface Photographs baseline fatigue specimens analyzed for fracture surface	111
Figure 50. Fracture surface study of Baseline Specimen 2 ~10X Magnification	112
Figure 51. Fracture Surface Photograph of Baseline Specimen 3 ~10X Magnification	113
Figure 52. Fracture Surface Photograph of Baseline Specimen 4 ~10X Magnification	113
Figure 53. Fracture Surface Photographs of RBIF Specimens 1, 3, 4 and 5	114
Figure 54. Fracture Surface Photograph of RBIF Specimens 1 ~10X Magnification	115
Figure 55. Fracture Surface Photograph of RBIF Specimens 3 ~10X Magnification	116
Figure 56. Fracture Surface Photograph of RBIF Specimens 4 ~10X Magnification	116
Figure 57. Fracture Surface Photograph of RBIF Specimens 5 ~10X Magnification	117
Figure 58. JEOL JSM-5410 SEM used for Microstructure studies	117
Figure 59. SEM photographs of fracture surface of RBIF Specimen 3	118
Figure 60. SEM cross-sectional view oriented in Y-Z plane showing grain boundaries	120

LIST OF TABLES

Table 1. Standards and Specification for Materials, Process and Design of Metal AM.....	31
Table 2. Assessment Criteria to Determine Structural Demand [17]	49
Table 3. Crack Phases and F&DT Analysis Type	52
Table 4. F&DT Methods of Compliance discussed in AC29-2C [19]	53
Table 5. Hazard Classification and Design Assurance Level, PoF per Flight Hour [47]	56
Table 6. Project Outline and Task Descriptions	86
Table 7. Build specification for baseline	88
Table 8. Static Test Results for Ti-6Al-4V Baseline (NF) and RBIF (F) Specimens	96
Table 9. Fatigue Test Results for Baseline Ti-6Al-4V Specimens.....	97
Table 10. Fatigue Test Results for Ti-6Al-4V Specimens with RBIF.....	99
Table 11. Review of Static Test Results for Ti-6Al-4V L-PBF	101
Table 12. Table of Static Parameter Results From Comparable Data [6]	102
Table 13. Summary of KDF Calculations for Various Combination Effects for L-PBF Processed Ti-6Al-4V	110
Table 14. EOS Titanium Ti64 Grade 5 Chemical Composition [135]	119

LIST OF ABBREVIATIONS

<i>F&DT</i>	=	Fatigue and Damage Tolerance
<i>RBIF</i>	=	Recoater Blade Interference Flaw(s)
<i>FAA</i>	=	Federal Aviation Administration
<i>AM</i>	=	Additive Manufacturing
<i>AC</i>	=	Advisory Circular
<i>Q&C</i>	=	Qualification and Certification
<i>EASA</i>	=	European Aviation Safety Administration
<i>PSE</i>	=	Principal Structural Element
<i>NASA</i>	=	National Aeronautical Space Administration
<i>PDF</i>	=	Probability Density Function
<i>MSFC</i>	=	Marshall Space Flight Center
<i>LLP</i>	=	Limited Life Parts
<i>MAE</i>	=	Mechanical and Aerospace Engineering
<i>FC</i>	=	Fatigue Critical
<i>NIST</i>	=	National Institute of Standards & Technology
<i>EBAM</i>	=	Electron Beam Additive Manufacturing
<i>AWS</i>	=	American Welding Society
<i>LBAM</i>	=	Laser Based Additive Manufacturing
<i>ASIP</i>	=	Aircraft Structural Integrity Program
<i>CIS</i>	=	Crack Initiation Site
<i>L-PBF</i>	=	Laser Powder Bed Fusion
<i>HCF</i>	=	High Cycle Fatigue
<i>UAM</i>	=	Ultrasonic Based Additive Manufacturing
<i>LCF</i>	=	Low Cycle Fatigue
<i>CAD</i>	=	Computer Aided Design
<i>FCG</i>	=	Fatigue Crack Growth
<i>CFR</i>	=	Code of Federal Regulations
<i>GAG</i>	=	Ground-Air-Ground
<i>PoF</i>	=	Probability of Failure
<i>SDO</i>	=	Standardization Organization
<i>N</i>	=	Number of Cycles to failure at Stress level
<i>S_E</i>	=	Maximum oscillatory or alternating stress for “infinite” number of cycles
<i>K_T</i>	=	Stress concentration factor
<i>K_F</i>	=	Notch factor
<i>LEFM</i>	=	Linear Elastic Fracture Mechanics
<i>EOS</i>	=	Electro Optical Systems GmbH
<i>UTA</i>	=	University of Texas at Arlington
<i>EDM</i>	=	Electrical Discharge Machining
<i>LENS</i>	=	Laser Engineered Net Shaping
<i>DLF</i>	=	Directed Light Fabrication
<i>DMD</i>	=	Direct Metal Deposition
<i>LBMD</i>	=	Laser-Based Metal Deposition
<i>LFF</i>	=	Laser Freeform Fabrication
<i>LDC</i>	=	Laser Direct Casting
<i>CDF</i>	=	Clearly Detectable Flaws
<i>BDF</i>	=	Barely Detectable Flaws
<i>SEM</i>	=	Scanning Electron Microscope

1 Introduction

1.1 Objective

The goal of this research was to characterize the fatigue strength of additively manufactured (AM) Ti-6Al-4V, with and without recoater blade interference flaws (RBIF), and to further enhance the fatigue substantiation methodology for AM parts by proposing use of combined fatigue strength knock-down-factors (KDF), and other structural reliability enhancements developed from this study. Ultimately, this research aims at enhancing capabilities to perform fatigue and damage tolerance (F&DT) substantiation analysis of critical structural aerospace metallic AM parts, beginning here with those produced using Ti64 Grade 5 powder and the EOS M290 laser powder bed fusion (L-PBF) process, an area where such progress is highly desired.

1.2 Motivation

Metal AM, a disruptive technology that is rapidly revolutionizing the design-build-manufacturing process in several industries, has the potential to make even greater inroads in the aerospace industry, if key hurdles to its use for critical structural applications, especially those known in civil certification as Principal Structural Elements (PSEs), are resolved. A PSE is any structure that carries significant flight loads, failure of which is likely to result in catastrophic outcome preventing continued safe flight and landing [16]. As such, structural qualification and certification (Q&C) of such AM PSE structures is bound to face significant hurdles, to ensure the highest applicable standard of structural reliability. A key challenge identified in the review by Mochache et. al [1], was the need to develop acceptable fatigue strength material allowables that account for *effects-of-defects* encountered in the AM process, for use in structural substantiation specific to meeting the fatigue and damage tolerance (F&DT) requirements.

This study endeavors to make progress in this area, by characterizing the fatigue strength of AM Ti-6Al-4V with a unique and significant defect – the recoater blade interference flaw (RBIF) – combined with residual stresses. Attention to the need for enhancements in the structural substantiation methodologies and capabilities for Q&C of additively manufactured aerostructures was reviewed and highlighted by Mochache et al. [1], Ristori et al. [8], Taylor et al. [26], and Gorelik [10]. Indeed, the illustration in Figure 1 by the Federal Aviation Administration’s (FAA) Dr. Gorelik [10] summarizes the need and urgency to develop pathways towards substantiation of major and critical structural AM components (PSEs and Limited Life Parts - LLPs), within a reasonable timeframe.

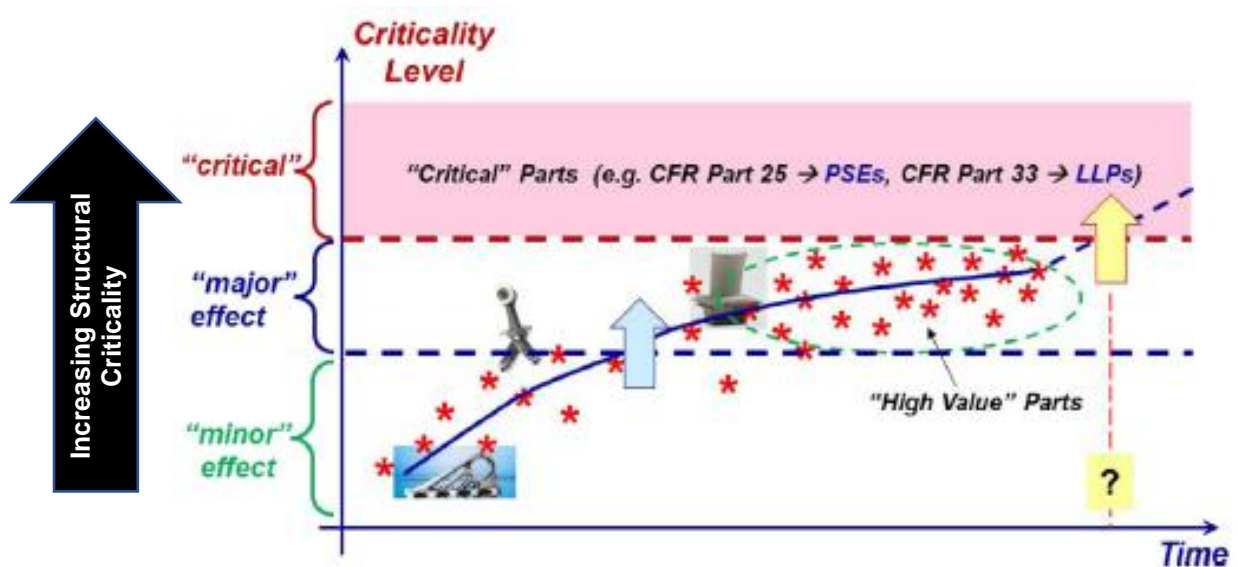


Figure 1. Roadmap to achieving structural substantiation of metallic AM critical parts (PSEs/LLPs) [10]

This underlines the significance and timeliness of this work. It seeks to make progress in a critical area of F&DT qualification of metallic additive manufacturing, while not diminishing daunting tasks that still lie ahead in achieving authority-acceptable approaches for F&DT Q&C of major and critical aerospace structural parts (PSEs/LLPs/FCs). It brings perspective to proposed

solutions to the F&DT substantiation challenge for AM metallic parts, unlocking potentially great opportunities ahead for the aerospace industry – perhaps even greater values than those already witnessed with the success of the AM metallic GE nozzle, which has now exceeded over 30,000 built [5].

There are several advantages of the AM build process over the traditional subtractive processes which can only be achieved over more aerospace products. The key advantages of the AM process over subtractive manufacturing processes (cutting, forming, casting) are below [2, 3]:

- Material: multiple material options to include polymeric materials, composites, metals, and ceramics.
- Speed: AM can fabricate in a single stage without the need for molds and dies thereby reducing production cycle time and consolidating the required manufacturing processes and equipment.
- Design freedom: The greater the geometric complexity, the greater the advantage. Due to the ability to manufacture unique shapes typically not possible with subtractive techniques, AM has a huge advantage over traditional fabrication methods.
- Application: AM offers high degrees of customization.
- Cost/Schedule savings: AM eliminates long lead time and delivery schedule costs associated with shipping parts globally (e.g. AM machines could easily be transported to various locations with the necessary powder stocks and parts needed say in the case of battlefield operations or out in space could be fabricated at the press of a button with the necessary CAD files).

- Green manufacturing: AM uses clean, nonpollution lasers as the energy resource, which are environmentally friendly. Since AM allows for the right material to be deposited at the right place, it is free from waste (green).

The focus of this study on Ti-6Al-4V alloy is because of its high-value for structural components primarily due to its favorable strength-to-weight ratio, superior corrosion resistance and excellent mechanical properties [100]. The aerospace industry accounts for most of the global titanium consumption – over 80%. Ti-6Al-4V is the most common Ti-alloy type used in the aerospace industry with main applications including building airframes, helicopter yokes and hub components, landing gears, low pressure compressor components and fan blades within gas turbine engines, and other increased uses of this alloy. For example, on a Boeing 777 aircraft, Titanium alloys account for over 15% of its total weight, Figure 2 [144].

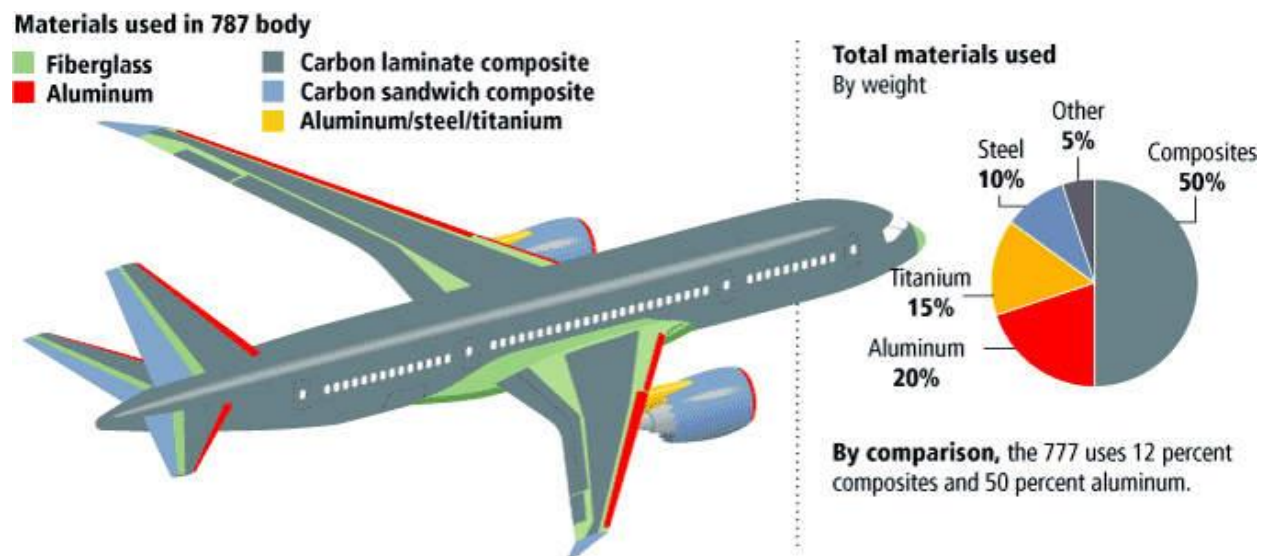


Figure 2. Titanium Alloys in Use in an Aerospace Structures Application [144]

1.3 Approach

The approach for this research involved design and manufacturing of test specimens, empirical methods for testing and analyzing the data as well as a technical review of literature, and cumulative engineering study and experience in aerospace structures analysis and additive manufacturing disciplines. The study began with an initial review of metal AM particularly the laser powder bed fusion (L-PBF) process. This study highlighted the various types of defects associated with this process prior to diving deeply into the surface defects resulting in the most significant fatigue strength reductions. The study then addressed aerospace fatigue and damage tolerance (F&DT) substantiation requirements for metallic structures, beginning with an in-depth review conducted by Mochache et. al [1], which highlighted the existing gaps in the current methodologies. The research then focused on the deterministic crack initiation approaches where gaps exist in development of knock down factors (KDF) especially those associated with the effects of defects resulting in potentially significant reductions in fatigue strength and proceeded to provide an enhanced methodology approach that combined the KDF associated with residual stresses and recoater blade interference flaws (RBIF), among other structural reliability enhancements proposed.

It concluded with generating test data, analyzing and discussing finding on the specimens with and without the RBIF and inclusive of residual stress. It also compared results without RBIF and other data inclusive of stress relief. A discussion on the results of the testing was presented in form of S-N plots and Soderberg and provided recommendations for fatigue strength KDFs for the RBIF surface flaw and residual stresses in Ti-6Al-4V Grade 5 developed through this testing.

Future work proposed includes full scale validations that test parts purpose-built for aerospace applications against the coupon-based data and proposed methodology enhancements.

2 Background

This section provides a background of metal AM process, providing a brief history of the evolution of this process, as well as defining the overall classifications of metal AM and in-depth review of the Laser-Powder Bed Fusion (L-PBF) process inclusive of a review on the various defects associated with the L-PBF process before proceeding to detail the state of design, materials and process standardization for this L-PBF process. Finally a review of various approaches to F&DT substantiation concludes, with a summary of challenges and gaps associated with each approach.

2.1 Metal Additive Manufacturing

Metal AM is the process by which metallic structures are manufactured through an additive process that combines metal particles layer-by-layer compared to the traditional subtractive metal processing methods such as CNC machining [1]. Metal AM has undergone tremendous advances over the last two decades. The earliest version of metal AM was introduced by RapidSteel™ in 1996 and utilized a liquid phase sintering process consisting of a thermoplastic binder coated 1080 carbon steel powder with copper as an infiltrant. These metal AM technologies have evolved rapidly to the ones that are currently used to produce full-scale functional parts. The current metal additive manufacturing technologies most often used are categorized under three main groupings by the manufacturing process employed as shown in Figure 3: Powder Bed Fusion (PBF), Directed Energy Deposition (DED) and Ultrasonic Additive Manufacturing (UAM) [2, 3].

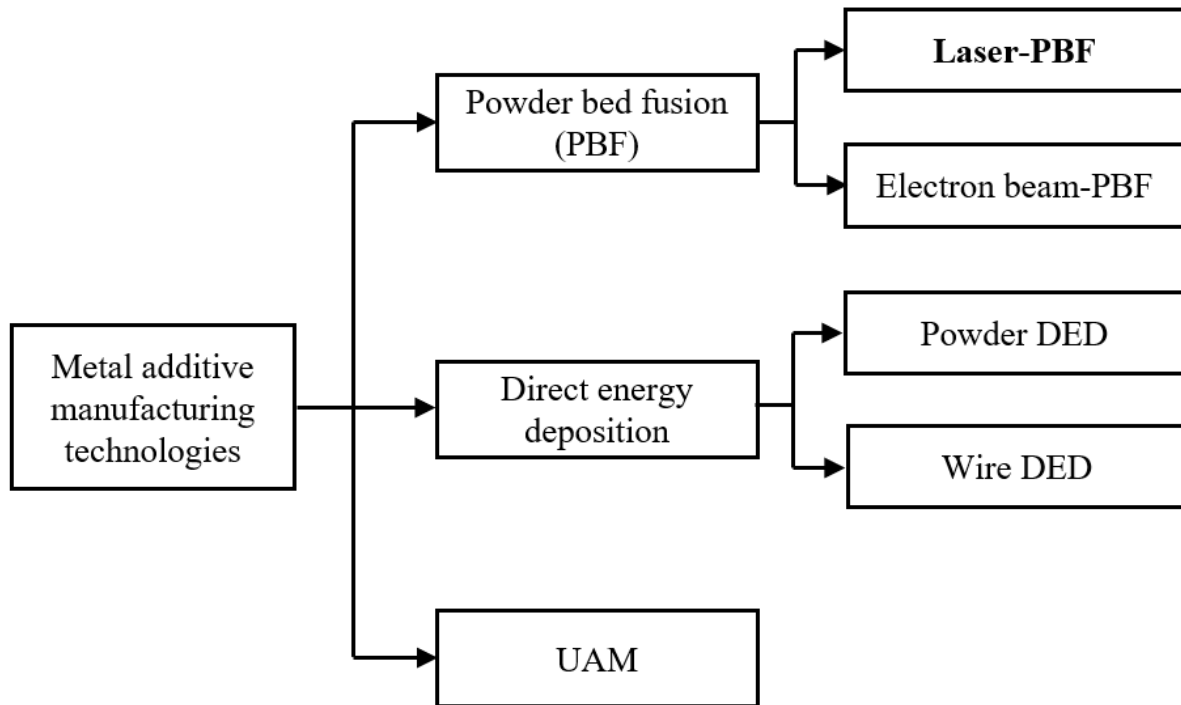


Figure 3. Metal Additive Manufacturing Technology categories

2.1.1 Powder Bed Fusion (PBF) Process

The powder bed fusion (PBF) processes were among the first to be commercialized. Beginning with the selective laser sintering (SLS) method (primarily for non-metals), the first commercialized PBF process was developed at the University of Texas at Austin, USA [1]. Metal powder bed fusion research in the late 1980s and early 1990s by various research groups was mostly unsuccessful primarily because metals have high thermal conductivity, high surface tension and high reflectivity making them significantly more difficult to process than polymers.

All PBF processes share certain basic sets of characteristics which include: a thermal source for inducing fusion between powder particles, a method for controlling powder fusion to a prescribed region of each layer and a mechanism for adding and smoothing powder layers. PBF remains the most dominant method of all the AM processes [3] and through modification of the initial

approaches that involve partial melting of the powder (sintering), applications now involving full melting by the Laser Powder Bed Fusion process (L-PBF) and the Electron-Beam Powder Bed Fusion process (EB-PBF) have been made possible.

2.1.1.1 Laser Powder Bed Fusion (L-PBF) Process

This study's focus was on the L-PBF process, which employs the full melting process using laser beam energy most associated with processing of engineering metal alloys [124]. It is one where the entire region of material is subjected to impinging heat energy which melts it to a depth exceeding the layer thickness. The L-PBF process is illustrated in Figure 4 [122]. The first commercial successes for metal L-PBF systems were developed by the Fraunhofer Institute for Laser Technology in Germany [1]. Their research developed the basic processing techniques necessary for successful laser-based, point-wise melting of metals and the use of lasers with wavelengths better tuned to the absorptivity of metal powders.

Several companies make commercially available L-PBF systems for direct melting of metals to include EOS (Germany), Reishaw (UK), Concept Laser (Germany), Selective Laser Melting (SLM) Solutions (Germany), Arcam AB (Sweden), Realizer (Germany) and 3D Systems (France/USA). Several of these companies have over the last few years been acquired by USA-based General Electric (GE) and are now part of GE Additive (USA). This is the process by which the specimens built for this study, using the EOS[®] M290 machine, employed. It is typically divided into five key steps with an iteration occurring between steps 2 and 4 until the build is complete as shown in Figure 5.

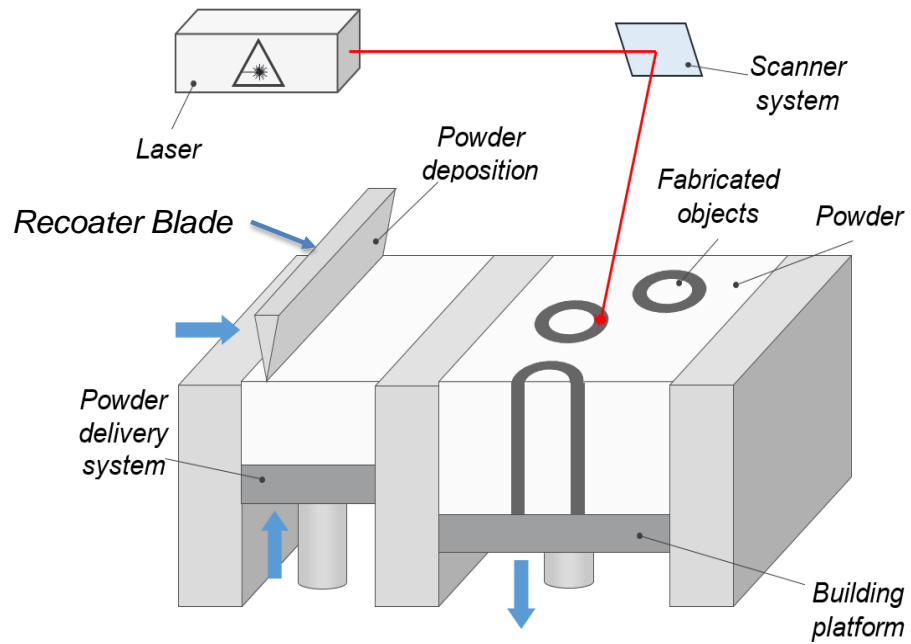


Figure 4. Typical Laser Powder Bed Fusion Process [123]

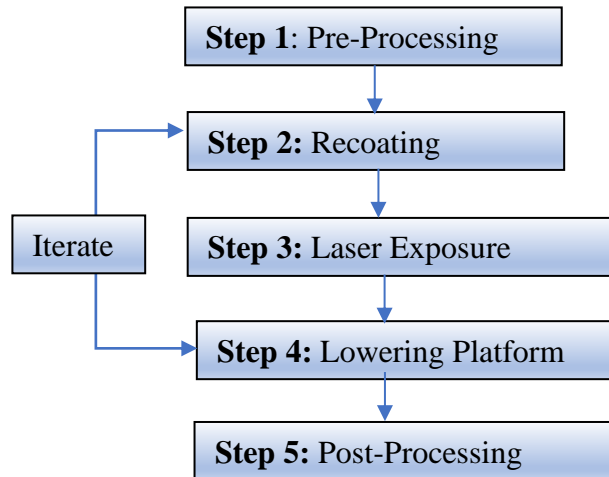


Figure 5. Key steps of the Laser Powder Bed Fusion (L-PBF) Process

Step 1. Pre-processing: As illustrated in Figure 6 [145], the first step in pre-processing begins with 3-dimensional Computer Aided Design (CAD) models in compatible format (typically .stl, .igs, .stp etc.) and converts the CAD file to a format used by the build machine, which in most cases is the STL format. A special software is used for the data preparation pre-processing step. For this project, the CAD files were converted using Materialise *Magics*[®] software. Other data preparation software includes ANSYS[®] Additive, Netfabb[®] Simulation and Siemens NX[®]. During this pre-processing step, this preparation software was used to analyze for potential building errors prior to conversion to the STL file type as well as virtually fitting the specimens to be built into the build chamber to optimize on the build arrangement. The order of the specimens, orientation relative to the recoater blade and other key features of the layout of the specimens have proven critical to avoiding interference with the recoater blade. Additionally, during the final pre-processing, using EOSPRINT, other optimal build parameters such as the overlap tolerance are entered to help eliminate interferences with the recoater blade, and work with the automatic collision detection to determine when to stop and continue a build following interference.

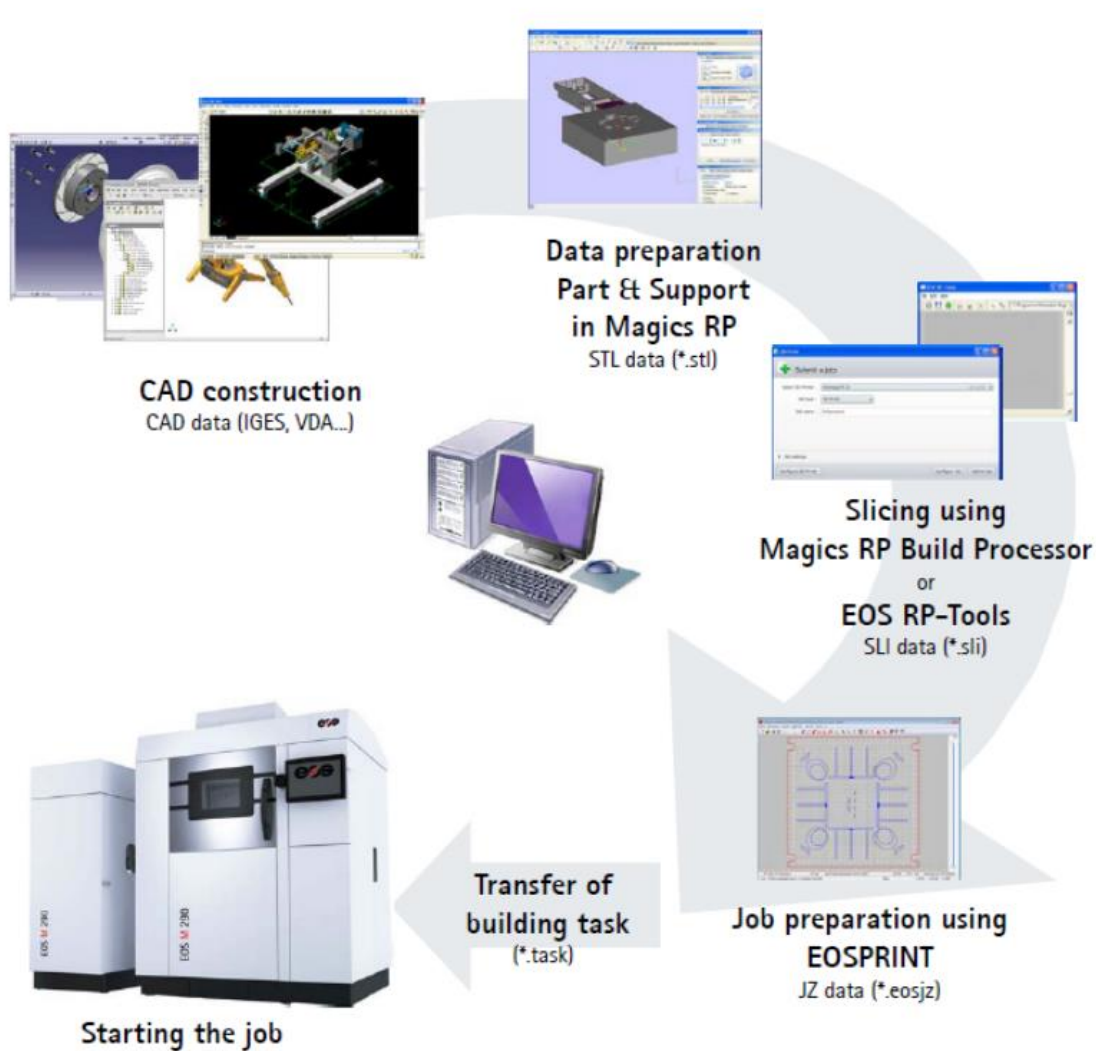


Figure 6. L-PBF pre-process steps illustrated using EOS equipment [145]

Other fundamental parameters [68] including build orientation, layer thickness, temperature setting among others critical to controlling F&DT strength characteristics, have been studied especially for this material alloy of study (Ti-6Al-4V). Understanding the effects of these fundamental parameters [68] have resulted in ways to identify and rank the most critical effects [106-112]. Among those identified for this study were build orientation (where specimens were built to be loaded along the Z-axis resulting in conservative F&DT knockdown factors relative to

other loading directions), as well as the build parameters chosen to result in large surface defects (interference flaws) which became crack initiation sites (CIS) for early fatigue failure conservatively covering other defects in Ti-6Al-4V [125, 126].

Step 2. Recoating: This step in the L-PBF process is critical, as it is primarily where the challenges addressed manifest. This is when the powder delivery system is used to appropriately get the right amount of powder spread on the build platform. Typically, this is done using a recoater blade that spreads the powder across from the powder delivery system side (on the left of the illustration in Figure 4) to the right of the build platform area. The thin powder layer (typically $< 100\mu\text{m}$) is applied to the build platform using different types of recoater blades depending on the setup of the machine. The EOS m290 used at the University of Texas Arlington for this study utilizes a hard recoater blade made from high strength (HS) steel. Other hard recoaters are made of ceramic. In comparison, a soft recoater blade, unlike the hard recoater blade, allows for some deformation of the blade as it travels across the build plate, may be made from silicon, rubber or soft carbon fiber [122]. Depending on several other setup options that will be elucidated on later, the operation of the recoating blade process to avoid interference with the build platform is key to ensuring the Recoater Blade Interference flaws (RBIF) are absent in a build. RBIF is classified as a type of surface roughness defect and can be seen in the example of the parts built for this study with this defect (see Figure 28). RBIF is created whenever the recoater collides with the build part. After this happens, depending on the settings in the software in terms of acceptable interference and the type of recoater blade (hard or soft), the build may stop or some of models may be dragged across the powder bed. Soft recoaters can be useful in avoiding RBIF especially when identical parts are printed on the same build platform [122]. If one part deforms or is not

built successfully, you have a high chance that all the other parts on the build plate will behave the same way, so then it may be preferable to stop the build in case of collision.

Step 3. Laser Exposure: The L-PBF process uses a high energy laser beam to impinge on the freshly laid powder layer to cause it to fuse to the previous layer below. Exposure is the energy per unit area. The energy density of the laser beam and the exposure period characterize the thermo-mechanical conditions which produce thermal gradients in the range of 5–20 K/μm and cooling rates in range 1–40 K/μs for Ti-6Al-4V L-PBF process [128]. This is where the fundamental L-PBF parameters of laser strength and scan speed are vital to the control of lack of fusion defects, balling and keyholing. Modeling of the thermodynamic-physics of the moving point-heat-source to characterize the melt pool formation and to determine the total amount of energy applied and absorbed by the powder bed as the laser passes, is complex, however several modeling tools are now available to support this including ANSYS Additive, and Netfabb Simulation. The simplified energy density equation was used [2] as a simple method for correlating input process parameters to the density and strength of produced parts, where applied energy density E_A (also known as the Andrews number) can be found using Equation 1 below:

$$E_A = P/(U \times SP) \quad (\text{Equation 1})$$

Where: P = Laser Power, U = Scan velocity and SP = Scan Spacing

From the above equation 1, build speed can be maximized by utilizing the fastest combination of laser power, scan rate and scan spacing for a desired part build. However, for metals, the balling defect – a phenomenon where a molten pool of metal is present on a powder bed - occurs when surface tension forces overcome a combination of dynamic fluid, gravitational and adhesion

forces. Balling is a significant issue for metal AM [2] hence track lengths and types, scan speed and laser power are important to control. Several studies on scan velocity vs. laser power have been conducted on steels but a recent study on Ti-6Al-4V [129] provides clear guidance, as shown in Figure 7, on the control of the parameters of scan speed to laser strength, so as to avoid significant defects resulting from over melting, balling effects, and incomplete melting (lack of fusion).

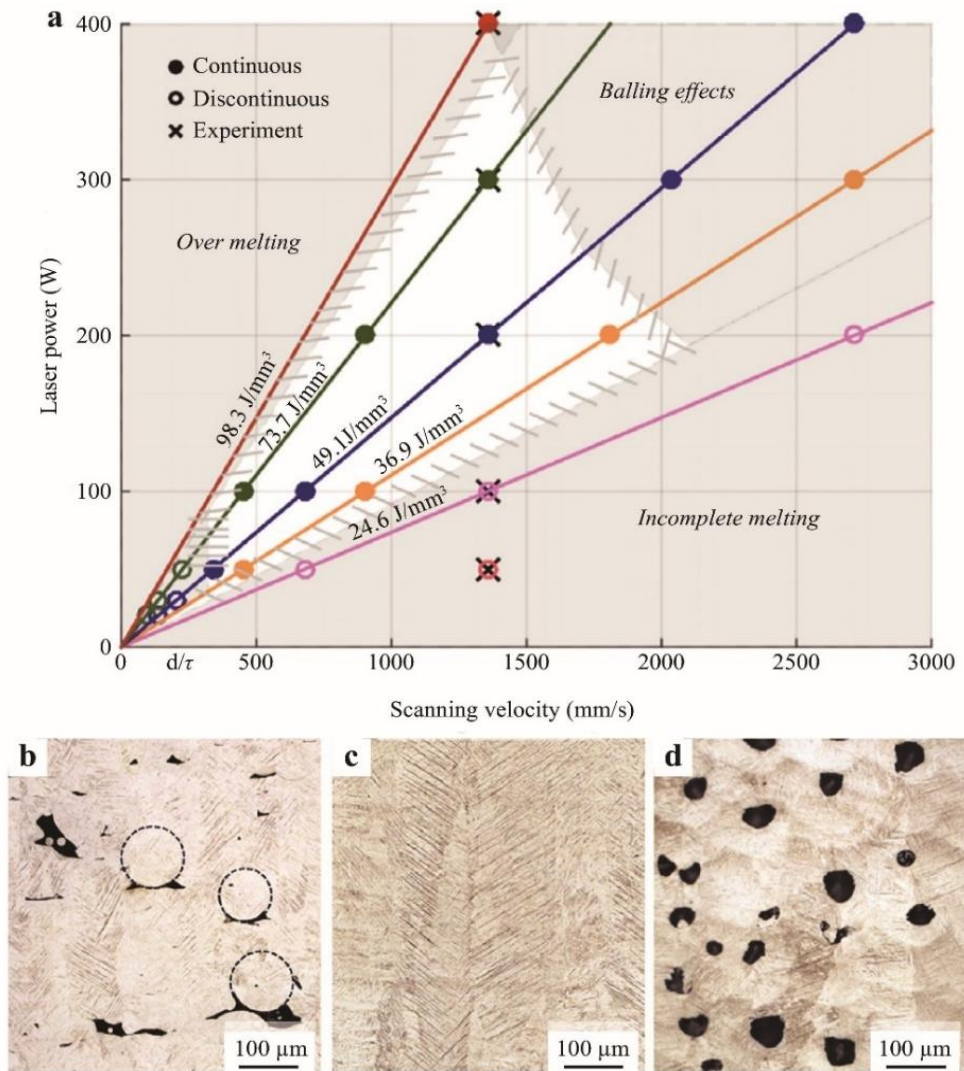


Figure 7. Scan velocity vs laser power in Ti-6Al-4V L-PBF [129]

Step 4. Lowering Platform: This is another critical step in the L-PBF build where the position of the build plate is moved down a certain predefined distance pre-programmed by process control inputs entered. This motion allows for the repeat of spreading of the material powder by the recoater blade to build up subsequent layers. Advances in computer-aided manufacturing (CAM) controls have allowed for very precise control of the build machine logic. Accurately controlling the position of the build platform increases the precision of the minimum layer thickness that can be produced with current machines capable of up to 10 μ m thick layers [129]. For this study at the University of Texas Arlington (UTA), the EOSPRINT software for the EOS m290 was pre-programmed for a minimum layer thickness of 40 μ m per layer, according to the machine capability for Ti64 Grade 5 [130].

Step 5. Post Processing: This post-processing step in the L-PBF process begins with the removal of the part from the built plate. Often to prevent distortion during the build, which is a primary cause of RBIF, a common practice is to ensure a robust and rigid support structure attaching the part being built to the build plate. These supports are removed during the post process using several methods such as: bandsaw, milling equipment or using Electrical Discharge Machining (EDM). For the specimens built for this study, a bandsaw was used to remove the specimens from the build plate as there was sufficient grip material at each end of the specimens. Another post-processing step is heat treatment. Depending on which material is used, this can have a significant impact on the resulting mechanical strength properties due to altering the microstructure. Additional post process treatment that has proven very beneficial in improving the mechanical properties of many materials especially Ti-6Al-4V is the Hot-Isostatic Press (HIP) post process treatment. HIPing subjects components to both elevated temperatures and gas pressure in a high-

pressure containment vessel. This helps to reduce or eliminate internal voids, porosity and micro shrinkage through a combination of plastic deformation, creep and diffusion bonding. The HIP process has been shown to improve several mechanical properties but especially fatigue and damage tolerance resistance [27, 28, 32, 33, 109].

2.1.1.1.1 Materials and Process Standardization for L-PBF

Material integrity standardization forms an integral part of ensuring mature, reliable, and repeatable product strength which is a crucial step in developing the certification criteria. Sources of variability in product strength include inconsistency in powder characteristics, process parameters used for fabrication, and variation within different L-PBF systems. Seifi et al. [8] comprehensively discussed the state of metal AM material qualification standards and summarized some of the essential standardization activities, as well as limitations associated with using currently available standards for metal AM. These AM material standards are identified as a precursor to the material characterization standards for any material system. Several SDOs have completed various AM materials and process standardization procedures [6]. The SAE International AMS-AM committee has set a high priority and goal for this effort. Indeed, an updated 2018 online SAE International brochure [26] quoted SAE AMS-AM committee chair, D. Abbott, stating:

“The industry consensus standards that SAE is generating through its AMS-AM committee greatly facilitate the implementation of additive manufacturing in the aerospace sector. By establishing the appropriate level of rigor and control, the specifications will ensure both quality and consistency in AM products and services.”

Table 1 lists some of the recently established standards and specification for metal additive manufacturing processes. As of May 2020, the SAE AMS-AM committees has so far released four new metal AM standards, SAE AMS-7000, 7001, 7002, and 7003 [65-67]. AMS-7003 is especially relevant to this study as it covers the laser powder bed fusion (L-PBF) process controls in detail [67]. AMS-7003, in combination with the groundbreaking document released by NASA MSFC, the MSFC-SPEC-3717 [16], provides standard practices for the L-PBF process that should set the proper trajectory towards industry-wide acceptance and mainstream protocols for certification of AM parts. NASA has given vendors for spacecraft hardware a framework within which they can supply metal AM per the guidelines [16, 42]. These will ensure minimal variability of acceptable end products. The NASA specification also points to additional SAE AMS-AM documents (see Table 3) which are set to also gain widespread use and acceptance throughout the aerospace industry. American welding society (AWS) released the D20.1/D20.1M [81] document in early 2019 that covers the general requirements for the metal AM components like design, inspection, and acceptance. This document also highlights the guidelines regarding the engineer and contractor interactions. The following committees, ASTM F42, ISO TC261, AWS D20, MSFC, and SAE AMS-AM, have been significant in establishing metal AM standards for the aerospace applications. The ASTM F42 committee is currently working on standard certification for additively manufactured Ti, Co, and Ni-alloys by powder-bed fusion. America Makes & ANSI Additive Manufacturing Standardization Collaborative (AMSC) released the 2nd version of ‘Standardization roadmap for additive manufacturing’ in mid-2018 [6]. This document provides an extensive review of the gaps in standardization/specification of the process, material, and design aspects of additive manufacturing.

Table 1. Standards and Specification for Materials, Process and Design of Metal AM

Reference Number	Organization/ Committee	Standards/Specification		
16	MSFC	MSFC-STD-3716	Standard for Additively Manufactured Spaceflight Hardware by Laser Powder Bed Fusion in Metals	Material and process
42	MSFC	MSFC-SPEC-3717	Specification for Control and Qualification of Laser Powder Bed Fusion Metallurgical Processes	
64	AMS AM Additive Manufacturing Metals	SAE AMS7000	Laser-Powder Bed Fusion (L-PBF) Produced Parts, Nickel Alloy, Corrosion and Heat-Resistant, 62Ni-21.5Cr-9.0Mo-3.65Nb Stress Relieved, Hot Isostatic Pressed and Solution Annealed.	
65	AMS AM Additive Manufacturing Metals	SAE AMS7001	Nickel Alloy, Corrosion and Heat-Resistant, Powder and Additive Manufacturing, 62Ni-21.5Cr-9.0Mo-3.65Nb	
66	AMS AM Additive Manufacturing Metals	SAE AMS7002	Process requirements for production of metal powder feedstock for use in additive manufacturing of aerospace parts.	
67	AMS AM Additive Manufacturing Metals	SAE AMS7003	Laser Powder Bed Fusion Process	
78	ISO/TC261 and ASTM F42	ISO/ASTM DIS 52907	Additive Manufacturing Technical Specifications on Metal Powder	
79	ASTM F42	ASTM WK55610 <i>(in work)</i>	New Test Methods for the Characterization of Powder Flow Properties for Additive Manufacturing Applications	
80	ASTM F42	ASTM WK55297 <i>(in work)</i>	New Guide for Additive Manufacturing – General Principles – Standard Test Artefacts for AM	
81	AWS	AWS D20.1/D20.1M	Standard for Fabrication of Metal Components using Additive Manufacturing	
82	ISO/TC 261 and ASTM F42	ISO/ASTM 52910-18	Additive manufacturing – Design – Requirements, guidelines, and recommendations	Design
83	ISO/TC 261	ISO 8887-1	Design for Manufacturing, Assembling, Disassembling and End-Of-Life Processing	
84	ISO/TC 261 and ASTM F42	ISO/ASTM NP 52916 <i>(in work)</i>	Additive manufacturing – Data formats – Standard specification for optimized medical image data	
85	ASME	ASME Y14.46	Product Definition for Additive Manufacturing	
86	ISO/TC 261 and ASTM F42	ISO/ASTM 52900	Additive manufacturing – General principles – Terminology	
87	ASTM F42	ASTM WK 54856 <i>(in work)</i>	New Guide for Principles of Design Rules in Additive Manufacturing	

2.1.1.1.2 Design Standardization for L-PBF Process

Part design and build orientation play a crucial role in the end-product quality of L-PBF parts. Figure 5 correlates L-PBF build quality, in the context of process-induced defects, with the process settings, material characteristics and geometric features via influential physical phenomenon predominant in the newly added layer [28]. L-PBF process-induced defects primarily include residual stresses, stress-induced deformation and cracks, surface roughness, porosity, and microstructural variations.

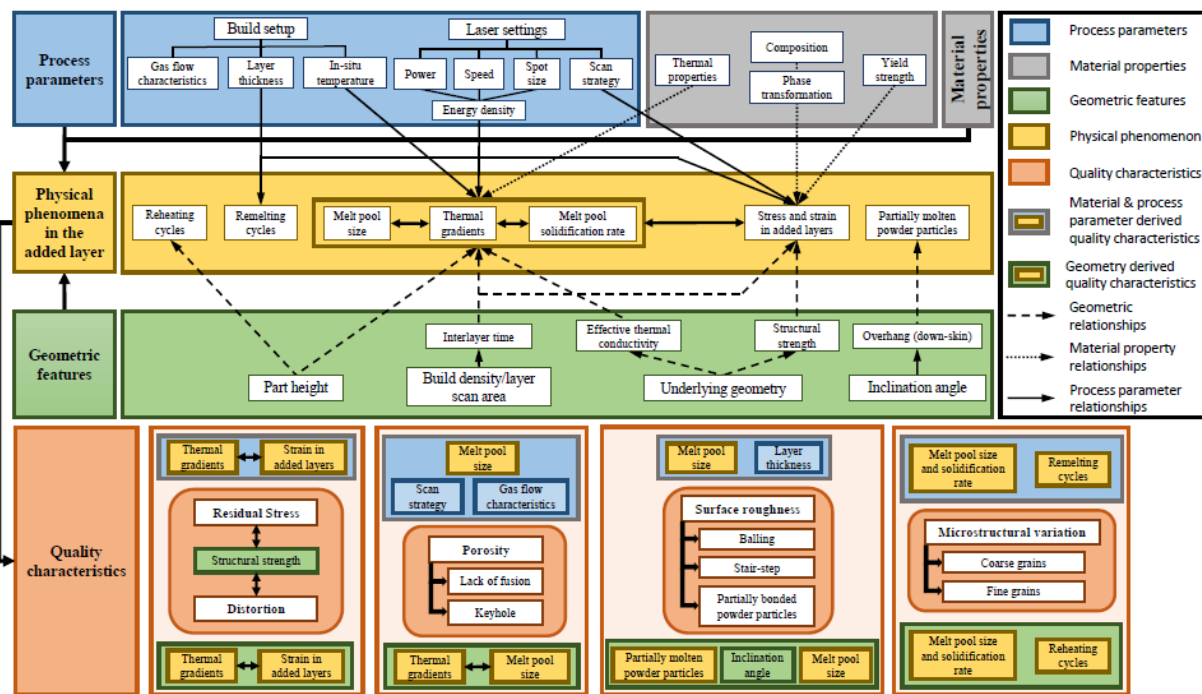


Figure 8. Design, Material and Process factors affecting L-PBF Part Quality [129]

Table 1 highlights some of the recently released design-related standards for additive manufacturing technology. A key highlight is the release of the L-PBF process-specific design guidelines/standards are yet to be announced, and much work remains. The standardization

roadmap for additive manufacturing [6] catalogues some of the critical gaps in design standards and specifications for L-PBF while crediting the joint ASTM F42 and ISO TC261 committee, and AWS for taking the lead in specifying design guidelines.

2.1.1.1.3 Review of L-PBF Process Defects

While the L-PBF process described above in detail above has matured significantly resulting in a thorough understanding of several causes and effects of various process parameters, and while a number of process standards for L-PBF have been recently released [65-68], never-the-less there still remain several potentially fatigue-strength limiting defects that need to be highlighted. Several studies have been, and continue to be undertaken, with goal of understanding the effects of defects associated with various L-PBF defects on fatigue strength. Some of the key defects that have been studied are listed below with a few of the key reference resources noted. The emphasis of this study is on the recoater blade interference flaw (RBIF) which, although not explicitly studied for its effect of fatigue strength of Ti-6Al-4V, is classified under surface defects in general, several which have been widely studied.

- **Porosity/Voids Internal Defects inclusive of Lack of Fusion, Balling and Keyholing:**
Porosity defects found in L-PBF parts consists of slit-shaped lack of fusion and near-spherical keyhole pores. The lack of fusion pores is generally more detrimental to fatigue strength due to their shape and orientation [34]. The following guidelines can minimize the effect and occurrence of porosity defects: laser density optimization [35, 36], build orientation optimization [37], generous radii provisions [38], and planning for effect tool paths [39]. Effects of LoF porosity in Ti-6Al-4V are well characterized [106-108, 128, 129].

- **Anisotropic microstructures:** [109, 110] The microstructural variations are caused by a disparity in cooling/solidification rate and remelting/reheating cycles within the part [40]. Most materials show coarse grains in regions near the bottom and fine grains within the topmost regions, concerning the build direction, because of prolonged and repeated heating of the material closer to the baseplate. These variations are known to induce some anisotropy in material behavior
- **Residual Stress:** Layer-by-layer fabrication methodology of L-PBF induces a shrinkage tendency in the sintered layer and a complex stress state through the build. Stresses within each layer are known to show a dependence on the thermal gradients of the underlying geometry; low thermal gradients result in lower residual stress and stress-induced deformations [30, 31]. Possible deformation and stress mitigation solutions include post-fabrication heat treatments and geometry compensation techniques that allow for stress-induced deformation achieving better tolerances on as-built parts [32, 33]. The effects of residual stress in L-PBF have been well modeled [111, 112] and characterized in Ti-6Al-4V [6]. The results of the studies by Wycisk et al. [6] will be useful in the knock down factor comparisons for residual stress in Ti-6Al-4V L-PBF that will be presented in this study.
- **Surface Defects:** Surface finish characteristics have also been well documented to have a significant effect on fatigue life [1]. Morgan and Wells [41] showed that surface finish effects were more substantial than build orientation in a study of Inconel 718 and influenced the fatigue test results (especially HCF) significantly when comparing as-built specimens to improved surface finish treatments. The surface roughness of L-PBF parts

predominantly depends on the orientation of the considered surface. The balling phenomenon, caused by scattering of the melt-pool, affects the top and side surface roughness, while downward-facing surfaces show a high quantity of partially melted powder particles and low surface quality because of the drooping phenomenon [29]. Several studies have established the critical effects of building orientation on both low cycle fatigue (LCF) and high cycle fatigue (HCF) behavior. Yadollahi and Shamasei [34] demonstrated that vertically orientated samples were more detrimental than those horizontally built as they provided more stress concentration under loading, leading to lower fatigue strength. Therefore, it is crucial to characterize the influence of geometric sensitivities to establish design-related standards and certification requirements.

- **Recoater Blade Interference Flaws (RBIF):** While characterization of the surface roughness and finish effects on fatigue strength of AM Ti-6Al-4V L-PBF, has been significantly addressed [110, 113, 126, 127], there has been no significant study of the surface defects associated with recoater blade interference, resulting in the so-called *recoater blade interference flaws* (RBIF). This is especially troubling as multiple AM builds exhibit this flaw as illustrated in a part build failure as shown in Figure 9 [138]. While Netfabb[®] Simulation software and ANSYS[®] Additive can now simulate and predict part build failure due to distortions. These tools are mainly predictive, warning of potential recoater impact locations, does not proceed go beyond that to determine what type of impact and the effect of the impact and resulting depth of the flaw etc. Another key factor that causes distortions is the lack of sufficient supports. This results in sub-optimal heat dissipation for the build and leads to this type of failure.

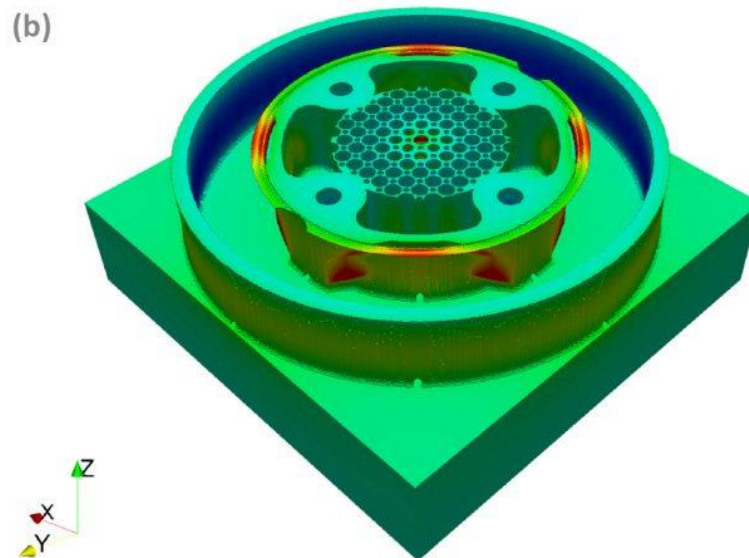
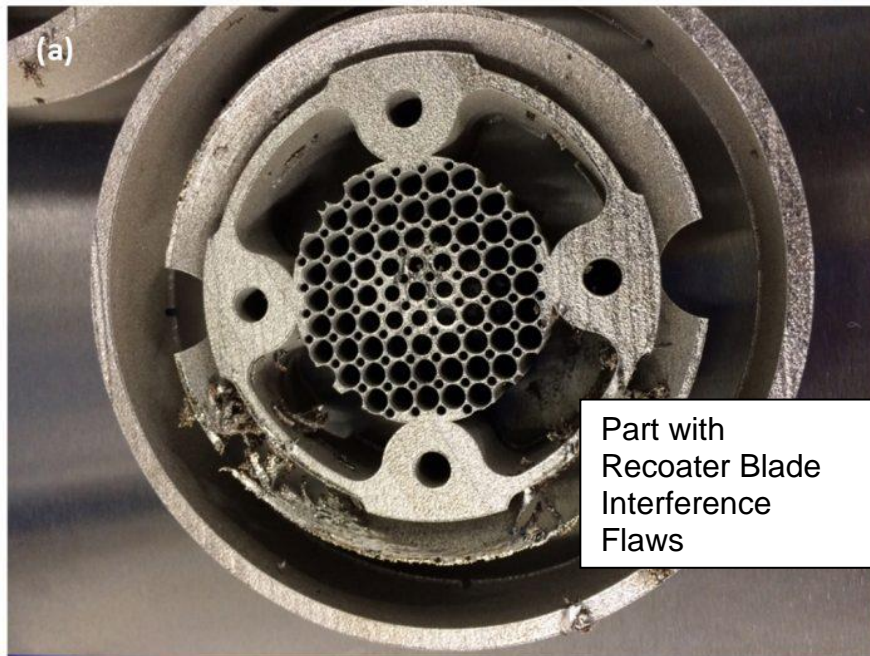


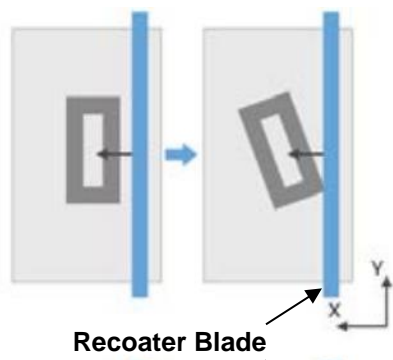
Figure 9. Illustration of Recoater Blade Interference in a Part (a) and Simulation of Distortion using Netfabb® Simulation [138]

Materialise, the maker of *Magics*® software used to pre-process CAD models for AM build, has also noted several other reasons for recoater blade interference. In a recent whitepaper [123], they presented key factors to avoid RBIF as:

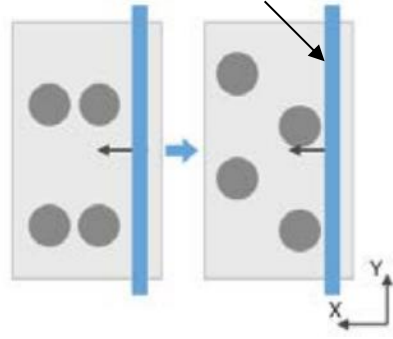
1. **Type of Recoater Blade:** For most L-PBF operations, there are two types of recoater blades used – soft recoater blades and hard recoater blades. A hard recoater has blades made of HS steel or ceramic and exerts pressure on the powder. This type of recoater, in comparison with soft recoaters, does not allow much part deformation. This means that less parts with deformities are produced, but on the other hand, the consequences of a collision with the parts and the recoater would be worse for the build. Either the build stops because the recoater cannot go over the part, or the part is damaged and debris (or the part itself in case of a bad connection to the build platform) is dragged into the powder bed. Another consequence could be that the part is deformed or shifted by the recoater from its original position, leaving a gap between the already printed area of the part and the area of the part that still needs to be printed. These types of recoaters can be useful when identical parts are printed on the same build platform. If one part deforms or is not built successfully, there is a high chance that all the other parts on the build plate will behave the same way, so then it may be preferable to stop the build in case of collision. Another reason to use a hard recoating system is that the manufacturing tolerances can be set slightly lower compared to soft recoaters, because if a part is successfully built with a hard recoater, its maximum potential for deformation is lower than a part built with a soft recoater. The last aspect concerning hard recoaters is their impact on sensitive features such as thin walls or lightweight structures for example. Every time a recoater deposits a new layer of powder, pressure is applied to the powder bed and transmitted to the part depending on the recoating parameters. For big or solid areas of a part, there is no consequent effect, but for geometries that present a high height to width ratio, this pressure can make the structure

vibrate. The vibration will deteriorate the powder bed around the concerned area and can lead to a small part deformation which looks “wavy”, known as a buckling effect [123].

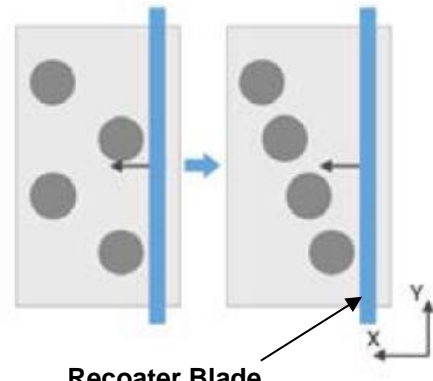
- 2. Position of parts on the build platform.** Empirical data has shown that optimal positioning of the parts on the build plate relative to the path of the recoater blade helps to significantly reduce or eliminate recoater blade interference [123]. This works primarily by reducing the surface area initially in contact with the blade, thus minimizing distortion as the blade goes by the part. When the part is positioned parallel to the recoater, it is more difficult for it to go over the part in case of deformation. Thus, rotating the part 5 to 45 degrees around the Z axis helps to prevent the recoater from passing over a long, flat wall as shown in Figure 10. Given the edges, especially the corners of a part always start to deform first, it is always better if the recoater passes over a corner and then the rest of the part instead of facing a long, flat wall with two corners at a time [123]. Additionally, placement of parts in lines right behind each other in a build makes for potential recoater interference. Such positioning results in the same flaw being repeated in similar fashion across all the specimens, as illustrated by the flawed specimens built for this study, see Figure 28. Placement of different size parts in the build is also important in avoiding RBIF. It is recommended to place the highest parts closest to the recoater blade (if the recoating operation is in one direction) as shown in Figure 10. If the recoating operation is in both directions, then ideally the tallest specimens are best placed in the middle of the build.



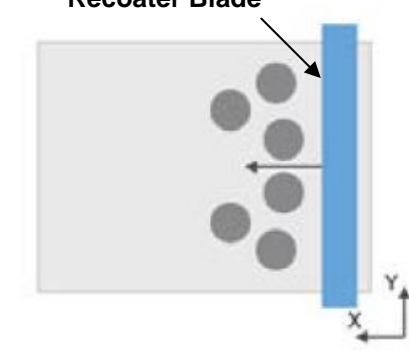
To prevent RBIF, avoid positioning parts parallel to the recoater blade direction



To prevent RBIF, avoid positioning build parts right behind each other



To prevent RBIF, avoid simultaneous contact with the recoater blade



To prevent RBIF, position the highest parts closest to the recoater blade

Figure 10. Positioning Parts on Build Platform to Prevent RBIF [123]

- 3. Support Structures.** Upward distortion during the L-PBF build process plays a significant role in recoater interference, as discussed by several authors [2, 4, 138]. Support structures are the primary means by which the build part is secured to the plate and to minimize distortion during the build as well as to dissipate the heat incurred during the laser melting and subsequent cooling phase of the L-PBF process. Thus, the adequacy of the support structures plays a vital role in minimizing distortions which can lead to RBIF. Various models have been developed to understand the physics of the melt pool and the resulting heat dissipation [128], significant among them are: Netfabb Simulation, and ANSYS Additive [138].
- 4. Aspect Ratio.** The relationship between the height and the base width/diameter of the build part is the aspect ratio. This feature also plays a significant part in how heat is dissipated during the build and thus how much distortion occurs, especially in the Z (build) direction, resulting in recoater blade interference. A part that has a high aspect ratio is more likely to have recoater blade interference than a part with a smaller aspect ratio. The fatigue test specimens built during this study had a high aspect ratio ($h/d = 11.1$) thus resulting in the high likelihood of RBIF.

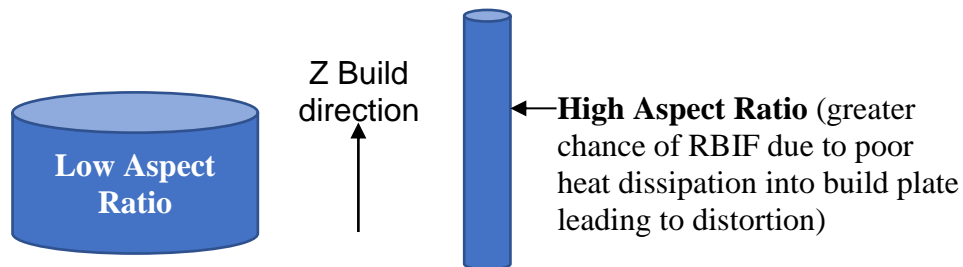


Figure 11. Low Aspect Ratio versus High Aspect Ratio Parts

2.1.2 Electron Beam Powder Bed Fusion (EB-PBF) Process

Another subpart of PBF is the Electron Beam Powder Bed Fusion (EB-PBF), a technology that has improved significantly and according to GE Additive [5], offers the design freedom, excellent material properties and stacking capability. This is an AM technology was developed at Chalmers University of Technology in Sweden and was commercialized by Arcam AB, Sweden, in 2001 [2]. It is based on the melting of metal powder by exposing it to a beam of electrons. The process starts with the spreading of a thin layer of metal powder on a build plate. The powder is pre-heated by exposing the entire layer to a stream of electrons. This broad exposure of electrons heats the powder to an appropriately high temperature based on the material being used (Fig. 2). In the case of titanium alloys, such as Ti-6Al-4V, the powder is heated to about 800°C. Other materials require even higher temperatures.

An electron beam is deflected by an electromagnetic field which transfers energy and selectively fuses parts of the layer by raising the temperature of the pre-heated powder to above the melting point of the material being processed. After melting of the selectively fused parts of the layer is completed, the build platform is lowered and a layer of fresh powder is spread across the build area. Heating and selective fusing of each successive layer builds up the object into the desired shape of the 3D model being produced [5].

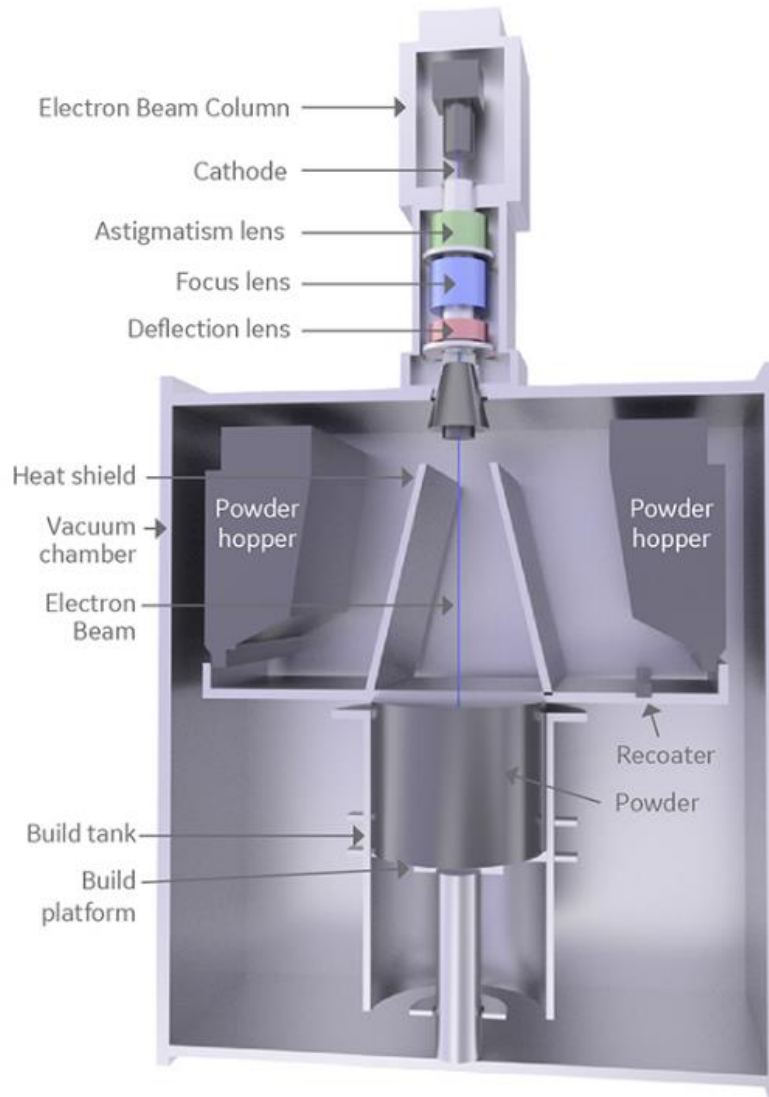


Figure 12. EB-PBF schematic (courtesy GE Additive [5])

The build process concludes once all layers of the build corresponding to the geometry of the part or parts have been heated and selectively fused. Heated but unfused powder forms a ‘cake’ around the fully fused part and needs to be removed and recycled in a post-processing step. This is done by mechanically blasting the surrounding cake and removing excess material from internal channels inside the part as necessary.

The basic architecture of an EB-PBF machine includes an electron beam source, electromagnetic coils to guide the beam to produce the desired shape and a build chamber with a moveable build plate and powder spreading apparatus. Typically, the maximum power output of the electron beam is between 3–6 kW. Electrons are emitted from a heated filament or crystal and accelerated by a high voltage. The electromagnetic coils shape and position the electron beam similarly to how light is focused and positioned by optical lenses and mirrors. The build chamber and the EB source remain under vacuum for the duration of the build process. It takes up to about an hour to create the required vacuum. At the end of the build, the chamber is filled with inert helium gas to speed up the cooling process. After a few hours of cooling in helium, the chamber can be safely opened and exposed to air without risk of powder oxidation [5].

Comparison of the fatigue strength of parts built by EB-PBF vs L-PBF shows that the EB-PBF parts have better fatigue strength properties due to the reduced residual stresses resulting from better control of the temperature gradients between the build and cooling process for each layer [124].

2.1.3 Directed Energy Deposition (DED) Process

The Directed Energy Deposition (DED) process differs significantly from the PBF process because while the latter uses an energy source to melt powder material which is *already* pre-laid on a build plate, the former (DED) uses direct energy (either laser or electron beam – see Figure 6 [131]) focused on a region to heat a substrate metal which is melted *simultaneously as it is deposited* [2]. The first DED process known as Laser Engineered Net Shaping (LENS) was developed by Sandia

National Laboratories, USA and commercialized by Optomec, USA with the “LENS 750” machine launched in 1997. Several other organizations have developed DED machines that use lasers and powder feeders such as Directed Light Fabrication (DLF), Direct Metal Deposition (DMD), 3D Laser Cladding, Laser Generation, Laser-Based Metal Deposition (LBMD), Laser Freeform Fabrication (LFF), and Laser Direct Casting (LDC) among others.

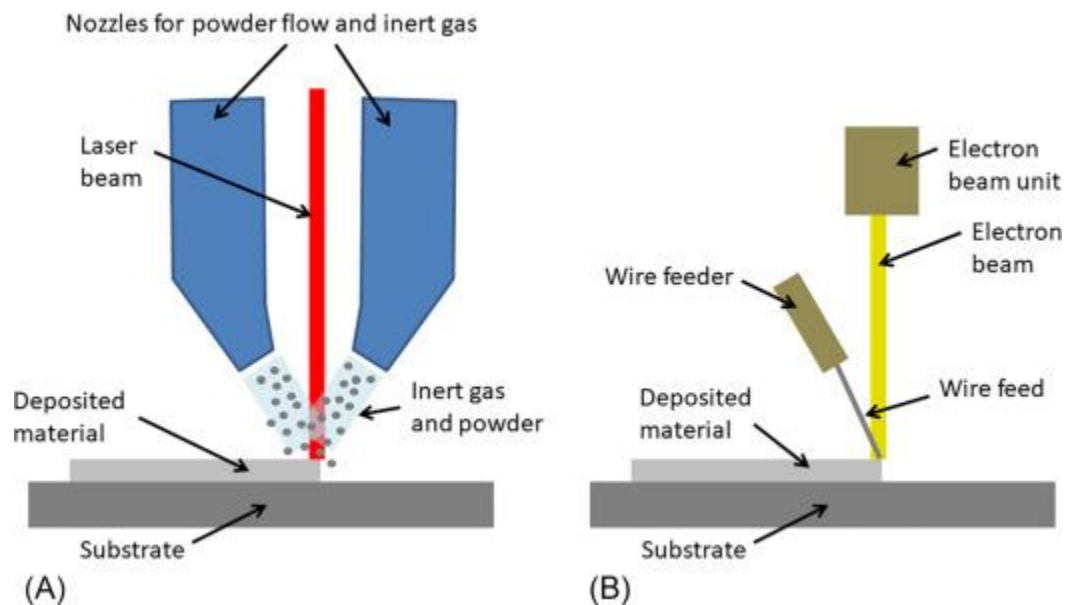


Figure 13. Schematics of two DED systems (A) uses laser together with powder feedstock and (B) uses electron beam and wire feedstock [131]

A key advantage of the DED process is that it allows for variation of parameters in ways that control the microstructure features while providing design freedom. This process is therefore best for repairing and refurbishing damaged and defective components such as turbine blades.

2.1.4 Ultrasonic Additive Manufacturing (UAM) Process

While most metal AM systems use a point-wise method often using metal powder as input, Ultrasonic Additive Manufacturing (UAM) – also known as Ultrasonic Consolidation (UC) - uses

a sheet lamination processes and ultrasonically welds them together using a rotating sonotrode which travels the length of a thin metal foil $\sim 100\text{-}150\ \mu\text{m}$ thick (see Figure 14) [133]. This process is repeated layer by layer, with four layers typically termed as one level. After each level, a CNC milling head shapes the deposited foils/layers to their slice contour. Thus this is an additive-subtractive process with continues until the final geometry is achieved. *Solidica USA* was the first company to commercialize this process in 2000 [1].

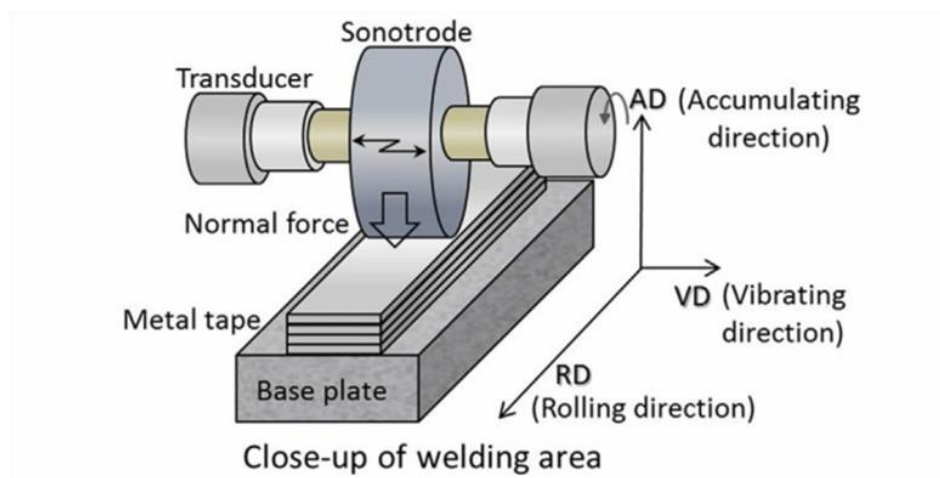


Figure 14. Ultrasonic Additive Manufacturing Process [133]

Since the surface of the UAM-manufactured parts is milled, this approach has the advantage of avoiding surface flaws resulting from the stair-stepping (or RBIF), however, void defects in-between the bonded sheets are common. Due to the low-temperature ultrasonic bonding process, thermal residual stresses are highly reduced in the UAM process, and this allows for embedding sensors during the manufacturing process which can allow for structural health monitoring.

2.2 Fatigue and Damage Tolerance Substantiation of Aerospace Structures

Most major Aerospace OEMs (Boeing, Airbus, General Electric, Lockheed Martin, Textron Aviation, Bell Flight, Northrup Grumman, SpaceX, etc.), Governmental and Regulatory Agencies

(US Army, US Navy, US Airforce, FAA, EASA, NASA) and Standardization Organizations SDOs (SAE-AM, NIST, ASTM-F42, ANSI-AMSC, AWS, ISO etc.), are currently, in one way or other, involved in development of methods to meet F&DT requirements for structural AM parts.

The viability of metal AM products in Aerospace applications was clearly and successfully demonstrated with the production of GE Aviation's LEAP™ engine nozzle which as of October 2018, GE had over 30,000 of these nozzles produced at its Auburn, Alabama advanced manufacturing facility utilizing the metal PBF process [5]. The fuel nozzle is a complex part. It must withstand thermal cycles ranging in thousands of degrees. Thanks to the geometric freedom of AM, it was possible to consolidate this 18-part design into one intricate part with multiple interior channels - Figure 6. Not only did the new nozzle turn out to be 25 percent lighter and five times more durable than previous generations of nozzles, but when all 19 of these nozzles were installed on a GE LEAP™ jet engine, the fuel nozzle design helped to reduce fuel consumption and CO² emissions by 15 percent [5]. This is a clear illustration of the enormous advantages that the metal AM process of making aerospace parts has over the traditional cutting, forming or casting in several key aerospace applications.



Figure 15. GE LEAP™ Engine Nozzle made by Metal L-PBF Process [5]

While the GE fuel nozzle is indeed a great example of a huge aerospace metal AM success story, it represents only a small fraction of what is already possible from a design-build solution perspective. So why has this still not taken off with more high-value structural aerospace components? Several gaps are presented by America Makes and ANSI-AMSC [7] but the largest of these, as highlighted by Ristori et. al. [8] and Seifi et. al. [9], is the F&DT Q&C challenge. Indeed, as the FAA's Dr. Gorelik [10] noted just a few years back, while envisioning that aerospace components in the 'minor' and 'major' flight safety effect category (e.g. the GE fuel nozzle) could, within a foreseeable timeframe, meet FAA Q&C requirements, with critical parts he remains less optimistic - note the question-mark on Figure 1 of the timeline to achieving Q&C for additively manufactured 'critical' parts, which provided the motivation for this study.

2.2.1 Classification of Aerospace Critical Structural Parts

What *are* Aerospace “critical” parts? Civilian airworthiness authorities such as the Federal Aviation Administration (FAA), European Aviation Safety Agency (EASA) and Transport Canada Civil Aviation (TCCA) identify Principal Structural Elements (PSE) to be the most critical parts from an airworthiness certification perspective. According to 14 CFR 29.571 b(2)6 [11] a PSE is defined as a “*structural element that contributes significantly to the carriage of flight or ground loads, and the fatigue failure of that structural element could result in catastrophic failure of the aircraft.*” AC25.571-1D [15] further defines a Principal Structural Element (PSE) as:

“An element that contributes significantly to the carrying of flight, ground, or pressurization loads, and whose integrity is essential in maintaining the overall structural integrity of the airplane. Principal structural elements include all structure susceptible to fatigue cracking, which could contribute to a catastrophic failure.”

The equivalent spacecraft terminology for a PSE is Class A1/A2 parts per the guidelines in NASA’s standard MSFC-STD-3716 [16]. Class A1 is the most stringent and would be composed of AM parts that have a high consequence of failure and a high structural demand. NASA defines a part as having a high structural demand if it does not satisfy the criteria for classification as having a low structural demand per the assessment criteria presented in Table 2 [17].

Equivalent to PSE parts for the US Air Force and Navy are those classified by the criteria in the Joint Services Specification Guide (JSSG-2006) [17] as highly critical, single load path safety of flight parts - Fracture Critical I or II (FC-I/FC-II). Further, Air Force requirements for the Aircraft Structural Integrity Program (ASIP) are defined in Mil-STD-1530C [18] as Durability Critical (DC) or Maintenance Critical (MC) - structural parts affecting the economic life of the

aircraft. For purposes of this review paper, wherever the term PSE is used, it shall be understood to include the equivalents of Class A1/A2, FC-I/FC-II and DC/MC parts.

Table 2. Assessment Criteria to Determine Structural Demand [17]

Material Property	Criteria for Low Structural Demand
Loads Environment	Well defined or bounded loads environment
Environmental Degradation	Only due to temperature
Ultimate Strength	Minimum margin ≥ 0.3
Yield Strength	Minimum margin ≥ 0.2
Point Strain	Local plastic strain < 0.005
High Cycle Fatigue, Improved Surfaces	Cyclic stress range (including any required factors) $\leq 80\%$ of applicable fatigue limit
High Cycle Fatigue, As-built surfaces	Cyclic stress range (including any required factors) $\leq 60\%$ of applicable fatigue limit
Low Cycle Fatigue	No predicted cyclic plastic strain
Fatigue Mechanics Life	20x Life factor
Creep Strain	No predicted creep strain

2.2.2 Fatigue and Damage Tolerance Substantiation Requirements for PSEs

One of the most thoroughly authored criteria for Q&C of PSEs for F&DT evaluation of “conventional” metallic PSEs is that from the FAA. It is also one where a significant set of guidance material has been provided for methods of compliance. The FAA regulations for F&DT substantiation of PSEs are enshrined in 14§CFR 25.571 [11] for transport category aircraft and in 14§CFR 29.571 [12] for transport category helicopters. The corresponding guidance provided by the FAA on the acceptable means of compliance to the regulations, are provided in AC 25.571-1D [16] and in AC29-2C [20], respectively. The goals in both 25.571 and 29.571 are to ensure that the substantiation of the PSE results in retirement times and inspection intervals that ensure that the probability of failure (PoF) of the PSE before detection and removal from service is extremely remote. Following the latest updates to the AC29-2C [20] per amendment 29-55 of the 29.571B

rule, more requirements were recently added to the F&DT Q&C process for rotorcraft PSEs. These additional requirements provide significantly more insight into methods of compliance for F&DT analytical substantiation that cover *effects of defects*, especially intrinsic and discrete flaws, as those expected in the AM processes for metallic PSEs.

2.2.2.1 The Rule

Parts of the rule per 14 CFR§25.571 and 14 CFR§29.571 is recited here for reference:

14 CFR§25.571: “(a) An evaluation of the strength, detail design, and fabrication must show that catastrophic failure due to fatigue, corrosion, manufacturing defects, or accidental damage, will be avoided throughout the operational life of the airplane...”

14 CFR§29.571: “(a) A fatigue tolerance evaluation of each principal structural element (PSE) must be performed, and appropriate inspections and retirement time or approved equivalent means must be established to avoid catastrophic failure during the operational life of the rotorcraft. The fatigue tolerance evaluation must consider the effects of both fatigue and the damage determined under paragraph (e)(4) of this section.”

Paragraph e(4): “For each PSE., a threat assessment which includes a determination of the probable locations, types, and sizes of damage, taking into account fatigue, environmental effects, intrinsic and discrete flaws, or accidental damage that may occur during manufacture or operation.”

2.2.2.2 Methods of Compliance for Metallic Structure F&DT Substantiation

While the overarching goal for F&DT substantiation of a metallic structure is captured in the foregoing rules, a typical analysis involves additional ingredients that are also governed by specific FAA rules/certification requirements. Many OEMs employ different methodologies however, they generally need to address similar key areas of basic metal F&DT analysis as defined by Stephens, Fatemi and Fuchs [99]. A concise practical guide for F&DT evaluation for aircraft is also presented by Duprat [21]. It begins by reviewing the basics of what fatigue is for aircrafts and the history of *safe-life analysis* methodologies and their shortcomings. While fatigue was typically addressed from the 1950's by means of safe-life methodology which provided an adequate level of reliability, it was however identified in the 1980's that higher levels of reliability was necessary to account for fatigue-strength-reducing effects of damage that had been shown by experience to occur during manufacturing or operational service per AC 27-1B MG11 [22].

Lessons learnt from introduction of composites led both manufacturers and regulatory authorities to develop more rigorous safe-life methodologies that accounted for specific static and fatigue-strength-reducing effects of aging, moisture absorption, temperature, voids, and impact damage. This drove increased requirements for fatigue substantiations to capture the *effects of defects* arising from both intrinsic flaws (inherent to the design and manufacture of the part e.g. inclusions, cracks, porosity) and discrete flaws (caused by external action such as corrosion, scratches, wear, impact and cracks initiated by fatigue). These additional analysis of effects of defects certainly seems to cover many of the issues that metal AM parts face and is worth digging further into. However, it is important to note how the fatigue initiation analysis differs from damage tolerance analysis and how AM metallic parts could be assessed in the context of these two types of analysis. AC 27-1B MG11[22] explicitly defines fatigue as the degradation process

of a structure subjected to repeated loads that may involve four phases. The boundaries of these phases are not in practice easily defined but Table 3 summarizes the phases and the analysis types that are employed in each phase.

Table 3. Crack Phases and F&DT Analysis Type

Crack Phase	F&DT Analysis Type
1) Nucleation of many micro-cracks	Crack Initiation (Safe Life)
2) Coalescing of some micro-cracks to one major macro-crack	
3) Stable crack growth	Crack Growth Analysis
4) Unstable crack growth and immediate failure.	

Crack initiation analysis (safe-life) methods are used to predict the ‘safe period’ for which the PSE part can operated at the assumed usage spectrum without a fatigue crack initiating to reach a macro-crack per Table 3 phase 1 and 2. Crack growth analysis methods determine the growth rate from phase 3 to the unstable and immediate fracture phase 4 [22, 99].

The FAA has provided guidance [20] in the form of methods of compliance that meet the requirements of the F&DT rules for analysis of metallic structures, inclusive of the effects of defects for PSEs. These methods of compliance are summarized in Table 4.

Table 4. F&DT Methods of Compliance discussed in AC29-2C [19]

Analysis Approaches	Method No.	Threat Assessment	Method of Compliance	Strategy
Crack Initiation Approaches	1	Not Included	Safe-Life Retirement	Retirement
	2	Not including cracks	Safe-Life Retirement with BDF(s)	Retirement
	3	Not including cracks	Safe-Life Retirement with CDF(s)	Retirement
	4	Included	Safe-Life Inspection for CDF(s)	Inspection
	5	Included if considered for all elements	Safe-Life Inspection for Failed Element	Inspection
Crack Growth Approaches	6	Included if Crack Bounds Damage	Crack Growth Retirement	Retirement
	7	Included	Crack Growth Inspection	Inspection
Other Approaches	8	Included	Supplemental Procedures	Inspection
	9	Included	Approved Equivalent Means	Inspection

BDF – Barely Detectable Flaws.

CDF – Clearly Detectable Flaws

2.2.2.2.1 Crack Initiation Methods (Safe Life) Analysis of AM Metallic Parts

Civil certification requirements for transport rotorcraft require crack initiation (safe life) analysis of the metallic PSEs to cover BDFs for retirement time and CDFs for inspection interval (except for Method 1 in Table 4 which must be combined with an inspection method accounting for CDF flaws). Since any AM metallic part, by nature of the manufacturing process, has BDF and CDF intrinsic flaws, Method 1 is automatically ruled out and cannot be considered for AM metallic parts from the onset. Methods 2 and 3 include BDF and CDF flaw sizes to determine a retirement strategy for the part. Method 4 includes threats which are allowed to initiate to detectable crack sizes. Method 5 considers the effect of a failed element of the PSE analyzed and assumes the analysis will substantiate an interval long enough for the inspections to detect the failed element. Thus, the challenge for the AM metallic part crack initiation (safe life) analysis is how to obtain

and properly apply the empirical and analytical input data required in Table 4 to obtain results with adequate structural reliability. This is what the enhanced fatigue substantiation methodology in this study will attempt to show in Section 3.2, in furtherance of Table 4 Method 3 for metallic AM PSEs – towards an enhanced Safe life with CDF approach. Summary of F&DT substantiation approaches from literature reviewed indicates several potential approaches that address crack initiation (safe life) analysis in AM metallic structural parts.

2.2.2.2.1.1 Knock-Down-Factors (KDF) based approaches

Crack initiation (safe life) analysis can be based on full-scale fatigue tests or analysis that is supported by element or coupon test data [21, 99]. Knock down factors (KDFs) are typically applied in these cases to account for material scatter (with and without flaws), load variability (pilot maneuver variability), design/construction (leading to fit/form variability), and usage (mission) variability. The most challenging factors to determine for AM metallic materials are the material scatter and design/construction related factors [15]. Approaches listed below attempt to address this gap.

2.2.2.2.1.1.1 NASA MSFC System-Safety Approach to Determine KDFs

A method to determine the appropriate KDFs for metal AM parts based on a system safety and part-criticality-based analytical approach was presented by NASA MSFC [17]. The analysis begins by determining the “consequence of failure” and the “structural demand” of the AM parts to identify and apply the necessary analytical method with the reliability and safety factors determined through this system safety approach. The lowest criticality is Class B4 and highest is

Class A1. Different analytical factors of safety are applied based on this system safety classification.

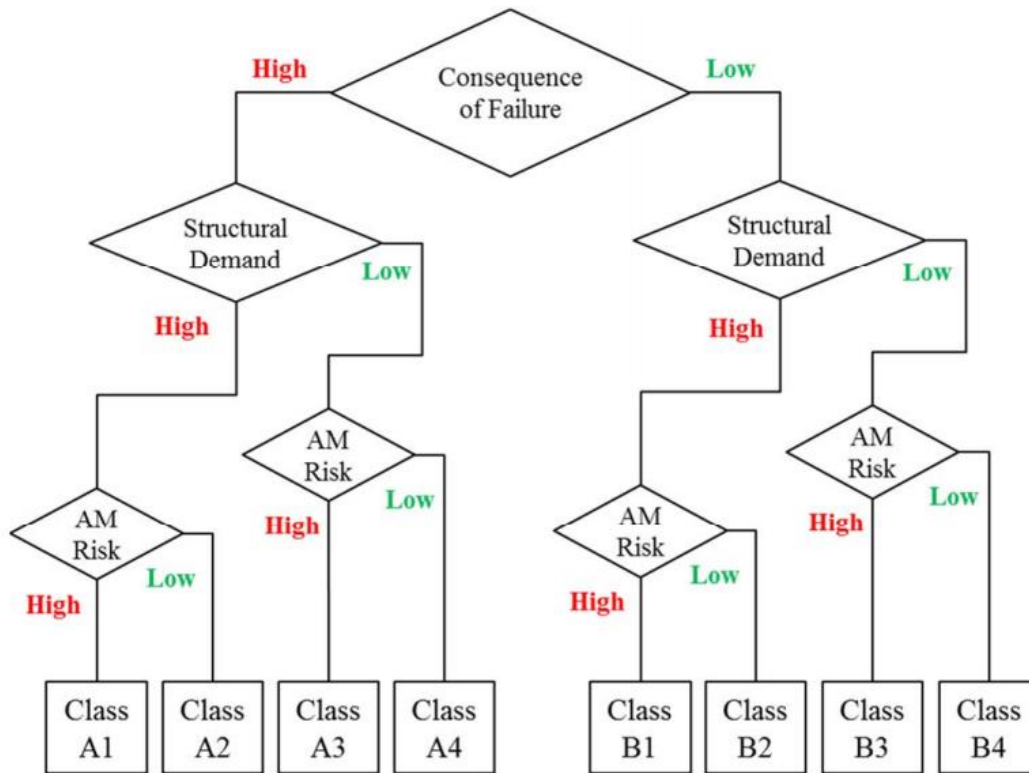


Figure 16. Part Classification (courtesy NASA MSFC [17])

Indeed, this approach does not leave out the most critical Class A1 (PSE's). By assigning KDFs *as high as 10* in certain applications, NASA-MSFC [17, 43] and NASA-STD-5019A [46] provides pathways for Q&C of all structural applications of metal AM parts inclusive of the most critical Class As. The challenge with this approach for civil certification is the importance of performing detailed failure modes and assessments analysis (FMEA) and a criticality ranking (FMECA) for every AM PSE part analyzed. This may further include performing a Functional Hazard Assessment (FHA) for each system that is impacted by the failure of the additively manufactured component. The FHA is performed first as an Aircraft Functional Hazard Analysis (AFHA) and

then as a System Functional Hazard Analysis (SFHA). Using qualitative assessment, aircraft functions and subsequently aircraft system functions will need to be systematically analyzed for failure conditions. Each failure condition will be assigned a hazard classification. Hazard classifications are further aligned by Development Assurance Levels (DALs) as shown in Table 5 per the guidance in ARP4761 [47] and related aviation safety documents such as ARP4754A [48], 14 CFR 25.1309 [11], and Radio Technical Commission for Aeronautics (RTCA) standards DO-254 [49] and DO-178C [50] covering various aircraft equipment, systems and installations.

Table 5. Hazard Classification and Design Assurance Level, PoF per Flight Hour [47]

Hazard Classification	Development Assurance Level	Maximum Probability per Flight Hour
Catastrophic	A	10^{-9}
Hazardous	B	10^{-7}
Major	C	10^{-5}
Minor	D	--
No Effect	E	--

As can be seen, the classification process may become more complicated than the F&DT analysis itself but is necessary to identify the analytical factors to be applied. In any case, a first conservative approach is to assume the ‘catastrophic’ hazard classification and hence apply the most stringent factors in the analysis.

While the NASA approach allows for F&DT analysis of AM metallic parts subject to application of appropriate factors by the aforementioned classifications, there are additional ranking requirements in NASA-MSFC [16, 42] to appropriately implement this approach: (1) all volumes and surfaces must be reliably inspected or proof tested, (2) the as-built surface must be

fully removed for all fatigue-critical surfaces, (3) surfaces interfacing with sacrificial supports must be fully accessible or can be fully improved, (4) structural walls or protrusions must be ≥ 1 mm in cross-section, and (5) critical regions of the part require sacrificial supports. Expanded methodologies are required to cover scenarios where one or more of these requirements cannot be met.

2.2.2.2.1.1.2 Industry approach with KDF-based Material and Process Factors

Airbus' Mardaras [15] determined that the current certification standards in EASA regulations [52], which mimic FAA regulations, are fully applicable for AM parts. Airbus further states that the processes for F&DT including material qualification, design value definition and stress analysis approach (per CFR §29.571, 29.603, 29.605, 29.613) for AM have been agreed with EASA, thus claiming success in that regard. Airbus' approach for crack initiation (safe life fatigue) analysis follows the traditional safe-life methods [21, 99] but with the additional development of KDFs based primarily on the material and process variability resulting from internal and external defects [15, 25]. Airbus proposed development of data banks of fatigue KDFs that can be drawn upon to analyze specific variables affecting fatigue primarily to address surface condition issues which are discriminated by surface roughness (Ra) value. A similar KDF approach is applicable to crack growth. Additionally, KDFs can be applied based on various zones but with the application of different KDFs by them to different zones of a part referenced by Gorelick [10] and Taylor et. al. [26]. Additionally, they compared the established risk mitigation frameworks for material systems such as the use of casting factors for cast aircraft components, analogous to conventional casting factors approach. Encompassed within this approach are the methods of compliance listed in Table 4 as Methods 2, 3 and 4. Depending on the size of flaw used for the KDF - BDF for retirement, CDF for retirement and CDF for inspection

respectively. A perspective by FAA Chief Metallurgist Khaled [45], opines on AM metallic parts that while Q&C of transport category aircraft per 14 CFR 25 [11] is subject to factors of safety per CFR 25.303, and statistical design values per CFR 25.613 and possibly special factors per CFR 25.619, for aircraft engines 14 CFR 33 [12] is applicable without subjection to similar factors of safety or requirements. In Khaled's view, regardless of whether a design is a "component", an "engine" or an "aircraft", materials and processes approvals applied to the build are implied when the design is certificated. Hence, he queried the need for the FAA to regulate materials and processes for AM as separate entities. Indeed, per FAA Advisory Circular AC20-107B [44], section 6a(7), the FAA does not generally certify materials and processes – the materials and processes are accepted as part of a particular aircraft product overall Q&C.

Differences in the application of structural Q&C per CFR Part 25 for aircraft and Part 33 for engines has Khaled [45] also opining that the FAA should perhaps consider waiving certain Part 25 requirements in favor of 'meaningful qualification and lot acceptance testing.' This calls for the FAA, to work directly or through Designated Engineering Representatives (DERs) and Designated Manufacturing Representatives (DARs), to be intimately involved with qualification testing of first articles (control parts). This will indeed help to verify the adequacy of the manufacturer's material and process selections and further, lot acceptance testing and verification with witness specimens can be conducted with FAA or company designated representatives verifying and validating the results against the control parts from the first article test. This requires significant allocation of resources to develop the necessary test data e.g. [99, 100]. This takes a significant commitment from the primary stakeholders – industry and certification authorities but will ensure that conforming parts are manufactured consistently.

2.2.2.2.1.2 Building Block Approach for AM

This approach borrows from a good example of the description for Q&C of composites. FAA advisory circular AC20-107B [44] establishes that “the strength of a composite structure should be reliably established, incrementally, through a program of analysis and a series of tests conducted using specimens of varying levels of complexity.” This is often referred to as the “building block” approach. These tests and analyses at the coupon, element, details, and subcomponent levels can be used to address the issues of variability, environment, structural discontinuity (e.g., joints, cut-outs or other stress risers), damage, manufacturing defects, and design or process-specific details. Typically, testing progresses from simple specimens to more complex elements and details over time. This approach allows the data collected for sufficient analysis correlation and the necessary replicates to quantify variations occurring at the larger structural scales to be economically obtained. The lessons learned from initial tests also help avoid early failures in more complex full-scale tests, which are more costly to conduct and often occur later in a certification program schedule.

A conceptual schematic of tests typically included in the building block approach for a fixed wing is provided in Figure 6. The large quantity of tests needed to provide a statistical basis comes from the lowest levels (coupons and elements) and the performance of structural details are validated in a lesser number of subcomponent and component tests. Detail and subcomponent tests may be used to validate the ability of analysis methods to predict local strains and failure modes. Additional statistical considerations (e.g., repetitive point design testing and/or component overload factors to cover material and process variability) will be needed when analysis validation is not achieved. The static strength substantiation program should also consider all critical loading

conditions for all critical structure. This includes an assessment of residual strength and stiffness requirements.

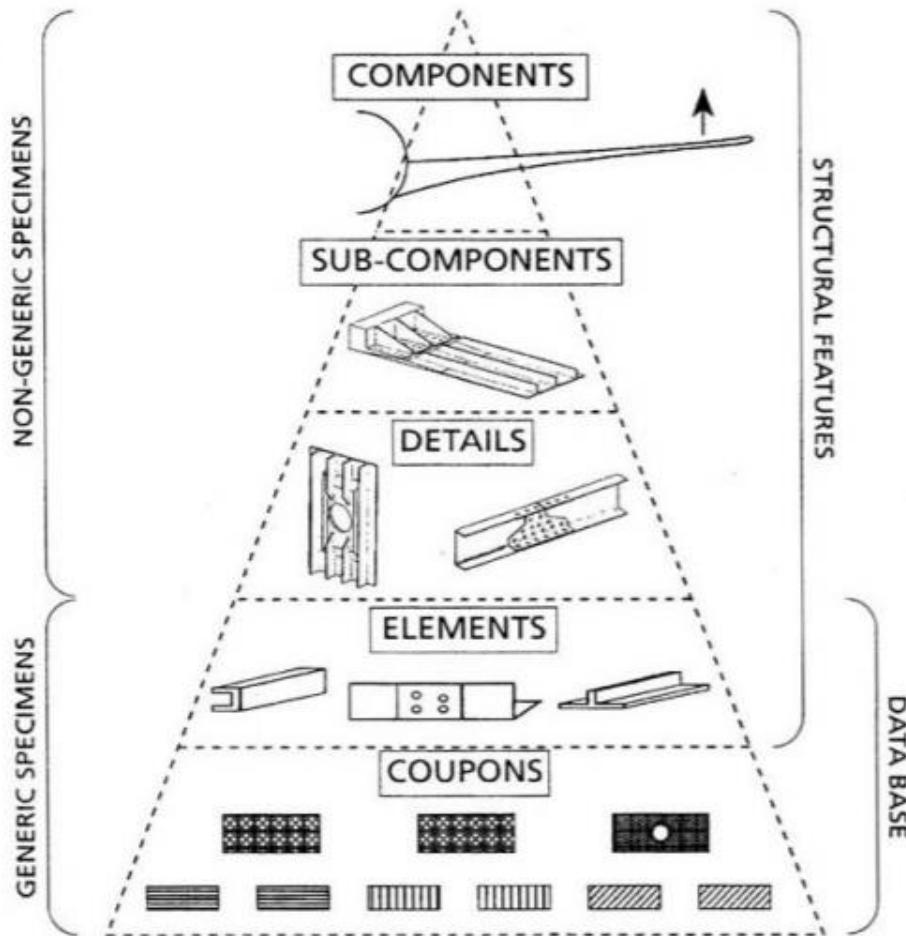


Figure 17. Schematic Diagram of Building Block Tests for a Fixed Wing [44]

FAA AC20-107B [44] sets forth an acceptable means for compliance with provisions of Title 14 of CFR parts 23, 25, 27 and 29 regarding airworthiness type certification requirements for composite aircraft structures involving fiber reinforced materials e.g., carbon and glass fiber reinforced plastics. AM metallic parts do not fall under this category currently covered by AC20-107B [44] but, as Taylor et. al. [26] opined, they exhibit similar properties including the same high variation on a micro scale, in-homogeneity at the meso scale and interactions among constituent

metals that are difficult to predict at these scales. As such, their properties are developed and applied at the macro scale to embed interactions and manufacturing effects at a scale where they can be effectively characterized.

The most significant challenge to the building block approach are the large economies of scale needed [7] for the coupon test programs to develop all the statistically based allowables required to the extent of inclusion in well-established references like MMPDS or CMH-17 [99, 100]. Indeed, the key advantage to AM is the low volume production hence this goes against the large economies of scale (subtractive processes). One possible approach is to develop full scale parts e.g. with the advent of Big Area Additive Manufacturing (BAAM), a full-scale wing can be produced using AM and several elements and coupons extracted at key features or details to determine notch sensitivity, differences in properties at different sections of the build etc. Lockheed Martin, Oak Ridge National Laboratories and Cincinnati Incorporated are primarily involved with the development of BAAM [51].

2.2.2.2.1.3 Safe Life Inspection for Failed Element

Another F&DT method of compliance applicable to inspections of metallic parts is the inspection for failed elements, Method 5 in Table 4 [20]. This approach may be especially appealing to metal AM parts that provides for additional freedom of design to incorporate multiple complex redundant load paths especially with the design of lattice structures. Metal AM lattice structures also incorporate the support structures necessary to prevent distortion during the build [78] which additionally provides the load paths that could be used to monitor the progress of fatigue failure. Fatigue safe life analysis performed using stresses calculated with the assumption that some of the structural load paths (inspectable) are considered to have no load-carrying capability, allows for

determination of a fatigue life that substantiates an inspection interval for the failed element. KDFs like those proposed by Mardaras et. al. [15] and NASA-MSFC [17] are still necessary and applicable to this method to account for uncertainty in material and process parameters, load variability, usage variability and part criticality when providing the recommended inspection interval for the failed element.

The safe-life analysis focused on inspection for failed element requires an understanding of the effect of the failed element. This requires a study of multiple analysis modeling scenarios to understand the failure effects. It requires further FMEAs and FHAs as discussed in 1(a) to determine the effect of the failed element to the function of the PSE and the effect downstream. Often, this requires determining which among the possible load path failures most critical (primary) and the secondary paths and analyzing all. Gaps remain in showing applicability of this approach to F&DT of structural PSEs and their resulting effects.

2.2.2.2.2 Crack Growth Methods for Analysis of Metallic Structures

Certification requirements for transport rotorcraft, per the latest amendment of CFR 29.571 (amdmt 29-55) [12, 20] require crack growth analysis of all metallic PSEs to account for effects of defects. The substantiation must cover BDFs for determination of retirement times per method 6 of Table 3 and CDFs for determination of inspection intervals per method 7 of Table 3 for inspections. Method 6 of Table 3 could cover both retirement and inspection if the Bounding Equivalent Crack (BEC) covers the CDF size. A factor is typically applied to cover for material scatter. If using fatigue crack growth rate data for conventional metallic materials and processes (machined plate, forging, castings etc.) $N = 2$ is assumed for bottom of scatter regression fits (Walker, NASGRO, Forman etc.), and $N = 4$ for mean fits [12, 20].

Airbus claims to have proposed to EASA and found acceptance of the applicability of the current 29.571 regulations extended to AM metallic structure [15], but while proceeding with some of the approaches listed in this section for the F&DT analysis of PSEs, it is not yet clear if the FAA will allow application of the associated advisory circular guidance [20] to perform crack growth analysis of AM metallic PSE structure. For example, it is not clear if the same material scatter factors applied to fatigue crack growth rate (FCGR) data as $N=2$ for top of scatter and $N=4$ for mean, remain applicable or if these need to be increased for analysis of AM metallic parts. NASA-MSFC [17] provides factors of up to 10 for spacecraft critical hardware of Class A1 (PSEs) based on the system-safety approach. More studies, such as this one, are necessary to elucidate on a clear path that provides a practical substantiation approach while ensuring the appropriate level of structural reliability is maintained. Full-scale FCGR testing to validate the crack growth analysis methods for AM metallic structures will help close these Q&C gaps. Further, the implementation of metal AM PSEs in some well-monitored applications using lead-the-fleet aircraft will provide valuable in-service experience that can help inform decision-making.

2.2.2.2.2.1 Crack Growth Analysis using Defect modeling

A method to model the influence of void features, such as size, shape, and distribution, on the fatigue and fracture behavior of AM materials was discussed by Yadollahi, Mahtabi et al. [53]. Additionally [54, 55] developed applications for introducing effects of defects to model crack growth especially in L-PBF products. Typically, the methodology applied per AC29-2C [20] is to determine a BEC for the initial crack size that the aerospace industry assumes as an initial crack equal to the depth of the worst flaw considered in the threat assessment [22]. Further refined approaches to determine the Equivalent Initial Flaw Size (EIFS) are discussed by Fawaz [97]

showing the results of testing and analysis. The benefit of new approaches such as that based on Kitagawa–Takahashi diagrams [55] is also compared over the back-extrapolation method that requires significantly more testing which slows down its appeal [56].

An effective method for analysis of AM metallic defects was presented by Carrion, Shamsaei, et al. [57] using a defect-sensitive crack growth analysis model applying linear fracture mechanics concepts to predict the fatigue life of 17-4PH stainless steel fabricated using L-PBF process. The defect was introduced into the model using Murakami’s approach with the area method [58, 59]. By this approach, the value of the square-root of the defect area is used as the initial crack length in the crack growth calculations that were accomplished using NASGRO software. The approach was validated by comparing the fatigue life results predicted using NASGRO software combined with the Murakami approach, to the results obtained experimentally. Results correlated well, and it was shown that this approach can meet acceptable reliability requirements. It is therefore proposed for analysis of AM metallic structure by this approach, that the initial defect size based on an intrinsic flaw e.g. lack of fusion (LoF) or porosity, be modeled as an initial crack whose length (a) is equal to the square root of the defect area projected in the direction of the applied loading. It has been further proposed [56] that based on Murakami’s initial crack size, for *as-built specimens* having multiple micro-notches on the surface, it would make it difficult to measure defect size accurately. Hence the AM parts should consider the post-contour process. Using a scanning strategy after melting the powder at the edge of the surface for better surface finish could result in a conservative approach to determine the crack size of as-built parts [59].

$$\sqrt{area_{as-built}} \cong d\sqrt{10} \quad (\text{Equation 2})$$

Where: d = width of the area covering the post-contour process on the circular fracture surface of the specimen

Muhammad, Carrion and Shamsaei [57] claim that typical values resulting from Equation 2, for the L-PBF process employing EOS machines, typically range from 60 μm to 80 μm . An upper bound for the EOS machines may be determined assuming $80\mu\text{m} \times \sqrt{10} = 253\mu\text{m}$. In English units, this results in an approximately 0.01-inch initial crack size. It is worth noting that this is about double the initial crack size recommended by Airbus [15]. This study plans to build and fatigue test specimens with multiple flaws up to 0.02-inch depth.

Determination of the right EIFS, the applicable defect size in a crack growth analysis, is critical to ensuring the structural reliability of the resulting crack growth life prediction. Using the typical approach assuming the depth of the worst size flaw is equal to the initial crack size is considered conservative [21]. Romano, Bruckner-Foit et al. [61] showed that a combination of defect-tolerant design with well-established and newly proposed fracture mechanics methods is key to expressing the relationship between the fatigue strength and material quality. Using fatigue crack growth simulation models based on the maximum defect size for estimating both the life and scatter of the data in the region of elastic material response. While this approach may conservatively cover the AM metallic crack growth analysis, it however results in the challenge to find more accurate ways to represent the defect-size in the model more accurately to maximize fatigue life. Additionally, the issue of multi-site damage (MSD) applicable to the AM metallic as-built parts needs to be addressed as single defects do not capture the effect of MSD. To add to the complexity, the difficulty of randomly distributed defects highlights the added need for non-deterministic analytical approaches.

2.2.2.2.2 Probabilistic Fracture Mechanics Approach

Deterministic approaches discussed in the prior sections, while providing less computational difficulty, often result in overly conservative results. This has been cited by Meneghin [62] as one of the challenges for adopting AM parts in the aerospace industry which results in overweight designs. Deterministic solutions do offer a quicker path towards Q&C of PSEs, however, in order to take full advantage of the weight-savings that could result from design optimizations capable through AM, probabilistic damage tolerance methods are necessary. This analytical method helps to cope with the combined variabilities of the fatigue evaluation inputs illustrated in Figure 3, namely: flight loads, design/geometry, materials and process, and usage spectrum variability. Probabilistic methods can be considered, however, without achieving the proper scale of computations necessary, these seldom obtain efficient and reliable results. The complexities included in computations of fatigue and fracture mechanics and probabilistic approaches can be overcome in the life-cycle reliability analysis of MSD using the Gaussian process (GP) response surface model. It was demonstrated with one of the recent multiple crack analysis tools, XFEM, in a study by Kim, Chau-Dinh et al. [63]. The assembled GP-XFEM method represented an efficient way to model the surface and sensitivity factors of multiple crack propagation in a structure (or a component) under a complex environment with computational efficiency. The accuracy and advantages of the proposed method were verified by a number of experimental results and numerical examples.

The probabilistic fracture mechanics approach to damage tolerance analysis is computationally intensive but in the same token it is uniquely framed to best solve the DT problems of AM parts. It is capable of simultaneously considering the variabilities involved in the analytical inputs, with the goal of converging on a solution that is better refined by the number of iterations run. To run

the billions of DT simulations requires robust and efficient tools. Several OEMs have developed their own tools while others have been developed through collaborations between the government and industry. DARWIN is a computer program designed to integrate FEA, fracture mechanics NDE and probabilistic analysis to analyze rotor failures. DARWIN has been found acceptable by the FAA for use in aircraft gas turbine engine analysis per AC 33.14 [98]. The FAA has also recently sponsored the SMART|DT tool [64] as an ultrafast crack growth probability of fracture (PoF) simulation tool. Figure 18 shows the schematic of the SMART|DT methodology which shows the consideration of geometric variability, usage variability, loading variability, inspection detection variability and most importantly the variability of material data, all of which affect the resultant F&DT life of the AM parts.

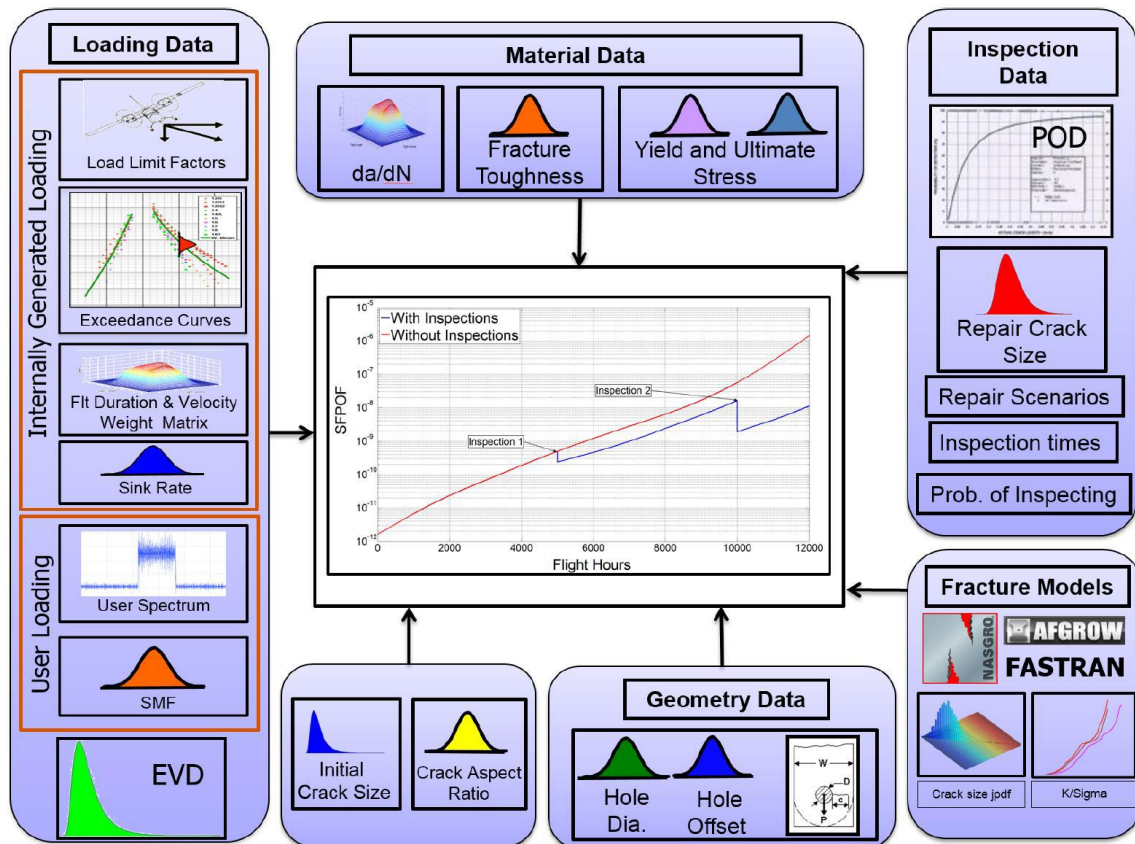


Figure 18. SMART|DT Schematic – (Courtesy – Ocampo et. al) [64]

A significant challenge to the application of this method lies in development of the probability density functions (PDF) for the various inputs to the metal AM F&DT evaluation. The most significant gaps lie in the PDFs addressing variability in AM part quality based on process parameters, material properties and geometric features. Advances in standardization especially of the L-PBF process [43, 65, 67, 68] have helped to reduce the variability but for the probabilistic F&DT analysis, a thorough study of each powder alloy and machine combination, characterizing the distributions specific to the process parameters variables, for specific geometries, is necessary. The analysis proceeds once the PDFs are input into the probabilistic DT calculator together with other well understood PDF distributions such as usage (missions) variability, flight loads variability (studied using different pilots and aircraft flying the similar maneuver) and Probability of Detection (PoD) distribution studies. Additional studies on a round-robin problem [91-94] shows the potential to arrive at divergent solutions from the same dataset depending on the probabilistic solution path taken and number of iterations run. Hence the need to apply unified, peer-reviewed and industry accepted probabilistic methods and analytical approaches [94-96].

2.2.2.2.2.3 NDE, Structural Health Monitoring and In-Situ Monitoring Approaches

The use of NDE to reliably monitor a structure for F&DT failure before it reaches critical size is key to meeting the goals of CFR 25/29.571 [11,12]. FAA's AC29-2C [20] recommends for PSEs that the NDE method applied meets the 90% PoD at 95% confidence interval – the so-called 90/95 requirement. Detection of cracks in metallic structure is highly dependent on their geometric location, the lighting, surface condition and other factors. Due to its ability to manufacture parts with internal cavities, undercuts and other complex geometric shapes, AM makes several

conventional NDE methods inadequate to meet the inspection requirements at 90/95. Several studies of PoD on conventionally manufactured metallic structures are reported in [74, 75, 76, 77], but there is a lack of sufficient PoD studies of AM metallic structures, especially as-built. It has been shown that the surface smoothness has a great effect on the detection of cracks, and the less smooth the surface, the more difficult it is to detect cracks [74, 75, 77]. NASA has performed some limited NDE studies on parts made by AM and has outlined some approaches taken to apply NDE these parts [89]. They could be compared to as-cast surfaces in conventionally manufactured parts.

The use of structural health monitoring (SHM) for management of fatigue critical components (in situ), has been shown to be valuable and practical in many applications. FAA Advisory Circular AC29-2C [20] discusses use of SHM, in-situ monitors using embedded sensors such as the Fiber-Bragg Grating (FBG) sensor or chip-detectors that sample oil in a gearbox to detect spalling or gear wear, as a *method of compliance* under the Approved Equivalent Means (AEM) used for F&DT certification of PSEs (see method 9 from Table 4). The US Army, a leader in Condition-Based Maintenance (CBM), collaborated with Bell Flight's Tucker, Mochache et. al [24] to present a fatigue life management approach for dynamic components for the US Army's OH-58D Kiowa Warrior fleet. It used data from embedded sensors integrated to a Honeywell Zing[®] data collector that was downloaded to the Honeywell PC-GBS system on the ground. Bell developed Regime Recognition Algorithms (RRA) that interpreted the collected flight data and as well-developed Fatigue Damage Calculator (FDC) that determined the expended fatigue lives relative to the baseline fatigue lives for the components. Huston [69] indicated that the use of these sensor-based technologies will continue to rise and especially so for valuable areas where

the parts to be studied require active monitoring such as is the case for metal AM PSEs where this is needed to provide additional structural reliability.

Due to the high thermal stresses encountered during the build, the L-PBF metal AM processes do not lend well to embedded sensors, however, recent studies by MacPherson, Hand, et al. [70] have shown some success. A metal AM process that is better suited for embedding sensors is the Ultrasonic-based Additive Manufacturing (UAM) approach. UAM combines ultrasonic metal seam welding of thin – typically 100-150mm thick metal foils - and CNC milling. A rotating sonotrode travels along the length of a thin metal foils to bond them. The foil is held closely in contact with the base plate or previous layer by applying a normal force via the rotating sonotrode. This additive-subtractive process continues until the final geometry of the part is achieved [2]. Thus, UAM process happens without large thermal gradients allowing for embedding of sensors such as the FBG sensor for flaw monitoring and detection. Example applications are given in References [71, 72, 73]. PoD studies are needed to determine the effectivity of detecting cracks using various inspection methods on metallic AM parts of varying surface quality. This PoD studies will provide the necessary confidence in the NDE methods applied to detection of cracks in metal AM PSEs, hence enhancing the structural reliability of the retirement and inspection intervals. Further work is also needed to develop embedded sensors that can withstand the thermal stresses of the L-PBF process.

3 Methodology Enhancement

While all the F&DT methodologies for substantiation of metallic structures reviewed in Section 2.2.2.2 have potential for applicability to AM metallic structures, the challenges and hurdles listed for each of them to overcome necessitate a need to select a most efficient approach to getting there quickest and reliably. This study chose to focus on the crack initiation method (safe life retirement) which begins with nominal fatigue strength data reduced with a CDF flaw reduction factor (method 3 of Table 4) – i.e. KDF from a CDF such as the RBIF. While this approach has not yet been explicitly used in civil certification of metallic AM PSEs, it has been presented for spacecraft hardware qualification by NASA [17] and has indicated initial acceptance of similar approach [15] with EASA. While indeed the threat assessment used to set the CDF size such may capture the worst-size physical flaw (such as RBIF = 0.020-inch depth for the specimens investigated), an enhancement to this methodology for added reliability is to combine the KDF from this CDF with a KDF resulting from a potential lack of adequate stress relief heat treatment. This study will show that a combination of KDFs as this provides additional reliability necessary to perform the fatigue substantiation of AM PSEs.

To provide additional clarity on this approach, we begin by reviewing the basic analytical theories supporting safe life fatigue analysis and the proposed enhancements to the use of KDFs specific to metallic AM PSE applications. The aim of the enhanced approach is to provide additional confidence in implementing these combined KDFs to support F&DT Q&C of PSEs. F&DT is a specialized discipline within structures analysis which involves the assessment of the structural integrity of part subjected to the application of repeated or fluctuating stresses, strains and stress

intensities. This discipline is focused on improving design, manufacturing, certification and continued operational safety by applying the principles of material science, fatigue and fracture mechanics to develop effective material characterization methods, design criteria and life cycle management plans for critical components [132]. F&DT substantiation analysis has evolved from so-called infinite-life analysis approaches to safe-life and finally fail-safe or damage tolerance approaches [100]. Within these approaches, depending on the computational power and inputs available, either deterministic models, where outputs are fully determined by the input parameter values and the initial values, or probabilistic (or stochastic) models which incorporate random variable selection with monte-carlo-type iterative simulations, can be used. For this study, the deterministic approaches were employed for the evaluations within the two broad F&DT substantiation approaches recommended below [20]:

- i. **Crack initiation analysis** which seeks to identify a safe-life period within which significant cracks are not expected to have initiated from pristine parts (assuming no-flaws) or from as-manufactured parts with flaws. This determines the appropriate interval for safe *retirement time* of the part.
- ii. **Crack growth analysis** which assumes cracks have initiated from flaws with initial crack sizes assumed to be as large as the flaw size or as determined using EIFS and proceeding to determines their crack growth rate(s) to determine the time to detectable crack size and to critical crack size. The crack growth analysis provides the *inspects intervals* and/or *retirement times*.

From the F&DT substantiation standpoint in the Aerospace industry, the problem of what analysis method to employ to substantiate a metallic component, is best posed in terms of which most

efficiently satisfies the Q&C requirements while satisfying reliability requirements especially for PSEs/LLPs/FCs described in 2.2.1 (henceforth simply referred to as PSEs). The discussion in Section 2.2.2.2 presents all the various requirements put out by various certification entities (FAA, NASA, JSC etc.) for structural substantiation. While it is understood that, with the exception of the recent NASA-MSFC guidelines [17, 43], most of the other requirements for F&DT substantiation were not designed specifically with metallic AM substantiation in mind.

3.1 Baseline Deterministic Crack Initiation Analysis

This study expounded on current baseline methodologies detailed for Metallic structures F&DT analysis of PSEs by FAA in AC29-2C [20], as well as proposed approaches by NASA for Metallic AM L-PBF substantiation of Spacecraft hardware [17], and industry approaches such as the KDF approach by Airbus [15]. While seeking to find applicability and enhancements of the requirements of the latest amendment to CFR§29.571 (amendment 29.55) [12], there still has been no explicit guidance indicating what the FAA will accept in terms of an F&DT substantiation of AM metallic PSE, however, based on this general guidance for F&DT substantiation of metallic PSEs to the latest amendment of the rule, it remains for additional studies, such as this, to identify gaps and provide enhanced approaches to address them.

According to the definition in ASTM E206 [114], fatigue is progressive localized permanent structural change occurring in a material subjected to conditions which produce fluctuating stresses and strains at some point (or points) and which may *culminate in cracks* or complete fracture after a sufficient number of fluctuations.

Various theories have been postulated for the calculation of cumulative fatigue damage [116] arising from the initiation of micro-cracks and the coalescing of them based on the fluctuating

stresses and strains to result in fracture. The predominant and most practical theory postulated is that by A. Miner in 1945 known as “Miner’s rule” [117]. It includes earlier work by Palmgren who initially proposed a theory to account for fatigue in bearings [122], thus the combination of the two results in the *Palmgren-Miner theory* of fatigue damage [117, 118]. It is a linear rule that states that the sum of the ratio of alternating stress cycles to the number of cycles applied (n_i) to the number of cycles to failure (N_i) sums to unity (1) at the time of fatigue failure. This can be expressed mathematically as shown in Equation 3 below and applied to the overall safe-life fatigue substantiation analysis as shown in Figure 19:

$$\sum_{i=1}^{Fracture} \frac{n_i}{N_i} = 1 \quad \text{Miner's rule [116, 117, 118]} \quad (\text{Equation 3})$$

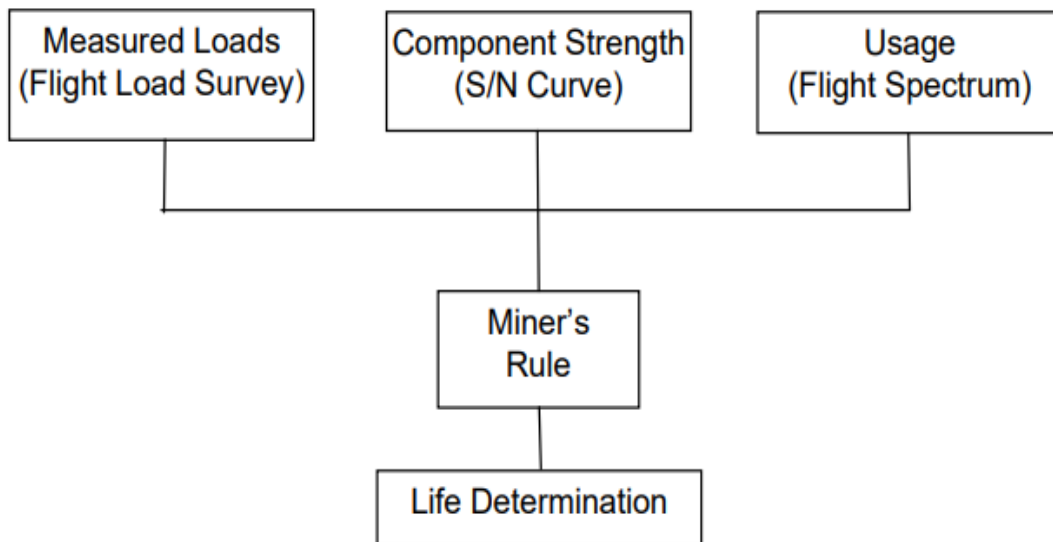


Figure 19. Elements of a Safe-Life (Crack Initiation) Analysis [22]

Therefore, it is necessary that for crack initiation fatigue life substantiation using Miner’s rule to obtain the three key inputs necessary in the Miner’s rule calculation as shown in Figure 19:

- *Component strength (material data)*: obtained empirically and typically presented in the form of an S-N curve that shows the alternating load/stress/strain in the ordinate and the total number of cycles to failure (N_i) along the abscissa. The alternating stress level below which no significant fatigue damage is expected to occur is known as the endurance limit (S_E). For non-ferrous materials (such as Ti-6Al-4V), the S_E value is typically at 10^8 cycles [99]. Additional reliability in the fatigue life prediction is placed in the material scatter allowed. The greater the number of test specimens, the more reliable the mean strength prediction. Typically, for the aerospace industry, fatigue strength reliability for most homogenous materials can be shown adequately using at least six fatigue coupons with a 3-sigma reduction for scatter ($\mu - 3\sigma$) [120] as it follows a normal distribution. The S-N curve fitting shape is another pertinent ingredient to the fatigue prediction characteristic and is often informed by the pattern of fatigue stress versus cycles-to-failure from the test data. Most in the aerospace industry use the Weibull equation to formulate the S-N curve shapes which define the constants k , m and E_∞/E , for the Weibull equation 4 below:

$$N = k \left(\frac{S}{E} - \frac{E_\infty}{E} \right)^{-m} \quad (\text{Equation 4})$$

Where:

N	Number of cycles to failure
S	Alternating/Oscillatory stress
$k, m, E_\infty/E$	Material curve shape parameters
E_∞/E	Ratio of fatigue strength at infinity to fatigue strength at a specified number of fatigue test cycles
E	Fatigue strength at a specified number of cycles: (Typically 10^8 for non-ferrous metals)

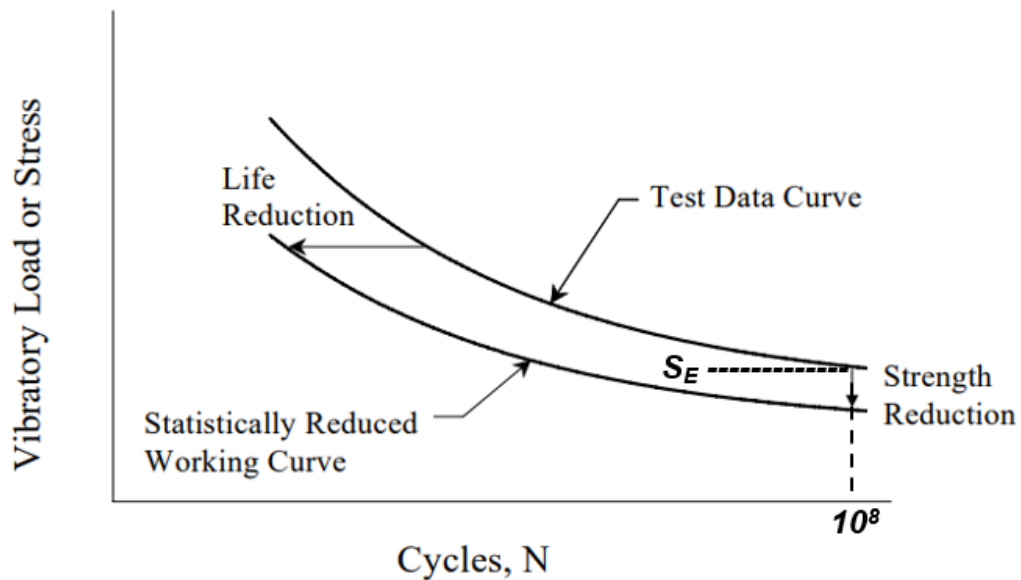


Figure 20. Typical S-N curve for Safe Life (Crack Initiation) Evaluation [22]

- *Usage (Flight Spectrum)*: This provides the number of cycles applied (n_i) to the structure to analyze during at each operating condition (based on the defined flight vehicle spectrum). Again, for reliability in critical substantiation application in aerospace, typically a 90th percentile usage spectrum is assumed for added confidence in the fatigue life predictions for critical structure [120]. A proposed enhancement for increased reliability of AM structural analysis is to increase this to mean plus 3 sigma for increased reliability for the AM structural part substantiations.
- *Mean and Oscillatory stresses or strains (S)*: The stress state at the fatigue failure location must be determined through a good understanding of the elasticity mechanics of the structure and loading combined with the geometric stress concentration factors, K_T . This is where the design and construction of the AM parts that gives rise to the effects of various flaws, such as the RBIF affect the number of cycles to failure [99]. Hence, for the simple axially loaded

fatigue specimens, assuming a load P is applied across the nominal test section area A , the stress at the test section is given by the equation 5 below with a correction for induced moment (M) if the specimen is not properly axially aligned as were the specimens with RBIF:

$$\sigma = \left(\frac{P}{A} + \frac{MC}{I} \right) * K_T \quad (\text{Equation 5})$$

Where: P = Axially applied load, A = cross section area, M = Bending moment across the section, C = distance from neutral axis to stress recovery point edge (for circular cross sections it is the radius), I - moment of inertia of the cross section and K_T = stress concentration factor

Since the S-N curve is typically developed at a single R-ratio (minimum stress divided by maximum stress), often when developing fatigue strength allowables that compare various alternating (oscillatory) stresses on a part at different mean/steady stress level, it is necessary to use either the Soderberg line (Equation 6), Goodman (Equation 7) or the Gerber curve (Equation 8) [99]. These plots provide the endurance limit (S_E) at $R = -1$ (y-intercept) and the x-intercept empirically determined from yield strength (F_{TY}) or Ultimate strength (F_{TU}), depending on which of the plots is selected – the Soderberg uses F_{TY} while Goodman and Gerber use F_{TU} .

$$\text{Soderberg line equation:} \quad \frac{S_{OSC}}{S_E} + \frac{S_{MEAN}}{F_{TY}} = 1 \quad (\text{Equation 6})$$

$$\text{Goodman line equation:} \quad \frac{S_{OSC}}{S_E} + \frac{S_{MEAN}}{F_{TU}} = 1 \quad (\text{Equation 7})$$

$$\text{Gerber curve equation:} \quad \frac{S_{OSC}}{S_E} + \left(\frac{S_{MEAN}}{F_{TU}} \right)^2 = 1 \quad (\text{Equation 8})$$

The Soderberg line equation (Equation 5) is the most conservative of the three listed above and is recommended for fatigue crack initiation analysis for critical applications [22]. The Soderberg line was developed in study using the static and fatigue data generated for the Ti-6Al-

4V specimens tested. The fatigue testing for the baseline specimens was used to establish the mean endurance limit Point A and the flawed specimen endurance limit established as Point B. Additionally, the yield strength F_{TY} was determined from static specimen tests for each configuration and compared to expected values in literature - the lowest static values for similar configurations were selected.

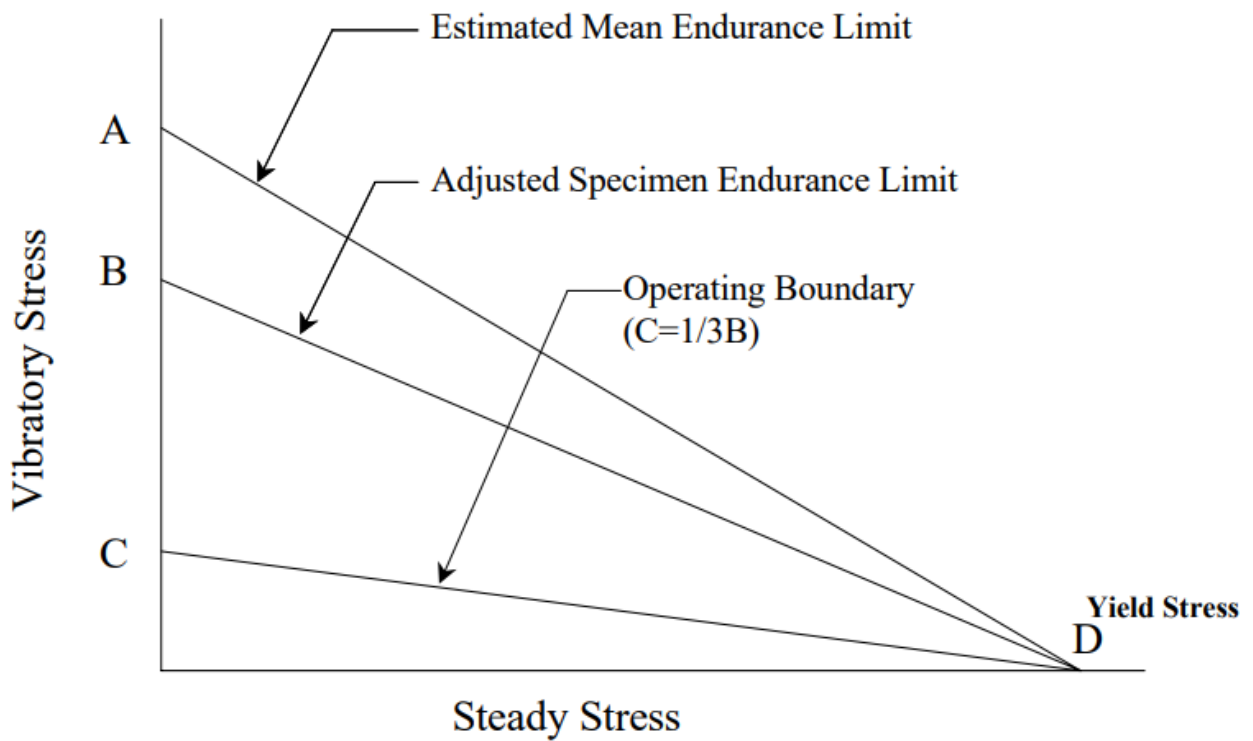


Figure 21. Soderberg Method for Safe-Life (Crack Initiation) Evaluation [22]

3.2 Enhanced Deterministic Crack Initiation Analysis

Many studies have highlighted material fatigue strength characterization as the most important of the of the 3 key inputs to the fatigue analysis illustrated in Figure 23, where an enhancement would have greatest effect in the F&DT process for metallic AM parts [1, 8, 9, 26, 146, 147, 148]. The inputs of usage spectrum and spectrum loads/applicable stresses need refinement to provide a wholistic approach that ensures sufficient fatigue margins exist to meet structural reliability inclusive potential clearly detectable flaws (CDF) or barely detectable flaws (BDF) resulting from the L-PBF processes. Several studies have shown that variabilities in the three primary independent inputs to the F&DT evaluation process, shown in Figure 23, namely: *usage spectrum*, *flight loads* and *material strength* data, all follow normal probability density function (PDF) distributions [23, 24]. The approaches currently used for F&DT substantiation use scatter reduction factors and mean reduction offsets to combine the three inputs statistically to account for usage spectrum and flight loads variability (with 90th percentile spectra being an acceptable reliability norm for PSEs [24, 120]), and $\mu-3\epsilon$ variability applicable to material strength fatigue testing with a minimum of four to six test specimens. This has been shown to serve reliably well for conventional (subtractive) metal applications [139], with the resulting conservative fatigue life retirement predictions meeting the requirements for a Probability of Failure (PoF) that is “very remote”. The term “very remote” in FAA regulation 14 CFR 29.571/25.571 [11, 12] is not explicitly defined statistically, however, for the failure of a PSE which is considered catastrophic, the target design assurance level based on ARP4761 [47] as shown in Table 5, PoF per flight hour $< 10^{-9}$.

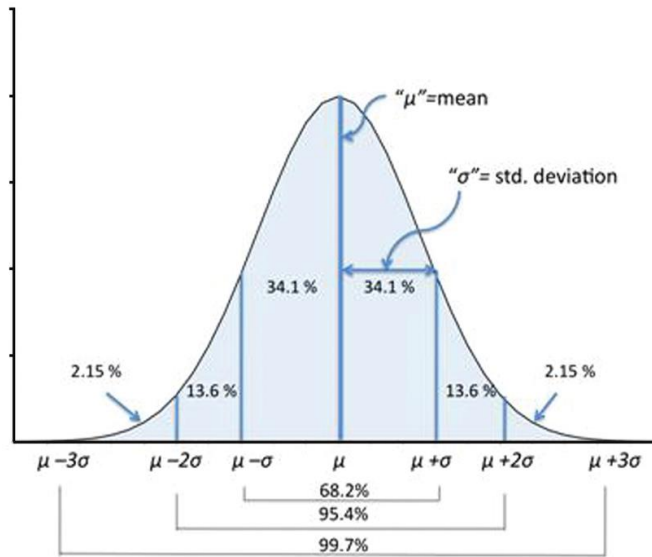


Figure 22. Normal distribution, mean, and standard deviation

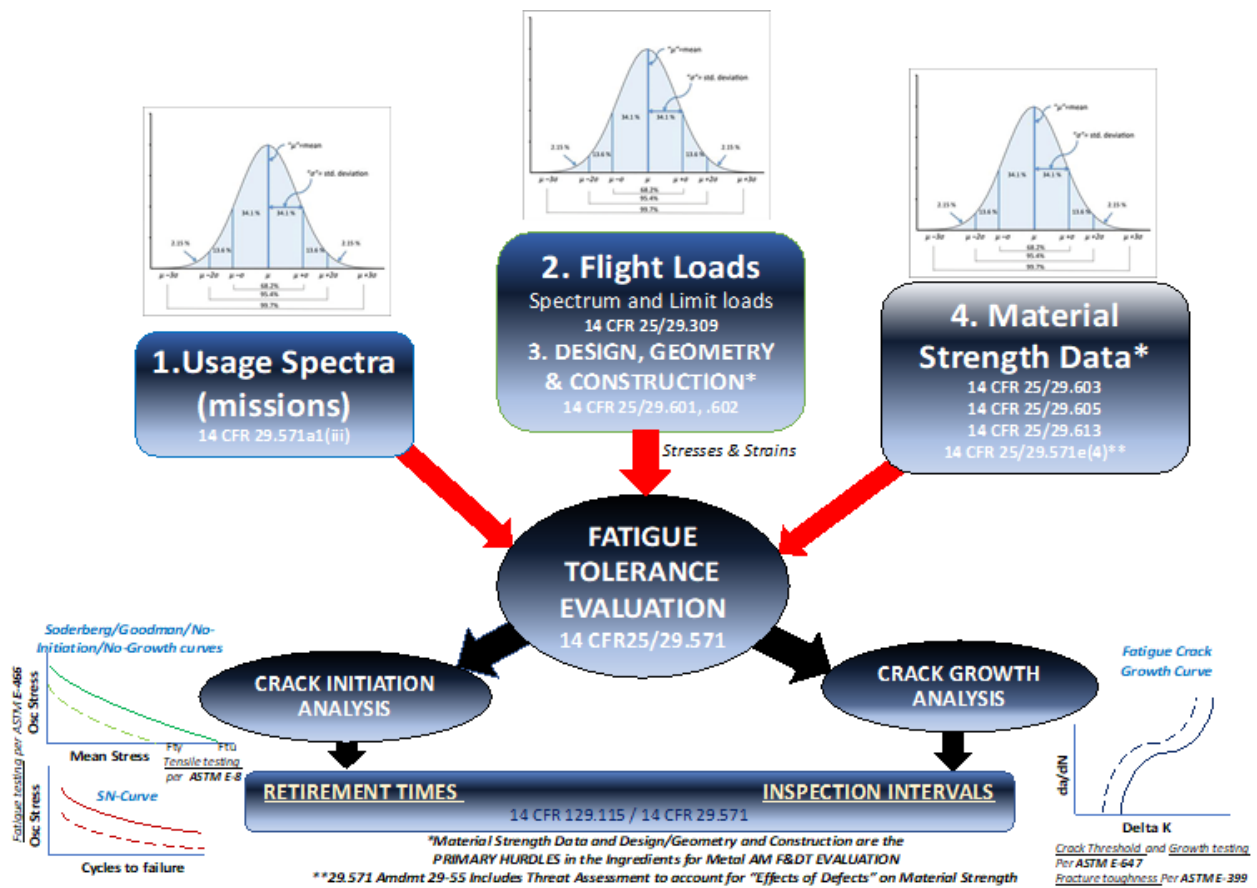


Figure 23. Key inputs to F&DT evaluation and effects of Metal AM

Equation 8 presents the un-modified relationship between allowable vibratory stresses that must be met when comparing strength-to-load ratios that meet requirements for PSEs made using approved manufacturing methods. Casting factors between 1.25-1.5 have been introduced in the past to account for casting variability but process improvements have reduced these [140].

$$\sigma_{allowable\ stress} \leq \frac{\mu_{strength} - 3\sigma_{strength}}{\mu_{load} + \sigma_{load}} \quad (\text{Equation 9})$$

where:

$\mu_{strength}$ = mean fatigue strength for more than 4 fatigue test specimens (no KDF)

$3\sigma_{strength}$ = 3 standard deviation reduction in mean strength (99.7%)

μ_{load} = mean flight spectrum load for given flight condition

σ_{load} = standard deviation of flight load distribution for condition

The reliability of Equation 9 for safe life analysis has been shown to be 0.9985 [23, 139, 143] as determined from the PDF interaction between load and strength shown in Figure 24.

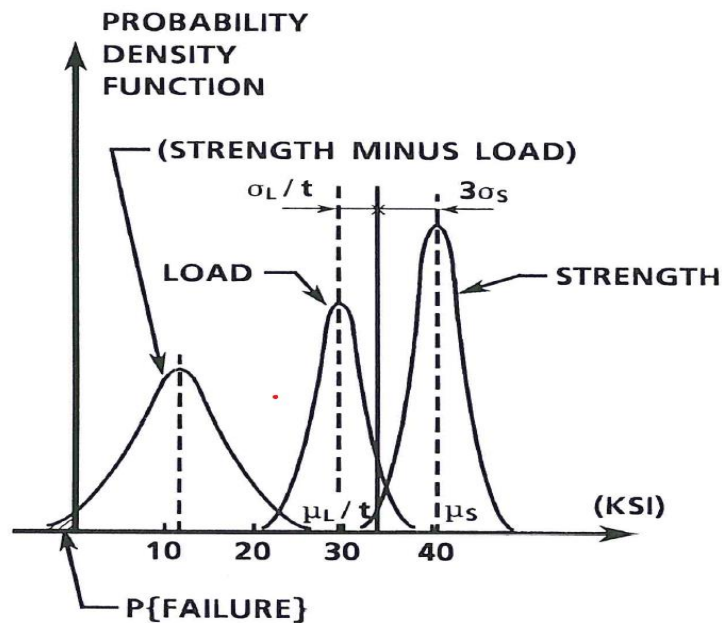


Figure 24. Combining Material Strength and Load PDF distributions [139]

Additional enhancements for increased reliability in application to metal AM using the L-PBF process are proposed in the modification of Equation 9 to Equation 10, which is supported by the data presented in this research. The mean fatigue strength is based on a minimum of 5 fatigue test coupons, both with and without flaws. Reduction in mean fatigue strength was based on the KDF generated for RBIF and residual stress, which is applied based on test results of coupons tested with RBIF and residual stress compared to ones without RBIF or residual stress.

$$\sigma_{allow.to.3million.cycles} = \frac{\mu_{strength}/(KDF_{RBIF+RS}) - 4\sigma_{strength}}{F_{am} * (\mu_{load} + 4\sigma_{load})} \quad (\text{Equation 10})$$

where: $\sigma_{3m_MaxCycles}$ = stress at which max life of 3 million osc cycles (at all oscillatory load levels) can be sustained without significant fatigue damage (Review shows most as-built testing limited to 3million)**

$\mu_{strength}$ = mean fatigue strength for more than 4 fatigue test specimens

$KDF_{RBIF+RS}$ = Knockdown factor for combined RBIF and Residual Stress

$4\sigma_{strength}$ = 4 standard deviation reduction in mean strength (99.99%)

μ_{load} = mean flight spectrum load for given flight condition

σ_{load} = 4 standard deviation of flight load distribution for condition

F_{am} = Additive manufacturing factor similar to casting factor (1.25-1.5) added to load variability. To be adjusted with additional empirical data. The max value applies if the part is principally loaded in the Z build direction (lowest strength), or if any location on part lacks proper inspectability. Lowest factor applicable if, in addition to being principally loaded perpendicular to Z build direction, the part is machined, polished and HIPed.

The probability of a severe surface defect (RBIF), in combination the lack of adequate residual stress relief occurring at the fatigue-critical location of a CIS, can be considered “extremely remote”, per the language in the rule given in Section 2.2.2.1. This enhanced method is based on the safe-life with CDF retirement - method 3 of Table 4 – with additional reliability for fatigue substantiation of metallic AM PSEs assuring sufficient fatigue margin. This methodology enhancement also proposes an additional AM factor (F_{AM}), akin to the casting factors of MMPDS

[100], initially proposed in the similar range of 1.25-1.5, to be further validated with additional full-scale testing. The specimens tested in this study's yield strength reductions range as providing sufficient reliability. Similar to the casting factor review approach [140], the K_F factor is proposed for further additional studies to dial up or down the reliability based on additional full-scale validation tests.

Using the existing requirements for the safe life analysis approach and the additional enhancements proposed here in, studies as this will continue to develop the appropriate KDFs for material strength reduction characterizations for various other materials in the presence of RBIF and stress relief omission in the critical test gage sections, a combination which adequately covers other materials and processes variations shown in Figure 8 [21]. These assumptions must certainly continue to be reviewed by the effects-of-defects characterizations, which with the current state of study for Ti-6Al-4V AM products made by L-PBF, is sufficiently understood to hierarchy significant effects as: 1. Residual Stress, 2. Surface Roughness (RBIF/stair-stepping etc.), 3. Microstructure defects, 4. Internal porosity (lack of fusion, keyholing). [106-112, 126-128, 146-148].

The applicable strength reduction factor (KDF) of each of the potential flaws, based too on the continued understanding of design and construction-related flaws that generate largest K_F , is required for deterministic F&DT analysis that accounts for these potential manufacturing and in-service flaws and their fatigue-life-limiting effects. While it is almost impossible, for each new design and material, to test for every single type of flaw that can potentially occur in parts made from either wrought materials, castings, or AM processes, it is key to continue statistically ranking the worst-case defects and reviewing probabilities of the combinations of these defects occurring

at the fatigue critical locations of the parts and obtain combined KDFs for each studied effect-of-defect characterization. This is indeed the approach considered most relevant and practical for the aerospace industry applications, as put forward as well by aerospace industry giants: NASA [17], Airbus' [15], academia [1, 28], and others to follow.

4 Research Test and Data Collection

Static and fatigue tests were conducted to collect research data to characterize the fatigue strength of Ti-6Al-4V and to test out the null hypothesis (H_0) that there is no significant reduction in fatigue strength in L-PBF built Ti-6Al-4V specimens resulting from RBIF at $\alpha = 0.05$. The static and fatigue tests were conducted at AADFW Inc., a NADCAP[®] accredited material testing facility. All loads, setup, witnessing and test data reviews were supported by the author as well as the AADFW Inc. personnel (primarily technical lead, Jeremy Wilson), with additional guidance from my advisor, Dr. Taylor. The research data obtained from conducting the static and fatigue tests using specimens made using UTA's EOS-M290 machine and the L-PBF process, from Ti-6Al-4V Grade 5 powder, with and without RBIF, was compared to other industry data obtained from published sources with specification detailed.

4.1 Project Outline and Execution

The project outline and set of accompanying tasks listed in Table 6 were undertaken to accomplish the objectives of this research. A total of 12 specimens were built all in the Z orientation (Z-direction is established as more critical for fatigue properties [147]), in two separate batches; one batch was built with RBIF and one without. The specimen overall dimensions were as shown in Figure 25. All specimens were built at the University of Texas Arlington's (UTA) Additive Manufacturing lab using an EOS M290 machine, acquired by the University in 2019 and calibrated and maintained to EOS' guidelines and specifications. The static tests were conducted per ASTM E8 and fatigue tests were per ASTM E466. Fatigue tests were run at 30 Hz at ambient room temperature. The test machine used for both the static and fatigue tests was a hydraulically

powered SATEC 120, TC-25, serial number 106. Mechanical wedge grips were used for the static testing and hydraulic grips for the fatigue tests.

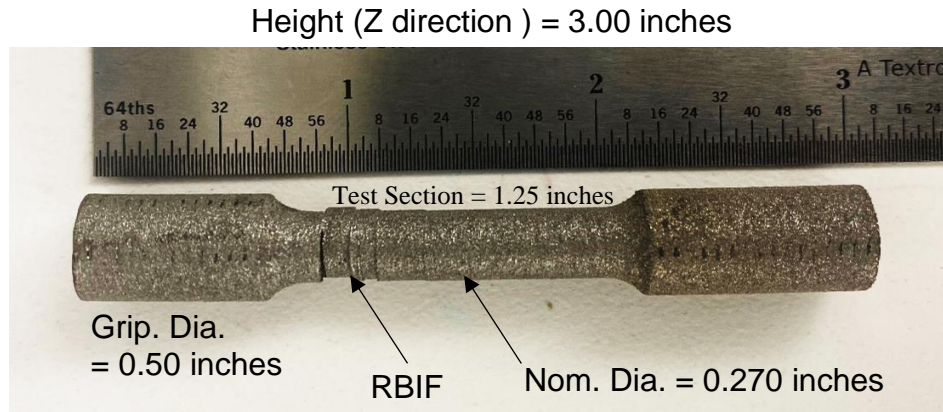


Figure 25. Overall dimensions of Ti-6Al-4V Specimens made using EOS M290

Table 6. Project Outline and Task Descriptions

Item	Category	Detail Task Description
1	Design/Build (Baseline)	Design and Build Baseline Ti-6Al-4V (as-built) specimens without flaws, no post process
2	Design/Build (Flawed)	Design and Build specimens with recoater blade interference flaws (RBIF).
3	Fatigue Test (Both)	Fatigue test the baseline specimens verifying similarity to existing literature
4	FEM (Flawed)	Fatigue test specimens with interference flaws; Use Finite Element Modeling to predict failure location and Kt
5a	Crack Initiation Analysis Review	Results Review & Analysis:
5b		Plot S-N curves of results from Fatigue Tests of Baseline and Flawed Specimens
5c		Identify S-N, Soderberg/Goodman fatigue knock-down-factors (KDF) for RBIF
5d		-6Al-4V specimens compared to baseline
5e		Compare fatigue origins to predictions and fracture surface microstructure of the baseline (as-built) and flaw specimens

4.1.1 Baseline Specimens Build and Test

The specimens were designed per the requirements of ASTM E466 [103]. A total of 6 cylindrical baseline specimens with a test section diameter of 0.270-inches and 3.00-inch height. Solid modeling was done using Solidworks® software. The CAD file was imported into .SLDPRT format into the Materialise Magics® software for preparation to build together with other flat specimens and C(T) specimens at different orientations that were planned together with this build as shown in Figure 26 below.

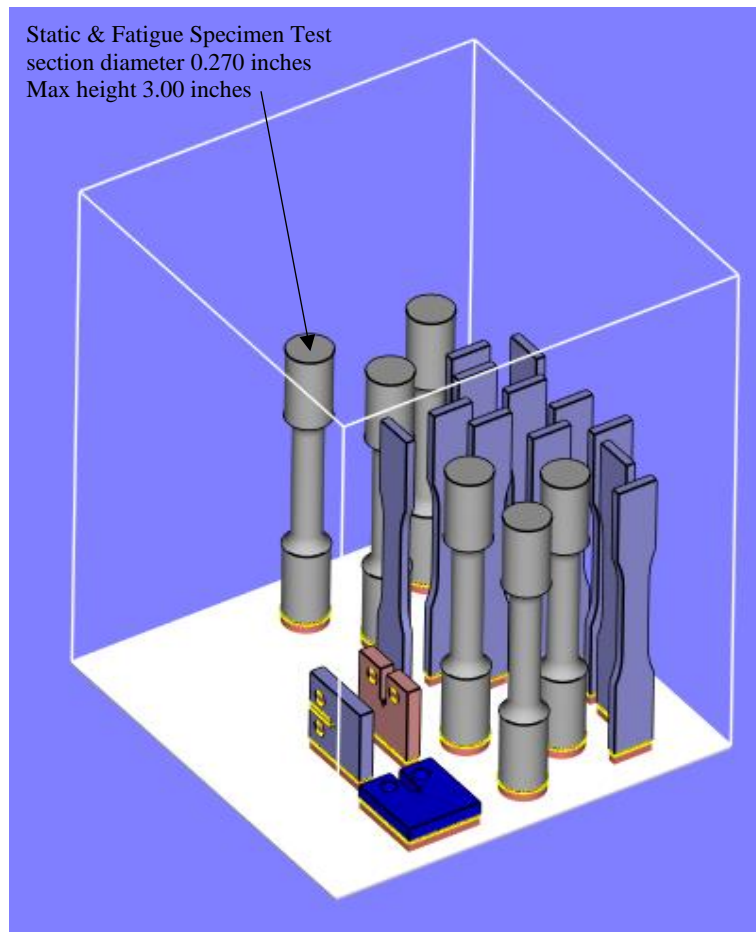


Figure 26. Initial Layout of Specimens in Build Chamber

The specimens were built at UTA using the L-PBF process and the EOS m290 set to the build parameters shown in Table 7. Other than mechanical removal from the build plate using band saw, there were no other post process surface treatment or stress-relief heat treatment applied.

Table 7. Build specification for baseline

Machine Model	Powder Description	Laser Power (W)	SS	HS	LT	E	Scan Strategy
EOS m290	EOS Ti64 Grade 5	280	1200.0	140.00	30	55.56	Stripes

While a hard recoater blade made from high strength steel was used for the baseline builds (no RBIF) in the EOS m290 machine, it is recommended to use a soft recoater blade made from silicon, rubber, or soft carbon fiber to prevent RBIF [122]. Supports were maximized to help also with heat dissipation due to the high aspect ratio and specimens were built at an angle to the recoater blade [122], see Figure 27. Layer spacing was set at 35-40 μ m. These were tolerances chosen to prevent recoater blade interference.

Additionally, the baseline specimens were better interspersed thus minimized the occurrence of RBIF as recommended [123]. Another reason why RBIF was not an issue for this build was that the interference gap was set at 100% meaning that each new layer deposited fully cleared the recoater blade without interference as illustrated in Figure 29.

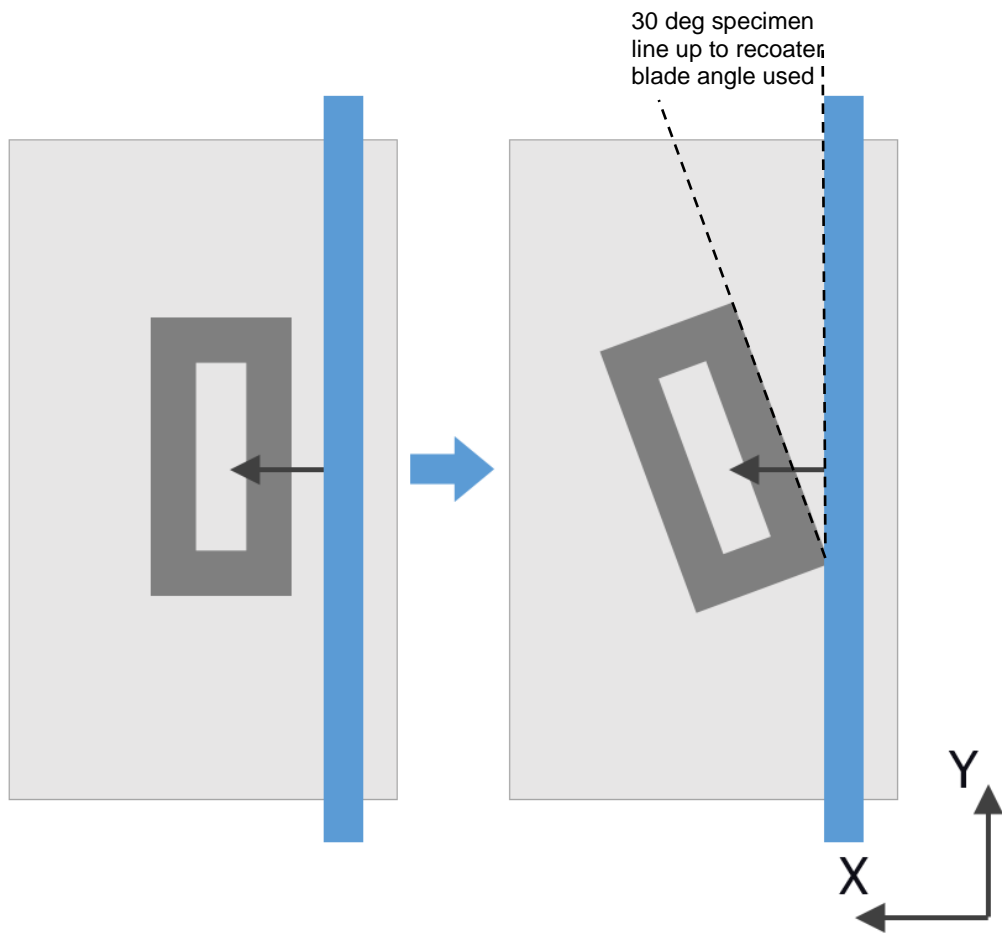


Figure 27. Baseline specimen lineup orientation on build plate versus recoater blade

4.1.2 Flawed Specimens Build and Test

These specimens were built with the same primary build parameters as the baseline specimens except that they were not staggered on the build platform, did not have increased support structures for increased heat dissipation to prevent distortion and their orientation towards the recoater blade was almost perpendicular and further did not follow recommendations shared in section 2.1.1.1.3. The aspect ratio for this build is $h/d = 3.00 \text{ inch}/0.270 = 11.1$, a high aspect ratio, and the tolerance overlap settings was less than 100% with a high strength steel hard recoater blade, hence assuring RBIF formation.

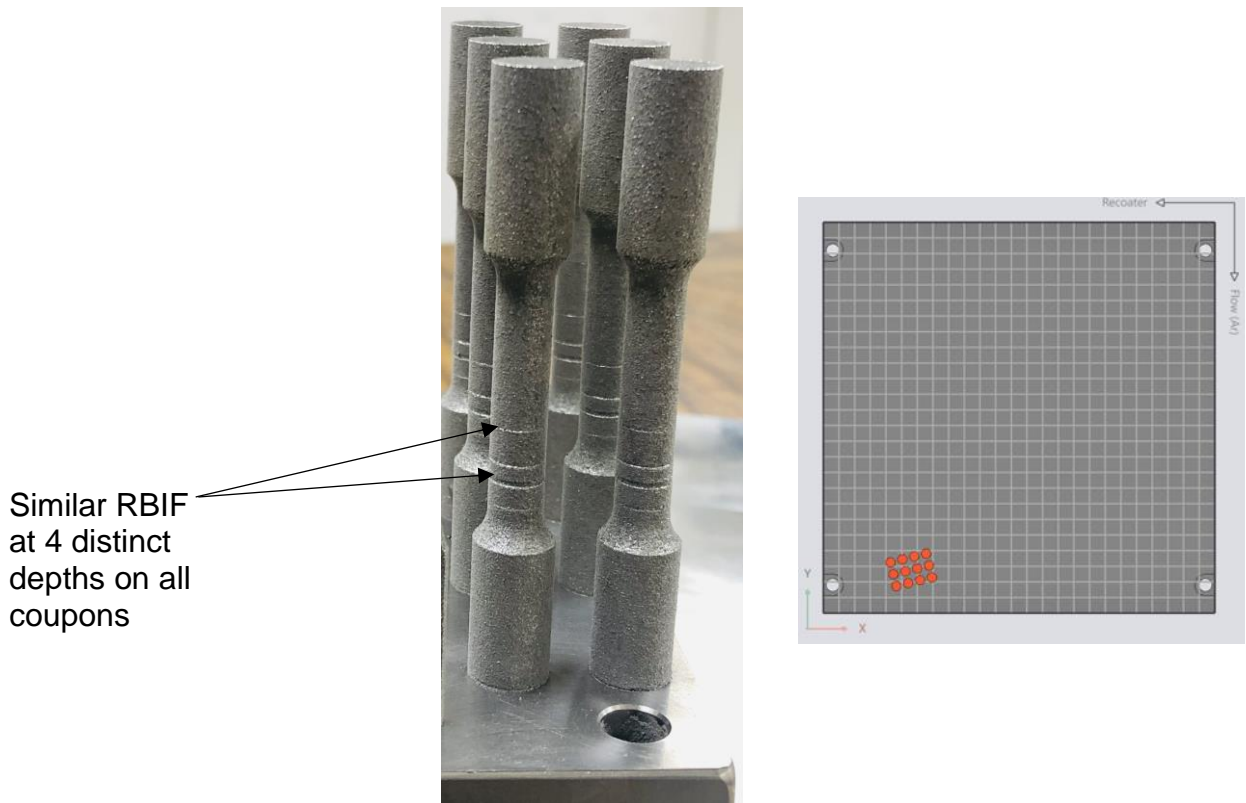


Figure 28. As-built test specimens with Recoater Blade Interference Flaws (RBIF)

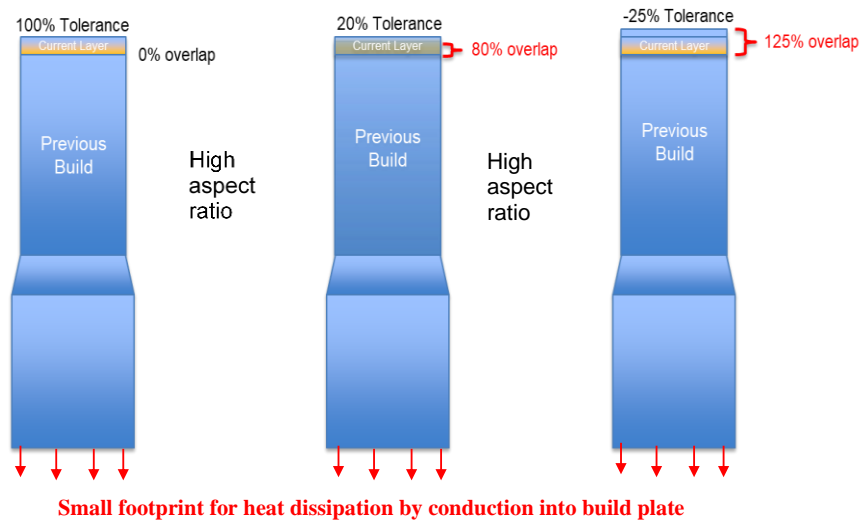


Figure 29. Tolerance setting and high aspect ratio challenge with RBIF

4.2 Stress and Fracture Failure Location Prediction

Predicting the state of stress and critical locations (likely crack initiation site) to further support selection of fatigue test loads requires understanding the application of strength of materials, elasticity and fracture mechanics theories and making simplifying assumptions to support AM analysis. Due to the challenge of anisotropy resulting from type of microstructure formations resulting from the L-PBF process [147], this study considered orthotropic material properties for the simplified prediction of failure. Material strength properties have been shown to be lowest in the loading along the Z build direction [147].

Due to the differences in the geometries of the baseline (no-flaw) specimens and the specimens with RBIF, analysis the specimens with no flaws was completed first with a simple use of used stress equation 4 with no bending terms due to misalignment. The specimen with RBIF required with misalignment required was analyzed more using FEM however, the state of stress was also checked using closed form solutions.

For the cylindrical test specimens built, the state of stress the element at the tangency of the outer radius may be represented in terms of cylindrical coordinates using the anisotropic part of the stress tensor ($\nabla^*\tau$) as , where τ is the deviatoric stress tensor, that gives rise to equations 11, 12 and 13 below.

$$\frac{\partial \tau_{rr}}{\partial r} + \frac{\tau_{rr} - \tau_{\theta\theta}}{r} + \frac{1}{r} \frac{\partial \tau_{r\theta}}{\partial \theta} + \frac{\partial \tau_{rz}}{\partial z} + F_r = 0 \quad (\text{Equation 11})$$

$$\frac{\partial \tau_{r\theta}}{\partial r} + \frac{1}{r} \frac{\partial \tau_{\theta\theta}}{\partial \theta} + \frac{\partial \tau_{\theta z}}{\partial z} + \frac{2\tau_{r\theta}}{r} + F_{\theta} = 0 \quad (\text{Equation 12})$$

$$\frac{\partial \tau_{zr}}{\partial r} + \frac{1}{r} \frac{\partial \tau_{\theta z}}{\partial \theta} + \frac{\partial \tau_{zz}}{\partial z} + \frac{\tau_{zr}}{r} + F_z = 0 \quad (\text{Equation 13})$$

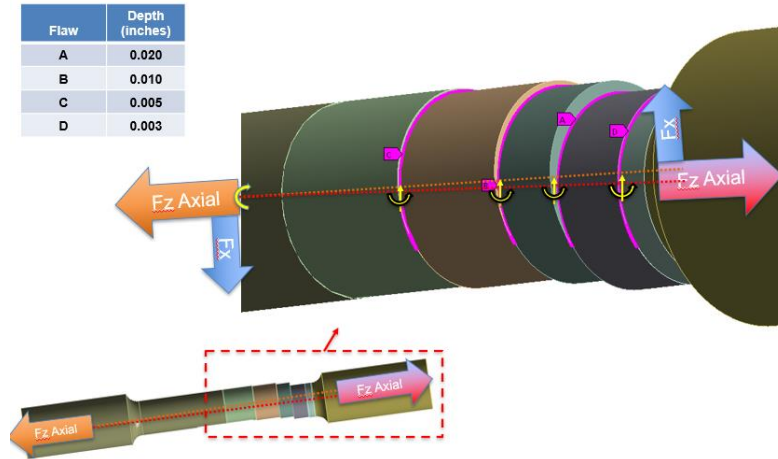


Figure 30. FEM Geometry and Modeling of the RBIFs

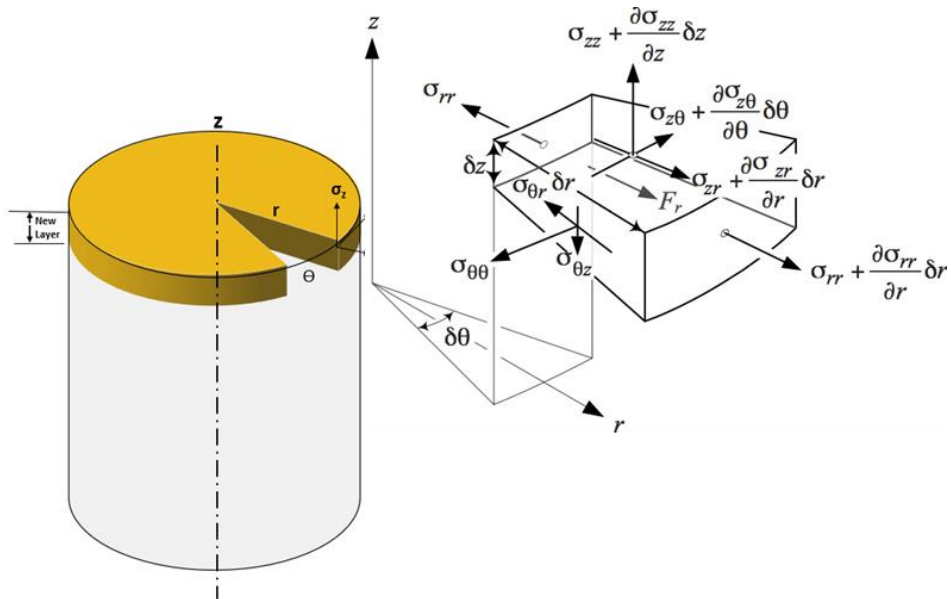


Figure 31. State of Stress in Test Specimens using Cylindrical Coordinates

Solutions to the partial-differential equations presented in 11, 12 and 13 for the flawed specimen can be accomplished with simplification of the material compliance properties and using numeric Runge-Kutta methods for the partial differential equations or simplified ordinary differential equation solution by Green's theorem for initial and boundary-value integration such as implemented finite element codes as ANSYS®. Recent updates to ANSYS® with addition of the ANSYS® Additive suite were not available for use in this study, however, online literature indicates the software has the full-physics solution modeling and the strain-based modeling which requires a calibration from an actual build.

The standard ANSYS® finite element model package was used to model the flawed specimen with accurate 3D of the flaws incorporated from reverse-engineering scans of the resulting specimens using UTA's Faro Arm®. The goal of this FEM was to identify the highest K_T location of the multiple flaws and thus to gain understanding of the maximum stress with each proposed fatigue test load condition. Further the model was used to hand analysis approximations. It must be understood that while this version of ANSYS (without the additive suite) was not readily capable of vary material properties on multiple layers to accurately predict the stress at all areas of the model but the hand calculations indicated a good relationship at the critical points for given fatigue test load cases. The model was constructed based on the measurements taken from the specimen with RBIF as shown in Figure 30 and Figure 32. The mesh used hexahedral elements (8 node) with the mesh density increased around the center test section where the recoater blade impact flaws were concentrated with the sharp stair-step flaws (RBIF), these were the areas expected to result in highest K_T (see Figure 33).

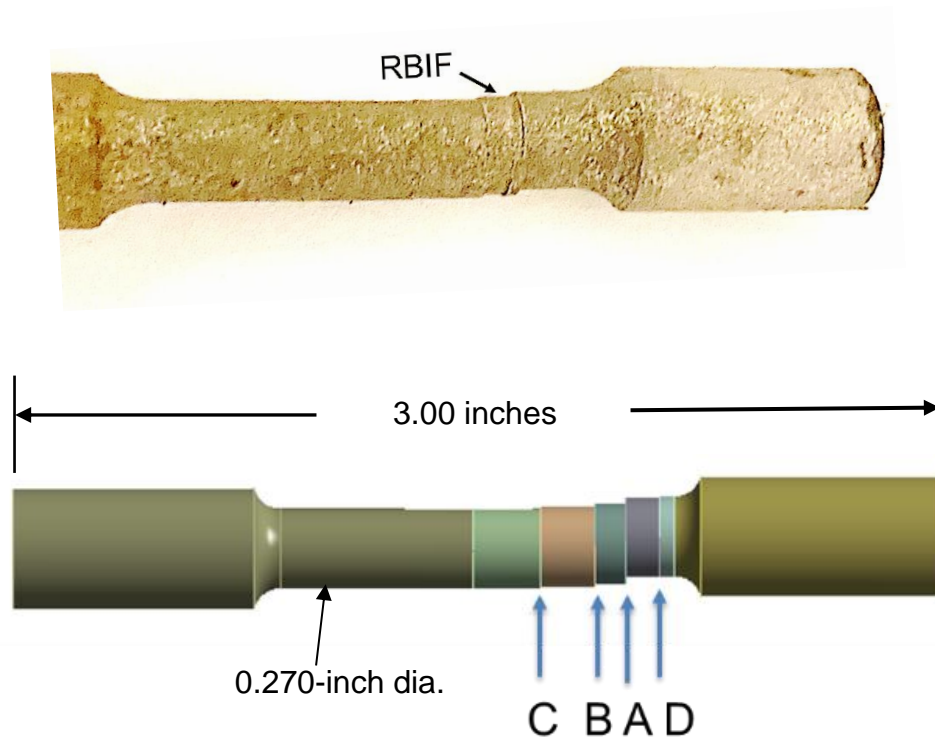


Figure 32. Fatigue Test Specimen with Recoater Blade Interference Flaw (RBIF)

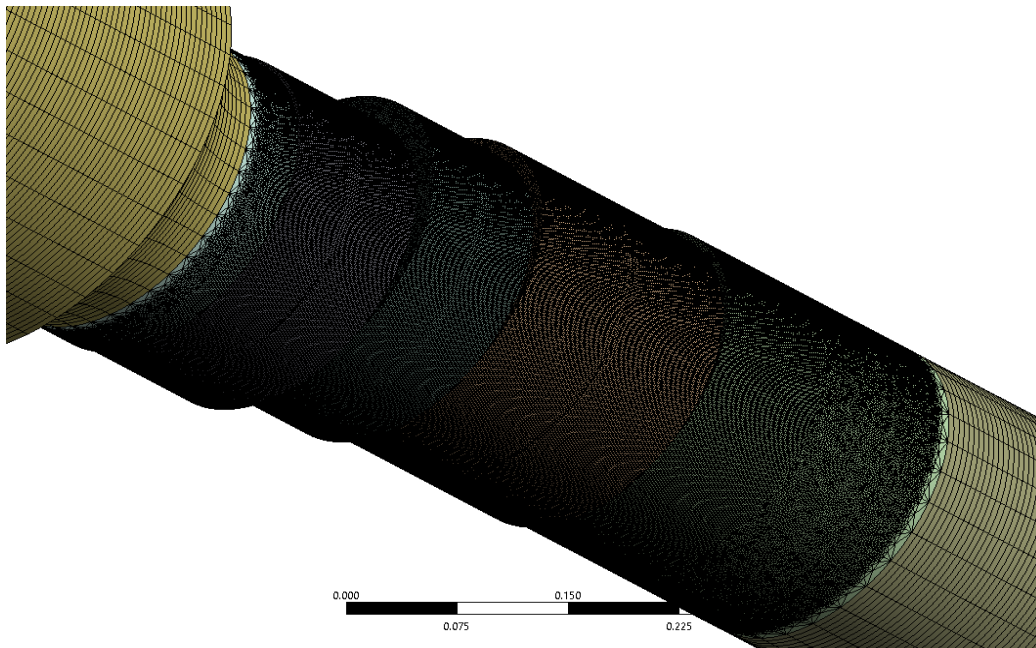


Figure 33. FEM showing Increased Mesh Density in Center (Flaw) Section

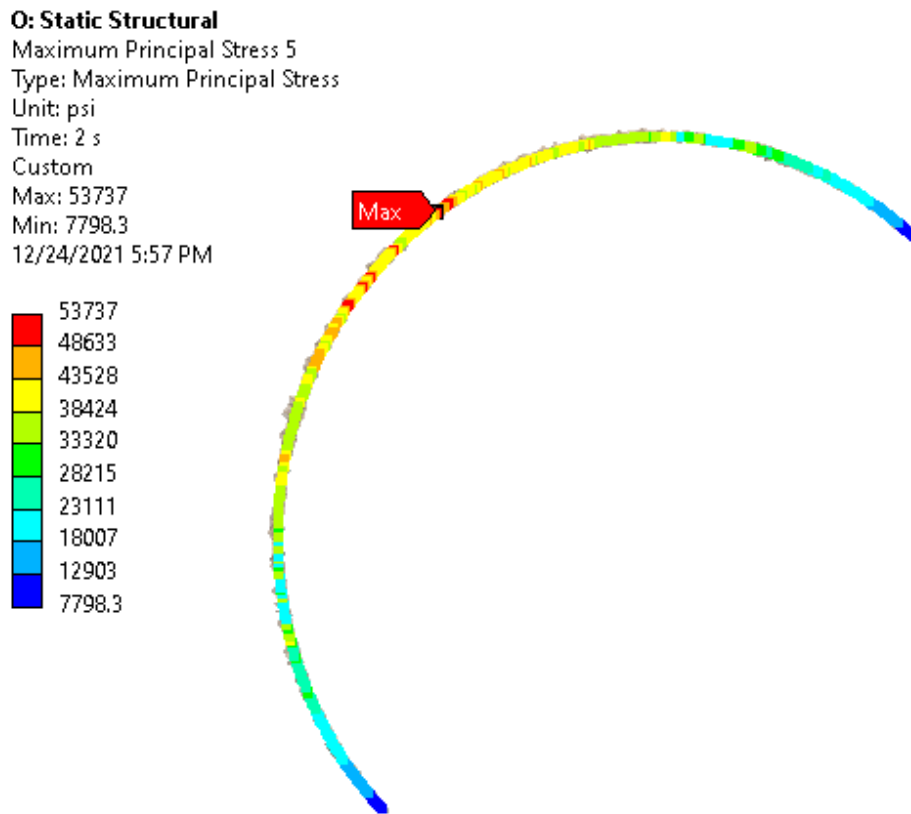


Figure 34. FEM Results at the highest stressed RBIF (Location A)

Results shown in Figure 34 indicate that the largest K_T occurs at flaw location A (0.020-inch step). The nominal stress at the net section area of 0.0574 in² with an applied axial load of 442 lb. (FEM load step 2) is calculated as 7,798 psi. The actual local stress measured at flaw location A is 53,737 psi. Hence the highest calculated K_T is given in Equation 14 as:

$$K_{T(\text{location A})} = 53,737 \text{ psi} / 7,798 \text{ psi} = \underline{6.9} \quad (\text{Equation 14})$$

This notch factor for the RBIF is severe enough and is predicted to result in most of the CIS for the fatigue specimen failures at this stress concentration point with a significant reduction in fatigue strength.

5 Results and Discussion

The raw test results from the total of 12 specimens, 6 baselines (as built without RBIF), and 6 flawed specimens tested at AADFW Inc., a NADCAP® accredited facility locate in Hurst, Texas, are presented in Appendix A (for static results) and B (for fatigue test results). All tests were witnessed by the author and the Satec™ 120 Hydro-mechanical machine used to perform the testing met calibration requirements.

5.1 Results

5.1.1 Static Test Results

The static testing was completed per ASTM E-8 with the results shown in Table 8 and a copy of the test certificate is presented in Appendix A. The baseline specimen with no flaws failed in the upper test gage section at the tangency to the transition radius. The flawed specimen failed at the location of the maximum flaw depth; Location A shown in Figure 30.

Table 8. Static Test Results for Ti-6Al-4V Baseline (NF) and RBIF (F) Specimens

<u>Equipment</u>				<u>Method</u>					
Tensile: Satec 120 HVL, SN:1290				ASTM E8					
Bar Type: Round			Yield Criterion: 0.2 % Offset			Gage Length: 1.0 "			
Specification: N/A			Rev:						
Material:			Elongation: % in 4D						
Sample Req:	----- Dimensions (in) -----			---- Ultimate ----		-----Yield -----		Elong	R. A.
		Dia.	Dia Final	(lbs)	(ksi)	(lbs)	(ksi)	(pct)	(pct)
F		0.269	0.267	8746	154	7627	134	1.3	1.5
NF		0.270	0.243	10633	186	8766	153	8.0	19

5.1.2 Baseline Specimen Fatigue Test Results

The baseline as built specimens, with not post process heat treatments for residual stress relief, are presented in Table 9. These results were also plotted on an S-N curve in terms of axial stress as the ordinate and cycles to failure (plotted in log scale) in the abscissa. The maximum stress amplitude (MPa) is shown in Figure 35 and Figure 36 shows it in terms of oscillatory stress. The stresses were calculated per Equation 3. Specimen 5 was terminated with no failure at 7,319,219 cycles when the lab confirmed instruction that any specimen over 3 million cycles would be considered a runout for purposes of this study.

Table 9. Fatigue Test Results for Baseline Ti-6Al-4V Specimens

Baseline Spec	R - Ratio	Max Load (lb)	Min Load (lb)	Max Stress (psi)	Max Stress (ksi)	Max Stress (MPa)	Min Stress (psi)	Mean Load (lb)	OSC load (lb)	Mean stress (psi)	OSC stress (psi)	OSC stress (MPa)	Cycles to Failure
Baseline 1	0.1	4500	450	78392	78	540	7839	2475	2025	43115	35276	243	6932
Baseline 2	0.1	3800	380	66197	66	456	6620	2090	1710	36409	29789	205	9345
Baseline 3	0.1	2000	200	34841	35	240	3484	1100	900	19162	15678	108	84295
Baseline 4	0.1	1500	150	26131	26	180	2613	825	675	14372	11759	81	180532
Baseline 5*	0.1	750	50	13065	13	90	1307	400	350	7186	5879	41	7319219

*Suspended test point - non-failure runout

After testing, all specimens were kept in appropriate storage condition with their crack surfaces maintained from mating or having any interference that would smear or cause any defect that may alter their crack surfaces which would have hampered further fractographic studies.

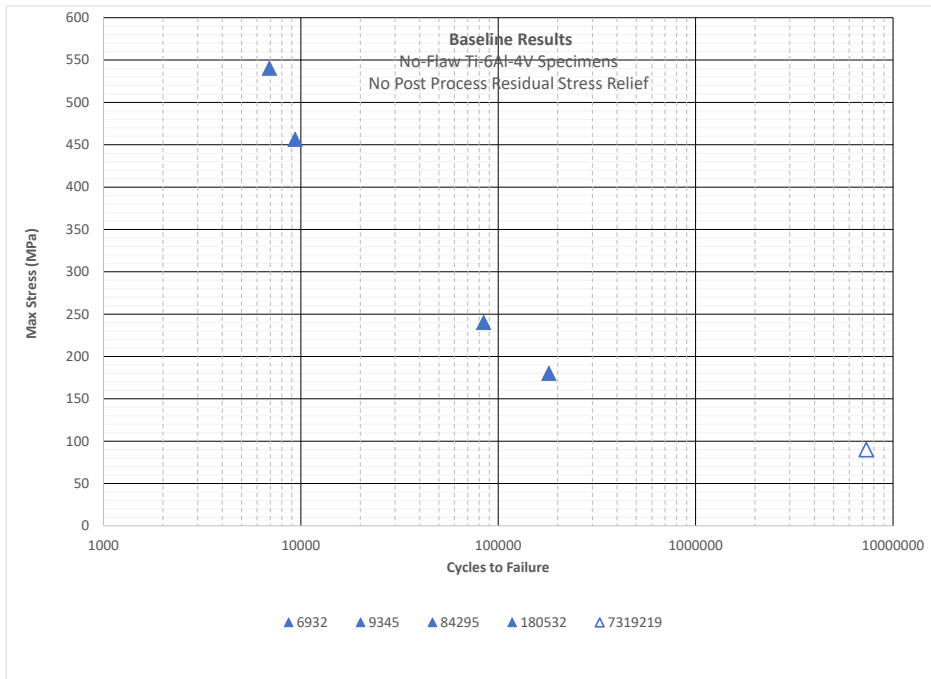


Figure 35. Baseline, Ti-64 Grade 5, As-Built, No-RBIF, with Residual Stress, R=0.1, Maximum Stress (MPa)

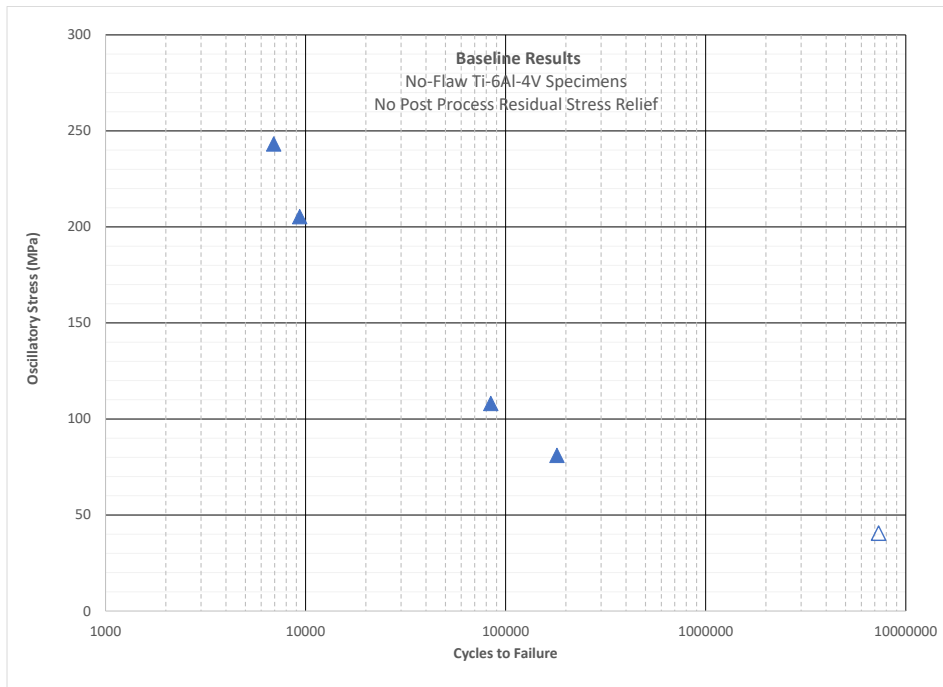


Figure 36. Baseline, Ti-64 Grade 5, As-Built, No-RBIF, with Residual Stress, R=0.1, Oscillatory Stress (MPa)

5.1.3 Flaw Specimen Fatigue Test Results

The fatigue test results for the specimens with RBIF and no residual stress, are presented in Table 10. These results were also plotted on an S-N curve in terms of axial stress as the ordinate and cycles to failure (plotted in log scale) in the abscissa. The maximum stress amplitude (MPa) is shown in Figure 35 and Figure 36 shows it in terms of oscillatory stress. Specimen 1 and 2 of the flawed specimens were inadvertently run at the same load level but help provide an understanding of the scatter in the results, at least for the low cycle region. The stress was calculated per Equation 3. Specimen 5 was terminated with no failure at 3 million cycles.

Table 10. Fatigue Test Results for Ti-6Al-4V Specimens with RBIF

FLAWED Spec	R - Ratio	Max Load (lb)	Min Load	Max Stress (psi)	Max Stress (ksi)	Max Stress (MPa)	Min Stress (psi)	Mean Load (lb)	OSC load (lb)	Mean stress (psi)	OSC stress (psi)	OSC stress (MPa)	Cycles to Failure
Flawed 1	0.1	4500	450	78392	78	540	7839	2475	2025	43115	35276	243	589
Flawed 2	0.1	4500	450	78392	78	540	7839	2475	2025	43115	35276	243	1168
Flawed 3	0.1	2000	200	34841	35	240	3484	1100	900	19162	15678	108	12474
Flawed 4	0.1	1500	150	26131	26	180	2613	825	675	14372	11759	81	38099
Flawed 5*	0.1	500	50	8710	9	60	871	275	225	4791	3920	27	3000000

*Suspended test point - non-failure, runout

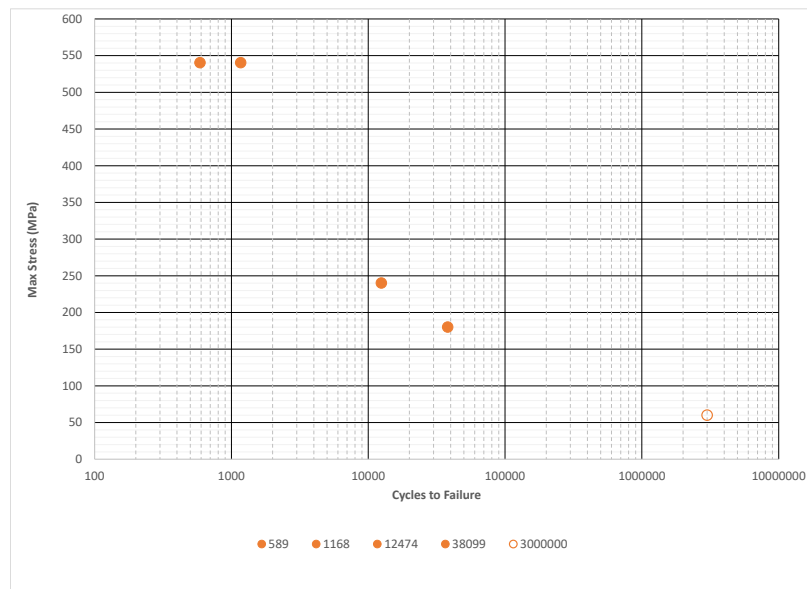


Figure 37. Fatigue Test Results of Ti-64 Grade 5 with RBIF and Residual Stress, R=0.1, Maximum Stress (MPa)

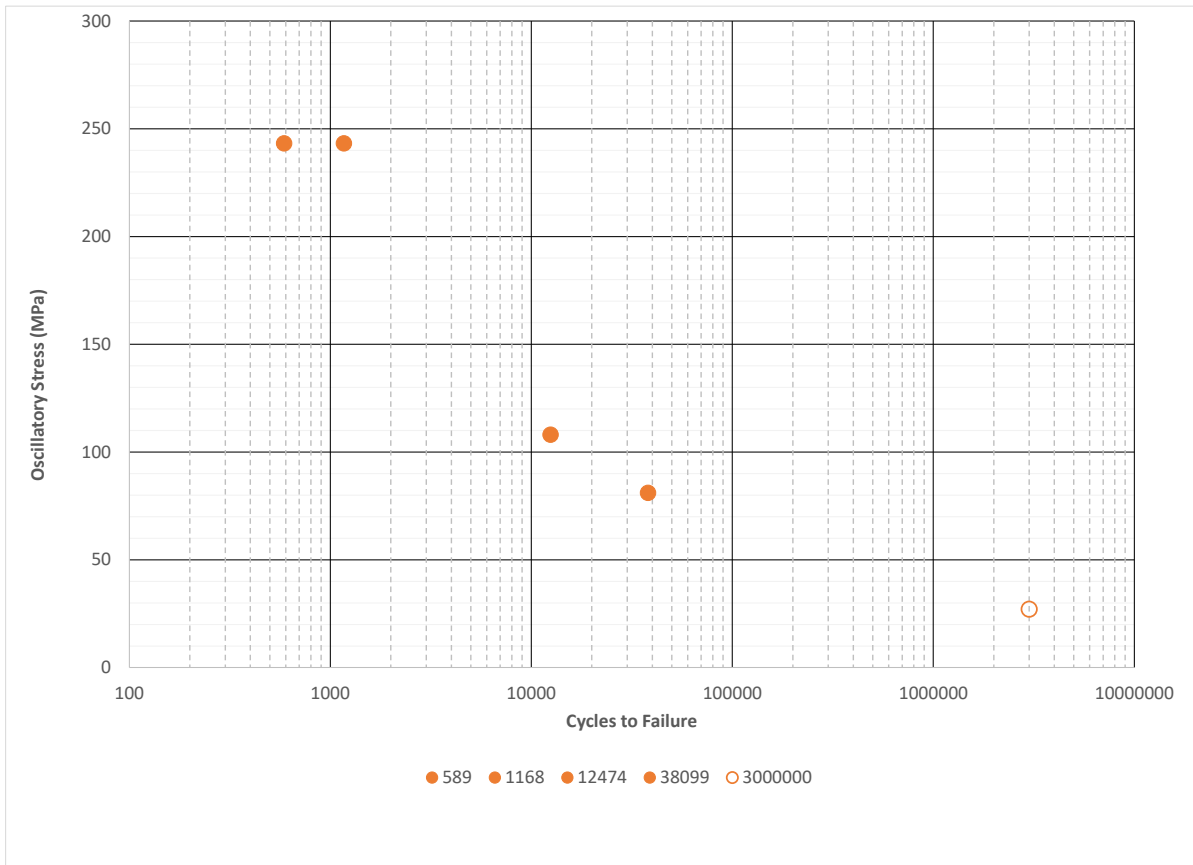


Figure 38. Fatigue Test Results of Ti-64 Grade 5 with RBIF and Residual Stress, R=0.1, Oscillatory Stress (MPa)

5.2 Discussion

Analysis of the results obtained indicates a significant (non-trivial) reduction in mean fatigue strength of the RBIF (flawed) specimens compared to the baseline as-built specimens with no RBIF. Further, review of the results with S-N curve fitting and comparison to other as-built Ti-6Al-4V fatigue data as well as including the additional comparison of stress relief reduction through heat treatment. Soderberg diagram plots will also provide the necessary adjustments of mean to oscillatory stress for extrapolation of the results from F_{TY} yield on the x-intercept, linearly to the $R=-1$ y-intercept through the test point obtained at $R=0.1$.

5.2.1 Static Strength Results Review

Results in Table 8 from the static tests of one baseline (no flaw) specimen and one specimen with RBIF were tested and analysis of the results is summarized in Table 11. The static test results are noted to be accurate as evidenced in the certificate included in Appendix A.

Table 11. Review of Static Test Results for Ti-6Al-4V L-PBF

Specimen	F _{ty} (yield)		F _{tu} (ultimate)		Elongation
	Mpa	ksi	Mpa	ksi	%
RBIF	924	134	1062	154	1.3
Baseline	1055	153	1282	186	8
<i>KDF</i>	1.14		1.21		6.15
<i>% change</i>	-12%		-17%		-84%

The results are in line with what was expected, as shown by other studies [6, 147, 148]. It is noted that the baseline (as-built, without stress relief) yield strength in Z direction is higher than the one with flaws, and that both results (with and without flaws) were higher than wrought Ti-6Al-4V beta annealed (which has $F_{TY} = 120$ ksi per MMPDS [100]). The reason is primarily because the lack of heat treatment in the as-built specimens leaves them in a brittle state resulting in martensitic

α' grain morphology resulting in higher static strength but lower elongation and fatigue strength as seen in the results in Table 11. A summary of static parameters from Reference [6] is also shared in Table 12 for further comparative studies with the results of this study using Soderberg.

Table 12. Table of Static Parameter Results From Comparable Data [6]

Parameter		Value
Ultimate strength	σ_U	1140 MPa
Yield strength	σ_Y	1070 MPa
Young's Modulus	E	110 GPa
Plain strain fracture toughness	K_{IC}	73 MPa m ^{1/2}
Crack propagation threshold	ΔK_{th}	3.48 MPa m ^{1/2}

The fatigue test results are noted to be accurate as evidenced in the certificate included in Appendix B. The baseline results (without flaws) were compared in terms of maximum stress (MPa) to the flawed specimens as well as oscillatory stress in Figure 39 and Figure 40, respectively.

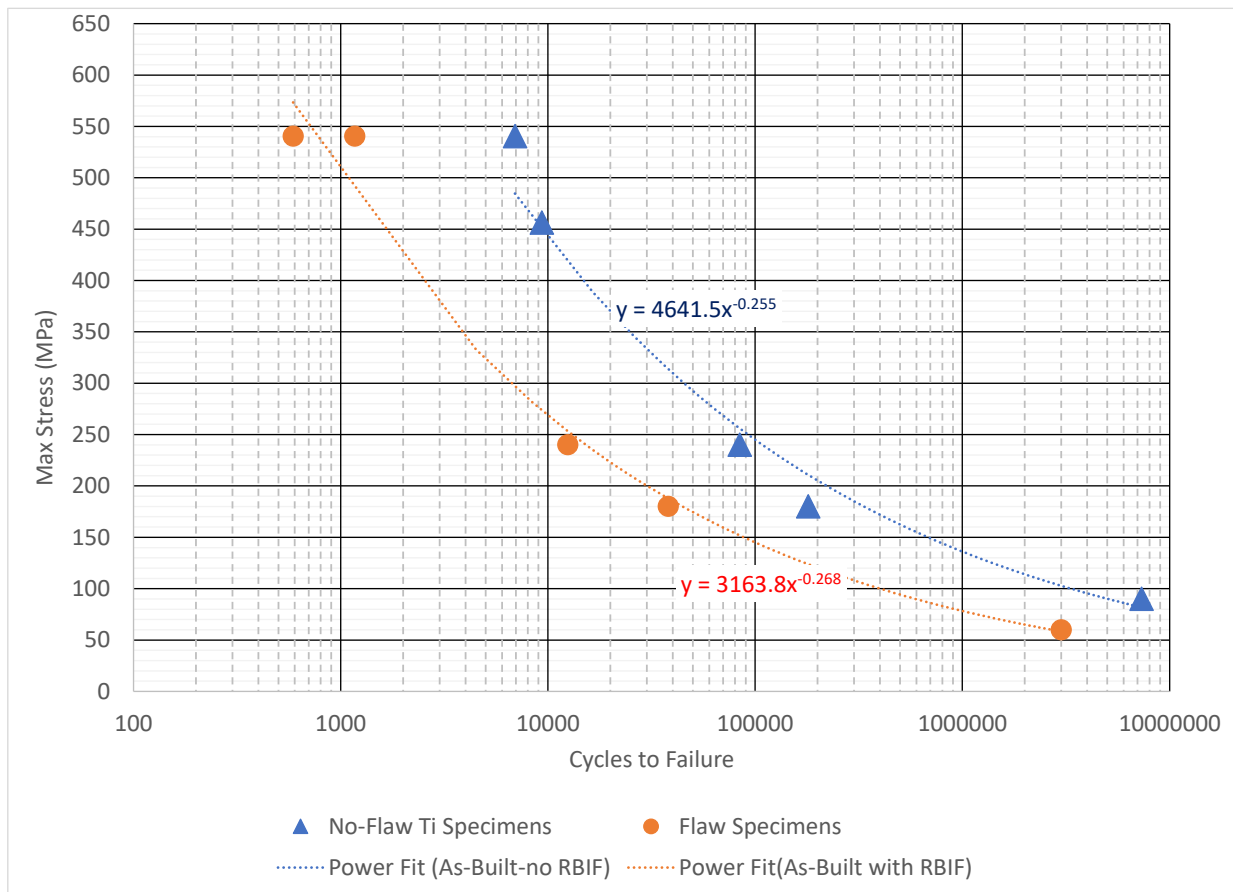


Figure 39. Fatigue Test Results of Ti-6Al-4V with Baseline and RBIF, R=0.1, Max Stressed

The mean fit curve through the baseline and RBIF data is given in terms of the equations:

$$y \text{ (Mpa)} = 4641.5x^{-0.255} \quad \text{Baseline mean fit} \quad \text{(Equation 15)}$$

$$y \text{ (Mpa)} = 3163.8x^{-0.268} \quad \text{RBIF mean fit} \quad \text{(Equation 16)}$$

Both the baseline and RBIF specimens did not have post process heat treatment for residual stress relief, nor other surface treatment, thus the reduction factor in fatigue strength is based on cracks initiation sites (CIS) originating at the RBIF defects (more details on the CIS in Section 5.3).

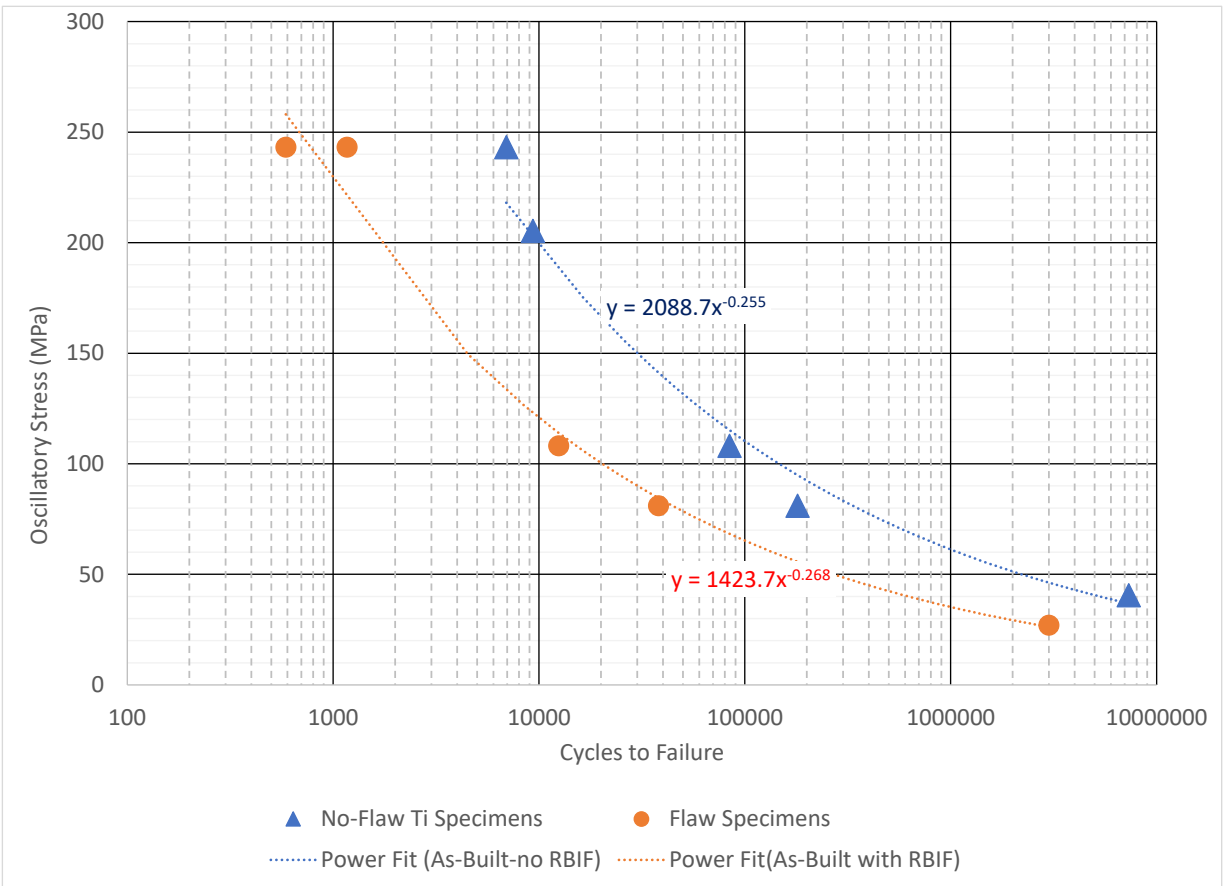


Figure 40. Fatigue Test Results of Ti-6Al-4V with Baseline and RBIF, R=0.1, Osc. Stress

Further, S-N comparisons were made using other literature data from similar L-PBF process-built specimens. The comparison with the data from Reference [6] was especially meaningful as it tested Ti-6Al-4V specimens built using an EOS-M290 L-PBF process with closely matching build parameters (200 W laser power, layer thickness of 30 μ m, energy density of 45.33 J/mm³ under Argon atmosphere) all closely comparable to this study’s parameters in Table 7. However, the specimens in Reference [6] were stress relieved at 650°C for 3 hours, with subsequent argon cooling as recommended in Reference [148]. S-N comparison of the as-built results is shown Figure 43 while the polished data is added to the summary tabulated comparison in Table 12.

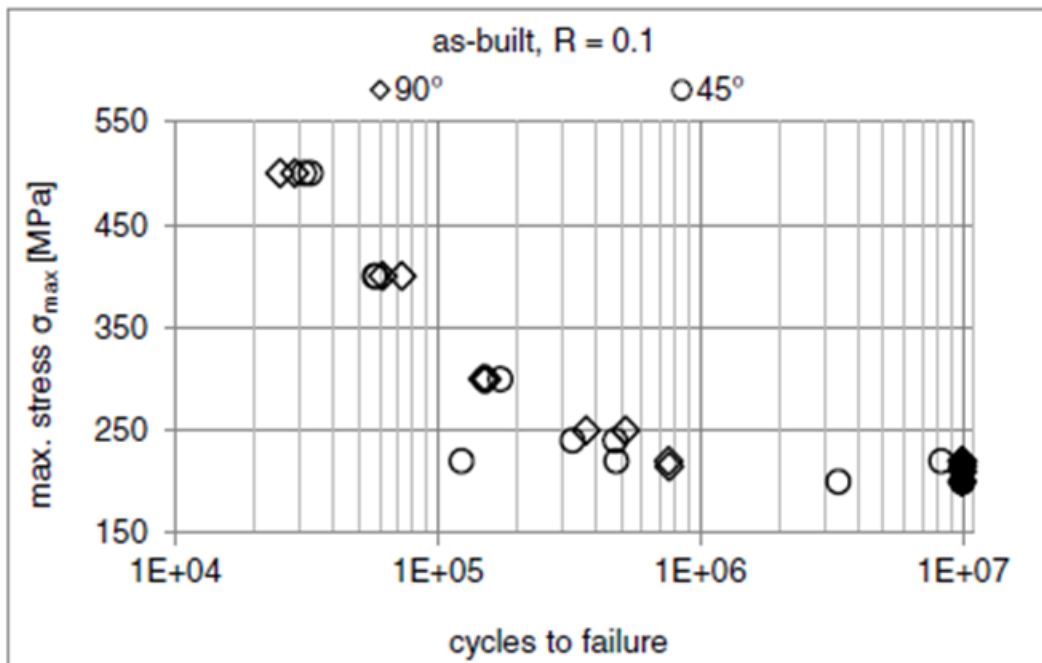


Figure 41. Ti-6Al-4V L-PBF Fatigue Test Results for as-built specimens at R=0.1, Stress Relieved at 650°C for 3 hours [6]

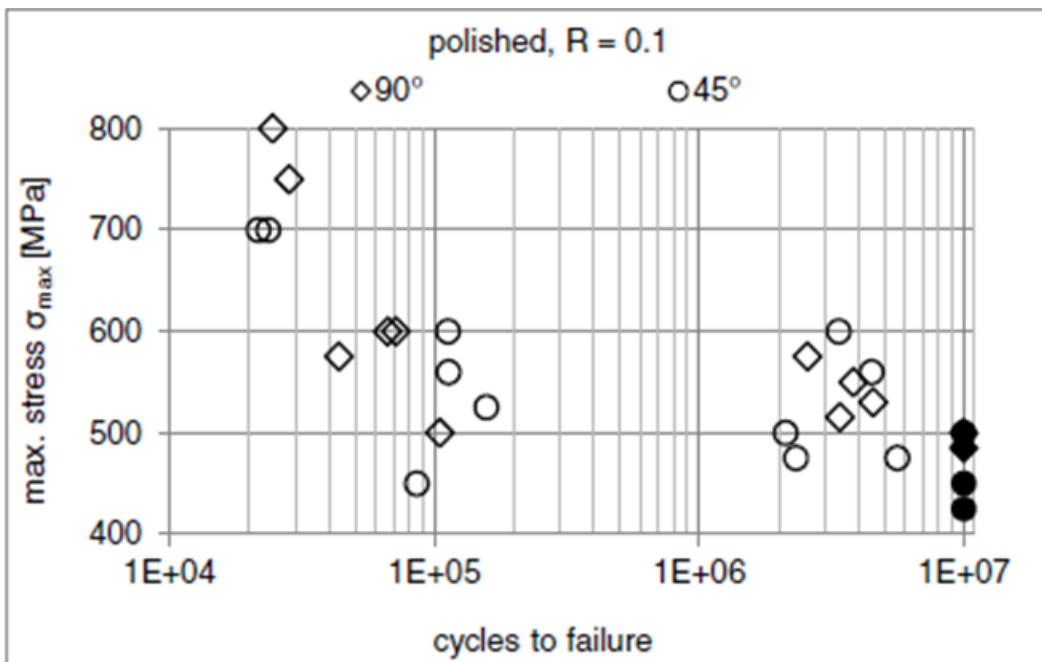


Figure 42. Ti-6Al-4V L-PBF Fatigue Test Results for Polished Surface specimens at R=0.1, Stress Relieved at 650°C for 3 hours [6]

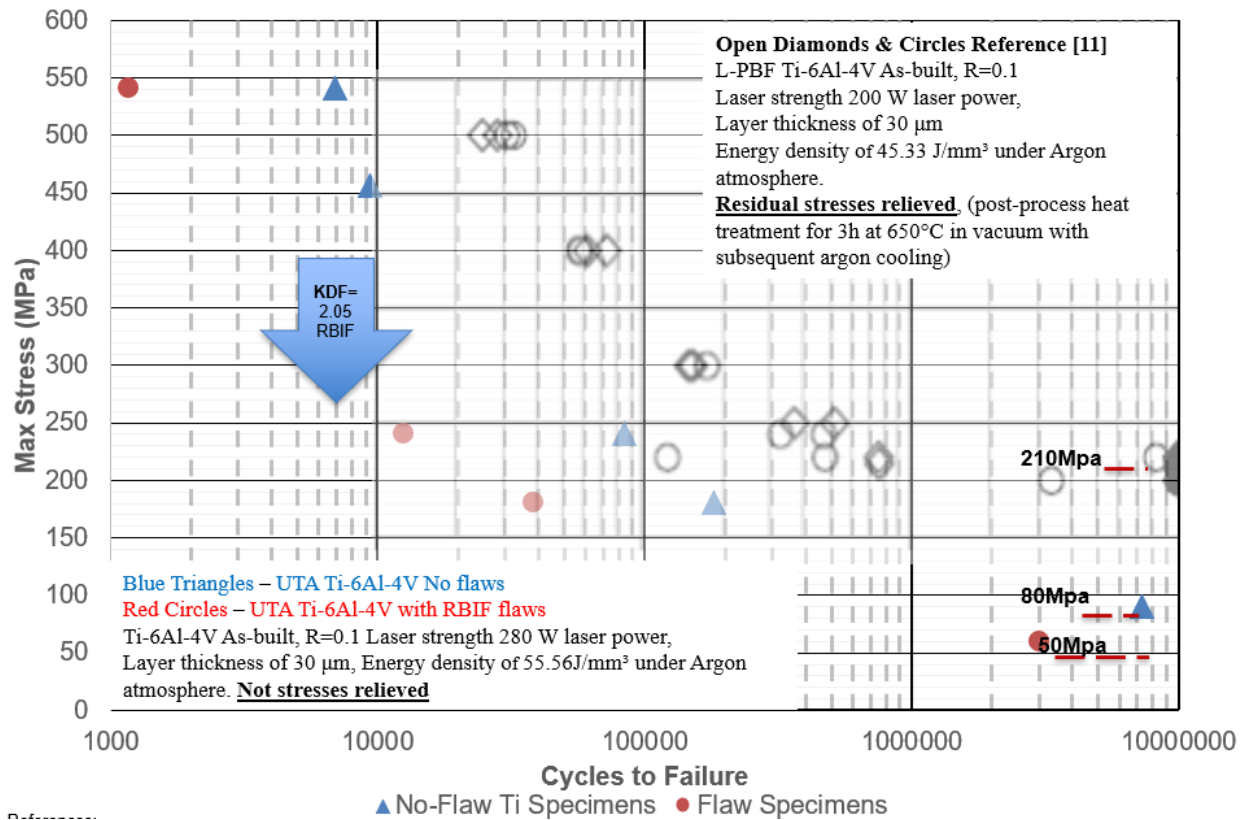


Figure 43. Fatigue Test Results comparison of current testing and Ref [6] as-built stress relieved specimens, max stress at R=0.1

Comparison to wrought Ti-6Al-4V annealed per AMS4928 [105] was also made using data from Reference [100] which overlaid with the results of this testing in Figure 45. As can be clearly noted, this data is best compared on Soderberg as the MMPDS Reference [100] was tested at various means and not the same R-ratio as the data generated in this study (R=0.1).

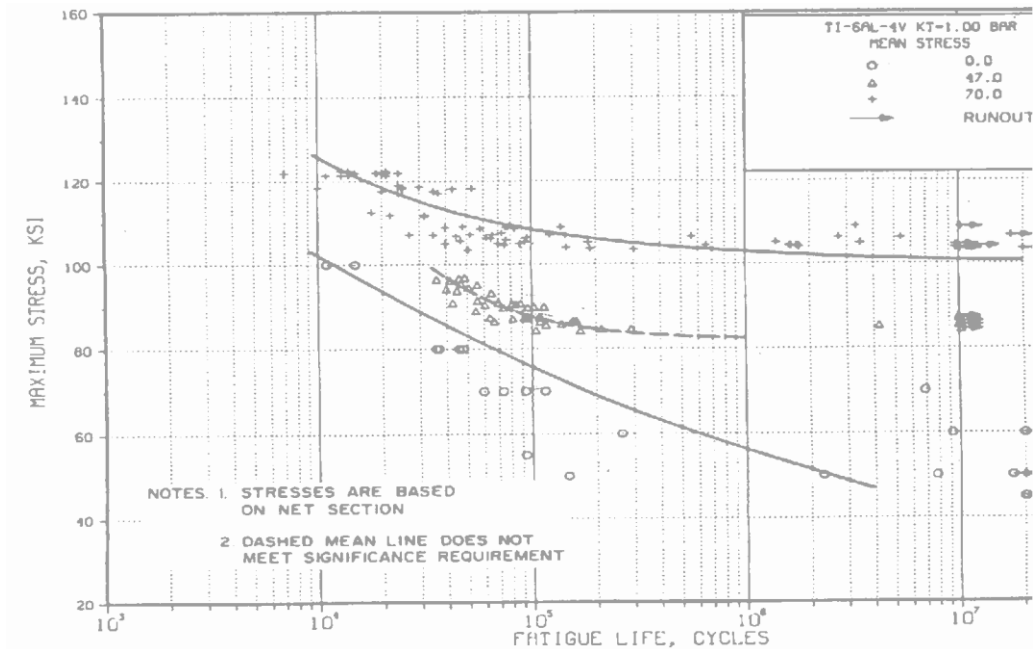


Figure 44. Wrought Ti-6Al-4V Annealed, smooth specimens (Kt = 1.0) [100]

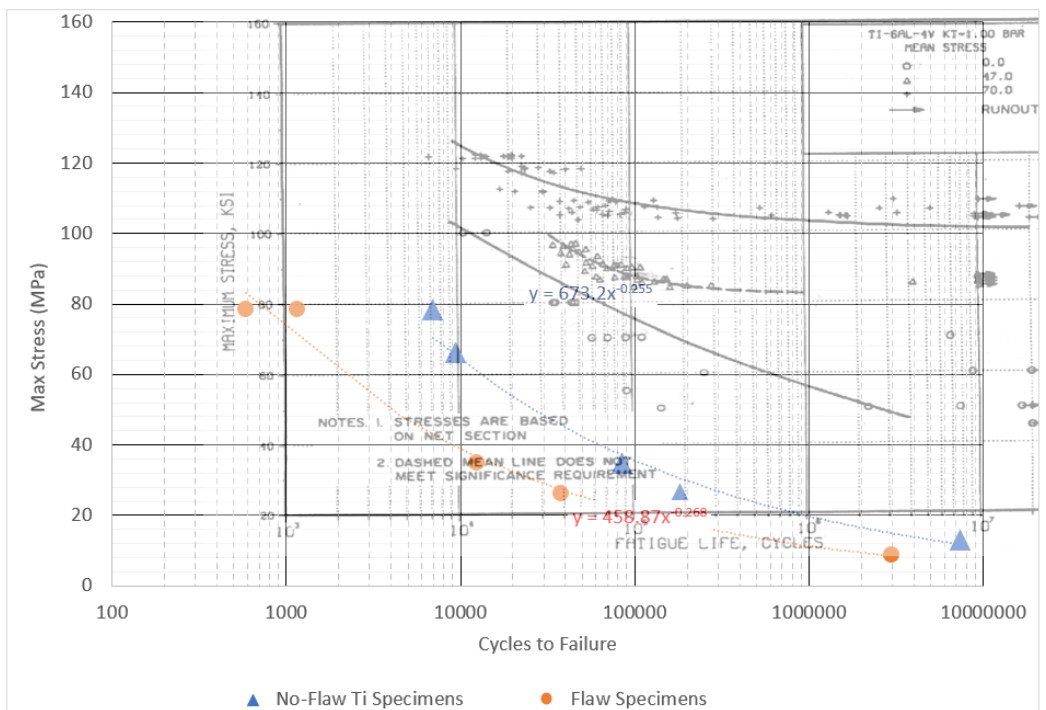


Figure 45. Test Results S-N comparisons Ti-6Al-4V annealed bar per AMS4928 vs L-BPF with residual stress

5.2.2 Soderberg comparison

Further deductions on the results were made based on comparisons using the Soderberg diagram which accounts for mean stress across various R-ratios providing the allowable stress back to the Y-intercept (R=-1). Section 3.1 discusses the Soderberg further and shows it's conservativeness over the Goodman line or Gerber curve, as illustrated in Figure 46. The usefulness of this analytical tool, combined with Miner's rule in performing deterministic safe-life calculations, as detailed in FAA guidance in Reference [22], cannot be over-emphasized.

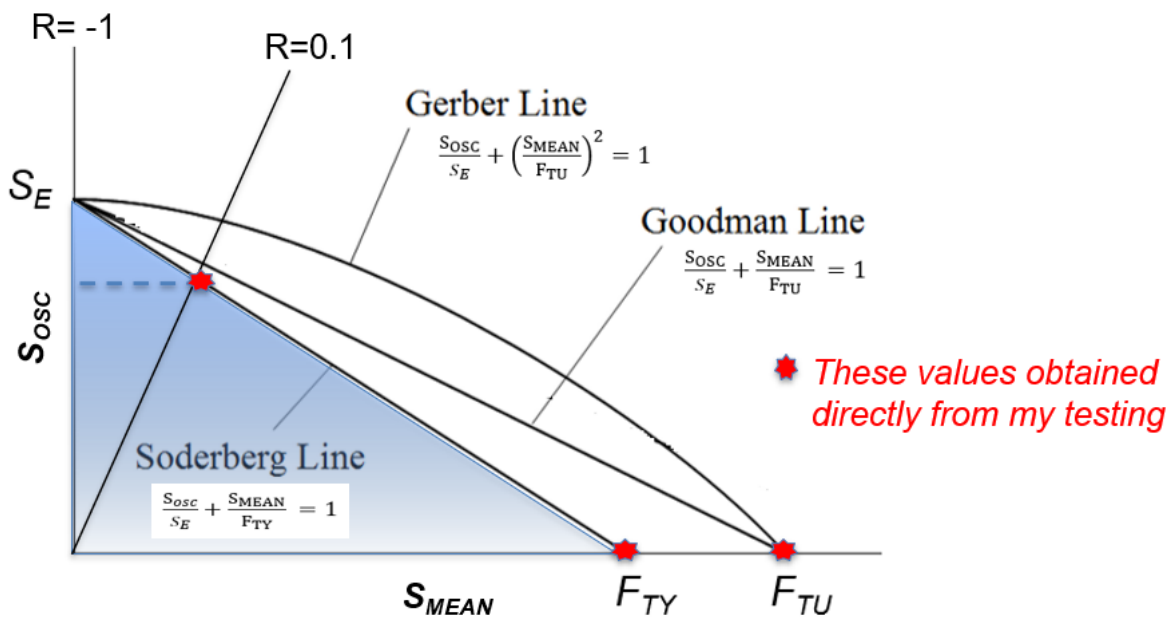


Figure 46. Soderberg plot showing values required from Static and Fatigue test results

The Soderberg diagram with the KDF resulting from RBIF is shown in Figure 47. Additional comparisons to the data in Reference [6] are presented in Figure 48, with the summary resulting KDFs presented in Table 13.

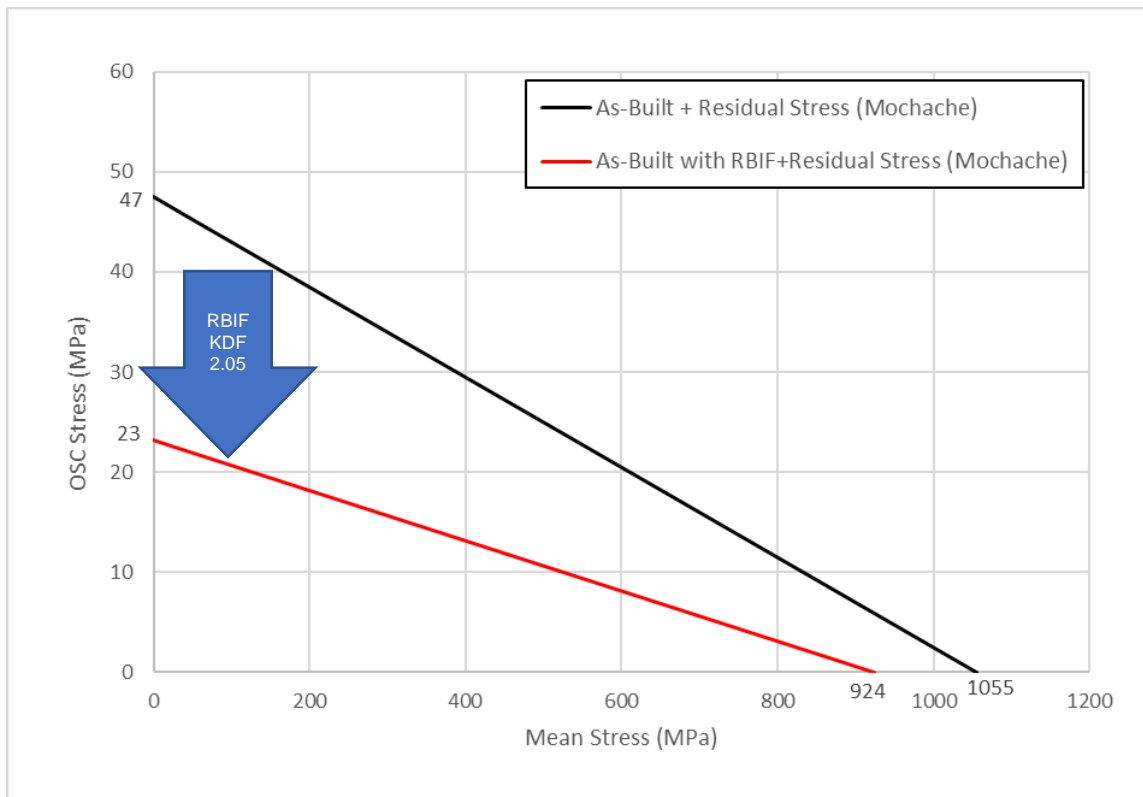


Figure 47. Soderberg plot showing Static and Fatigue test results of RBIF effect

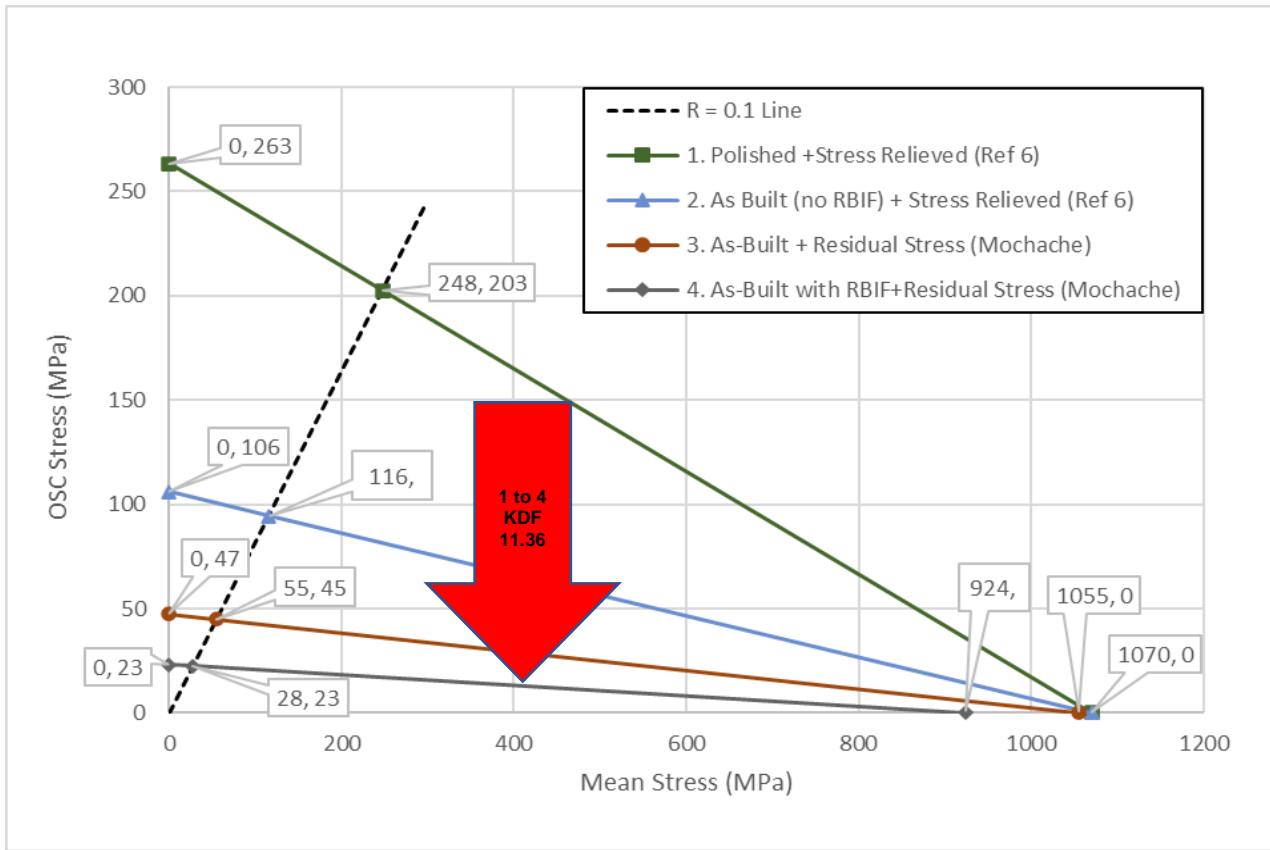


Figure 48. Soderberg of the Ti-6Al-4V by L-PBF with residual stress and RBIF

Table 13. Summary of KDF Calculations for Various Combination Effects for L-PBF Processed Ti-6Al-4V

Condition	Surface Treatment	Heat Treatment	Max Stress (Mpa)	Min Stress (Mpa)	Mean Stress (Mpa)	Osc Stress (Mpa)	R-Ratio	oeff Stress @ R=-1 Mpa	Reference
1	Polished	Stress Relieved	450	45	248	203	0.1	263	6
2	As-Built (no RBIF)	Stress Relieved	210	21	116	95	0.1	106	6, 147
3	As-Built (no RBIF)	Not Stress Relieved	100	10	55	45	0.1	47	Mochache
4	As-Built with RBIF	Not Stress Relieved	50	5	28	23	0.1	23	Mochache

KDF Summary

Comparison Condition	KDF	Remark
1-2	2.49	KDF for effect of surface finish: polish to as-built
2-3	2.23	KDF effect of as-built (no stress relief to stress relief)
1-3	5.55	KDF effect of surface finish and stress relief
3-4	2.05	KDF for effect of RBIF ONLY - The PRIMARY Result of this study!
1-4	11.36	KDF for effect of RBIF+Residual Stress per enhanced method (3.2).

5.3 Fractography

The fracture surfaces of the failed fatigue specimens were further analyzed to identify the following characteristics that are typical of fatigue failures [98]:

- Distinct Crack Initiation Site (CIS) or Sites
- Beach marks indicative of crack growth
- Distinct final fracture region

Fracture surfaces were also studied using high power microscopy to understand grain morphology, microstructure size and melt pool features. Three of the five baseline specimens were selected for the study: Specimen 2, 3 and 4. Initial high resolution digital photos of the fracture surfaces were taken using a digital DSLR camera with a 300 mm lens at about 10X magnification as shown in Figure 49. Using this magnification was sufficient for initial review of the fracture surfaces to identify the multiple CIS and distinct final fracture regions however, there were no clear beach marks indicative of the crack growth. These surfaces were further reviewed using high powered Scanning Electron Microscope (SEM).

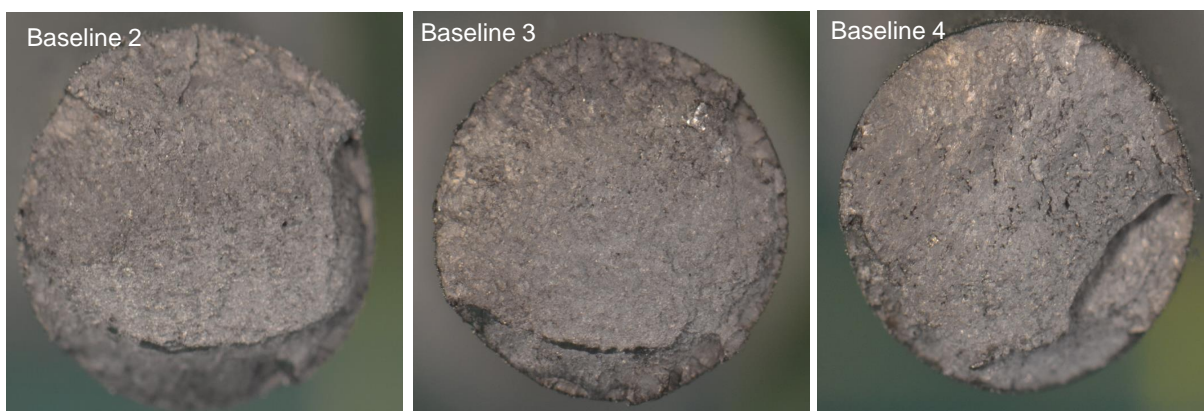


Figure 49. Fracture Surface Photographs baseline fatigue specimens analyzed for fracture surface

A closer look at baseline specimen 2, 3 and 4 revealed multiple CIS all originating at the surface and the distinct final fracture region giving general guidance on where initial crack paths coalesced and the general crack growth direction to final fracture as shown in Figure 50 , Figure 51 and Figure 52, respectively.

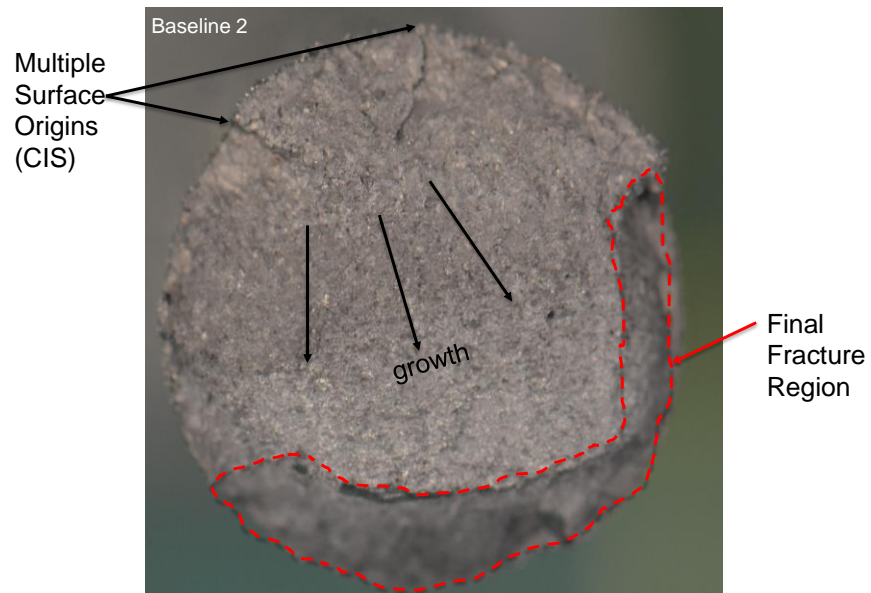


Figure 50. Fracture surface study of Baseline Specimen 2 ~10X Magnification

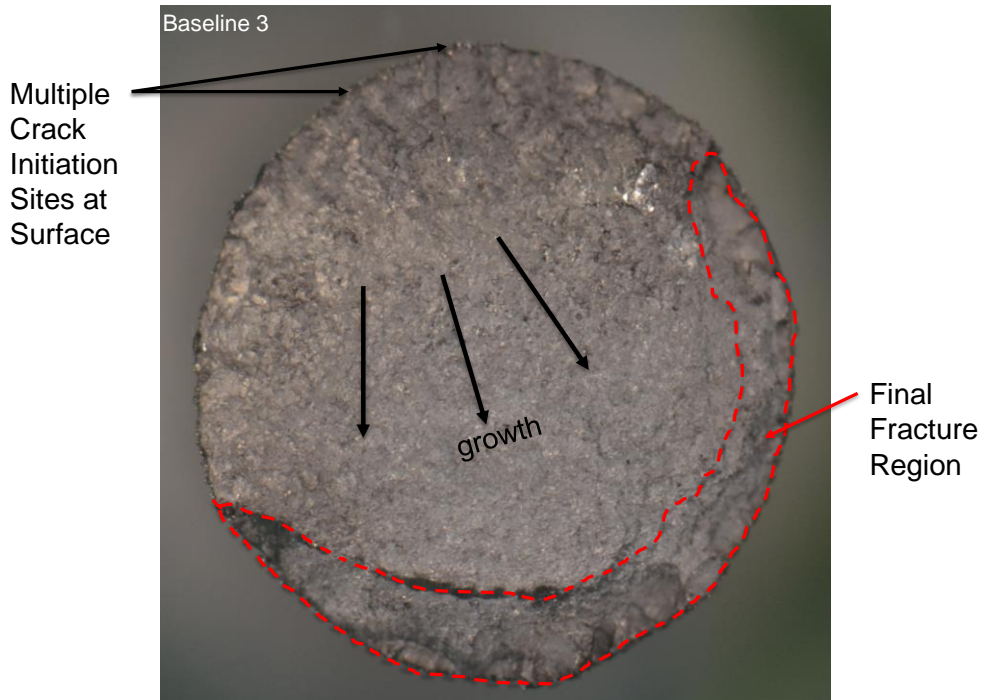


Figure 51. Fracture Surface Photograph of Baseline Specimen 3 ~10X Magnification

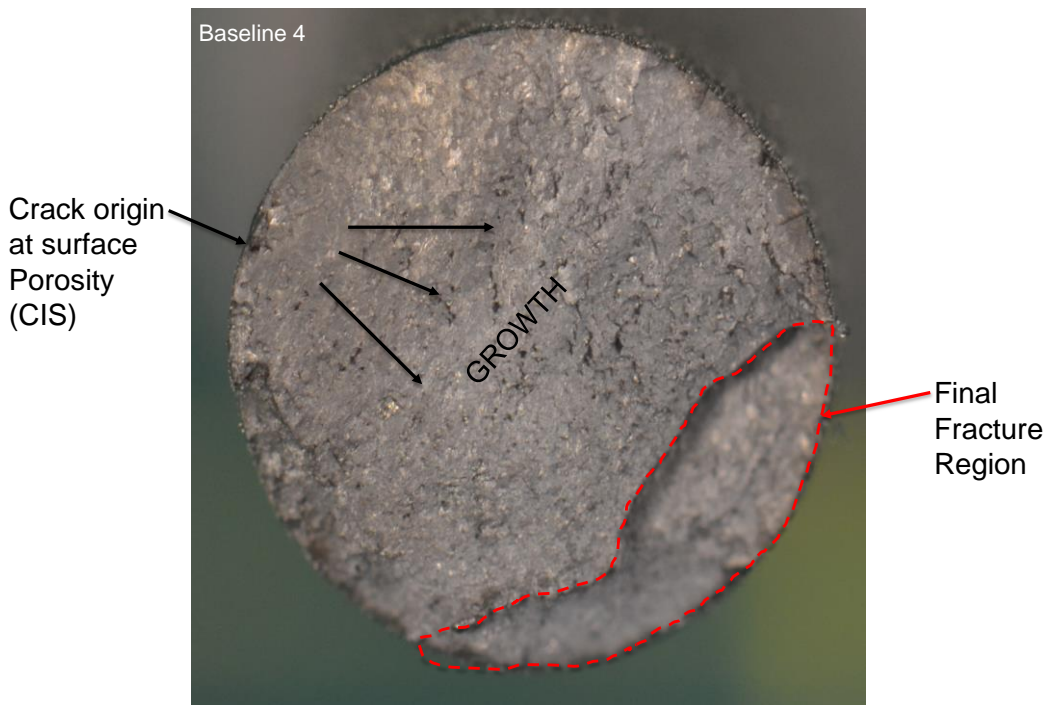


Figure 52. Fracture Surface Photograph of Baseline Specimen 4 ~10X Magnification

Additionally, all four of the five RBIF specimens which fractured during fatigue tests had their fracture surfaces analyzed. First, high resolution photographic images at 10X magnification were taken and are shown in Figure 53. From this, initial assessments of crack initiation sites, crack growth profiles and final fracture regions were made followed further by a study of the microstructures by SEM.

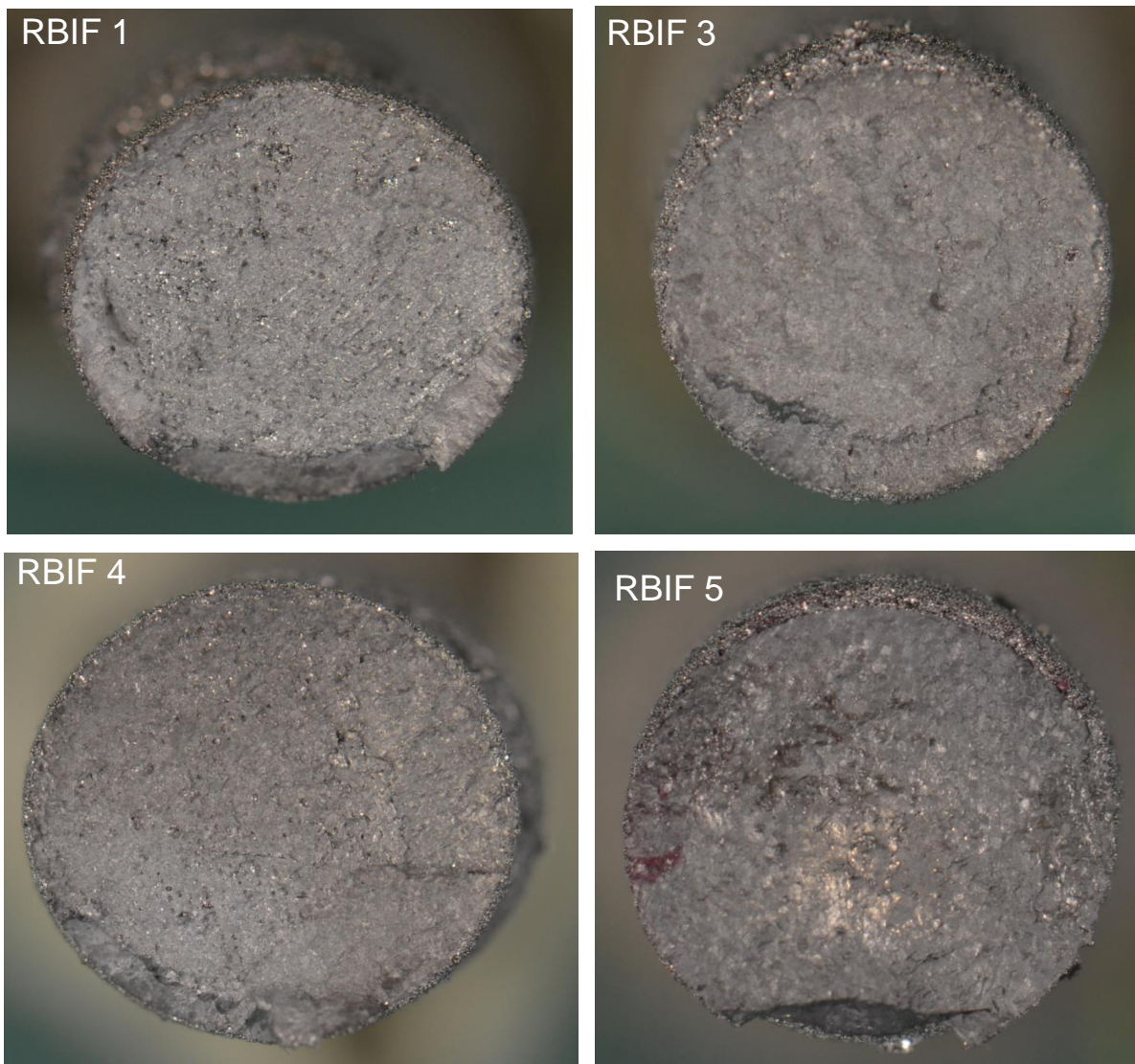


Figure 53. Fracture Surface Photographs of RBIF Specimens 1, 3, 4 and 5

Detailed reviews of the pictures of RBIF specimens 1, 3, 4 and 5 revealed that for the flawed specimens, the CIS was more concentrated around the areas of maximum depth of the RBIF profile as shown in Figure 54, Figure 55, Figure 56, and Figure 57 with the measurement between the dashed white lines representing the edge of the fracture surface and the border of the RBIF 'step'. From this maximum depth origins the cracks propagate diametrically out to the final fracture region. The final fracture region for the flawed specimens is on average, smaller in size compared to the baseline specimen final fracture regions. The detailed pictures with annotations are presented for the RBIF specimens 1, 3, 4 and 5 in Figure 54, Figure 55, Figure 56, and Figure 57 respectively.

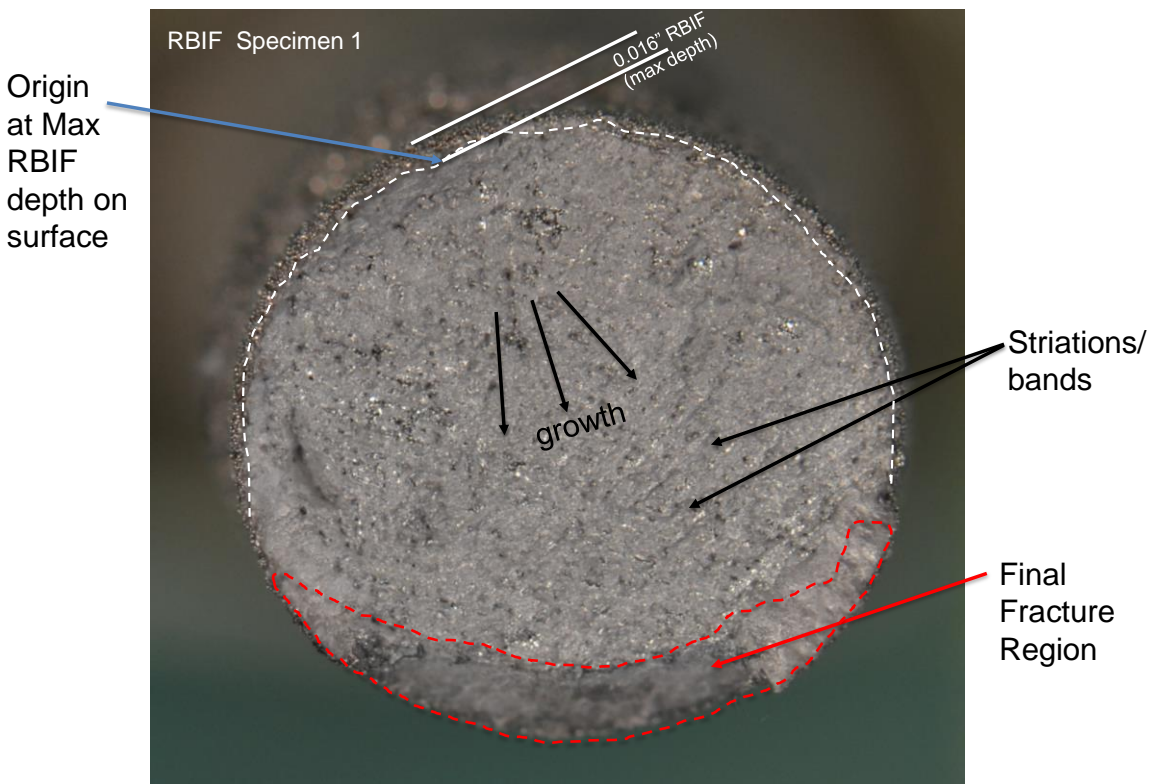


Figure 54. Fracture Surface Photograph of RBIF Specimens 1 ~10X Magnification

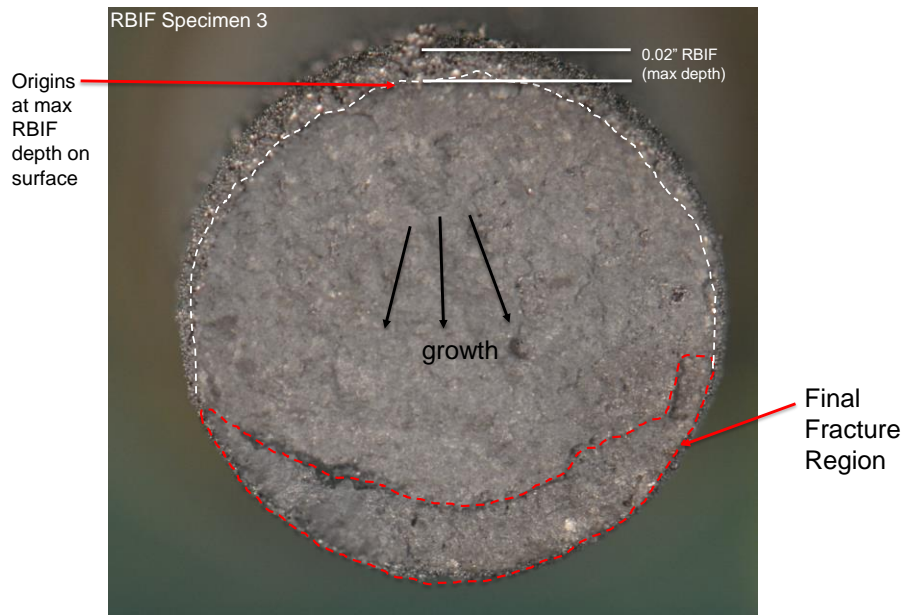


Figure 55. Fracture Surface Photograph of RBIF Specimens 3 ~10X Magnification

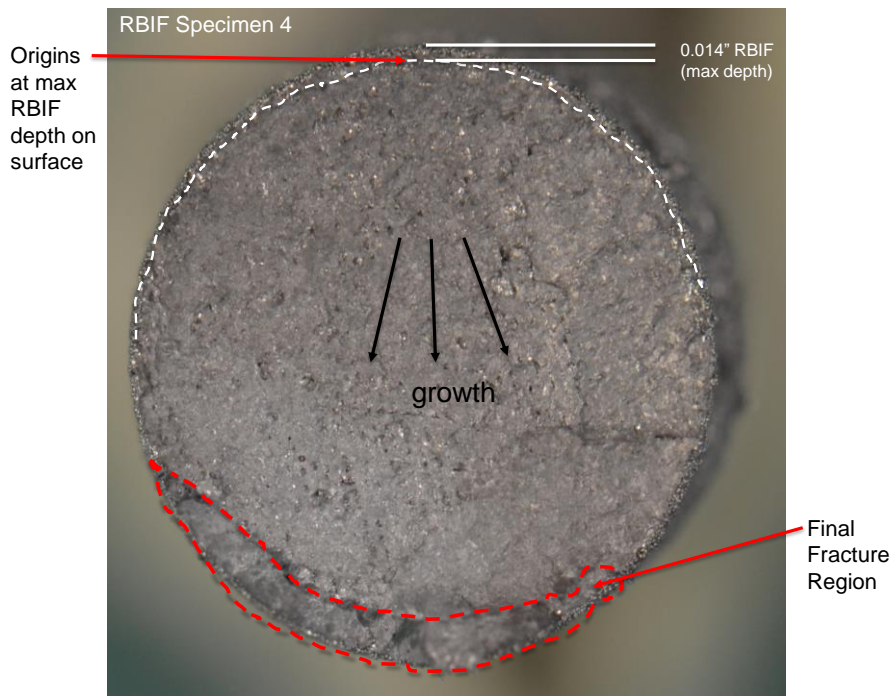


Figure 56. Fracture Surface Photograph of RBIF Specimens 4 ~10X Magnification

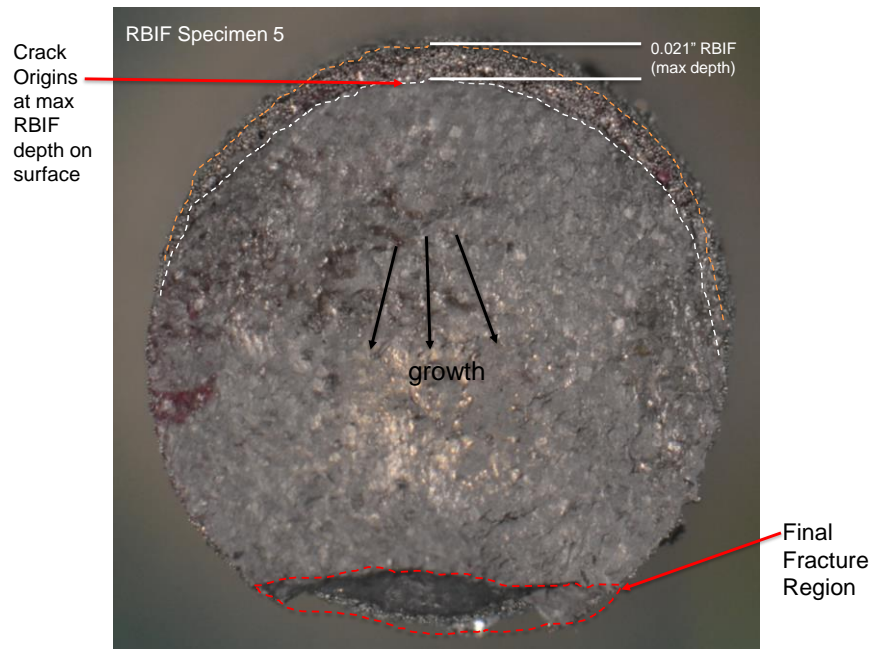


Figure 57. Fracture Surface Photograph of RBIF Specimens 5 ~10X Magnification

The microstructure of the specimens tested was also studied as this has been shown to have a significant effect on mechanical behavior [109, 127]. Using AADFV Inc's JEOL JSM-5410 SEM shown in Figure 58, the samples were scanned to identify microstructure grain type(s) and melt pool geometries as well as to determine defects such as inclusions, porosity, and LoF.



Figure 58. JEOL JSM-5410 SEM used for Microstructure studies

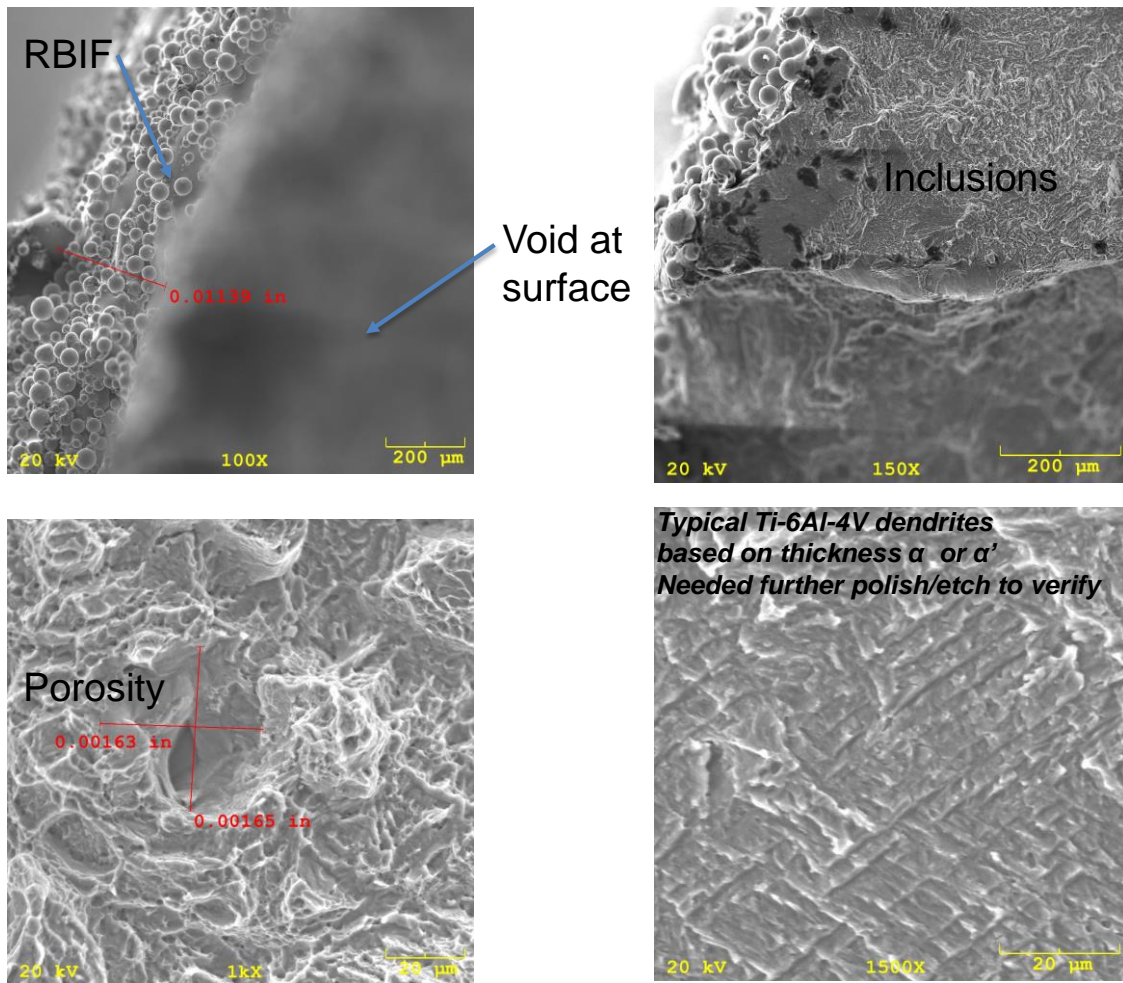


Figure 59. SEM photographs of fracture surface of RBIF Specimen 3

Analysis of the initial SEM results for specimen revealed clearly that the crack did originate close to see the maximum depth of the RBIF and a void close to this zone as shown in the top left of Figure 59. Indeed as another key observation made is that, while this specimen also shows other defects such as lack of fusion, inclusions and a lot of large internal porosities (see Figure 59), similar to the conclusions by others [113, 126], the surface defects are most critical for fatigue and indeed this RBIF and surface porosities is where the cracks initiated from.

Further studies of the microstructure were performed to identify the grain structure and melt-pool geometries of the build. From the lower right picture in Figure 59, the grain structures were observed as typical of titanium that has not been heat-treated. When heat treated at high temperature (above 882°C), titanium is allotropic with body centered cubic (BCC) crystal structure known as β phase. When cooled below 882°C it becomes hexagonal close packed (HCP) crystal structure known as the α phase. The α - β transformation temperature known as β -transus is sensitive to chemical composition, thus the alloying elements can be used to stabilize the α and/or β phase in the desired temperature range [134]. The composition of the titanium alloy used to make these specimens, EOS' Titanium Ti64 Grade 5, is shown in Table 14.

Table 14. EOS Titanium Ti64 Grade 5 Chemical Composition [135]

Powder chemical composition (wt.-%)			Powder particle size	
Element	Min.	Max.	Generic particle size distribution	20 – 80 μm
Ti	Balance			
Al	5.50	6.75		
V	3.50	4.50		
O	-	0.20		
N	-	0.05		
C	-	0.08		
H	-	0.015		
Fe	-	0.30		
Y	-	0.005		
Other elements, each	-	0.10		
Other elements, total	-	0.40		

During AM process by L-PBF, the Ti-64 powder is melted and solidifies first as β phase then transitions to $\alpha+\beta$ dual phase structure as it cools. Due to the high cooling rate in most L-PBF processes (unlike EB-PBF), martensitic transformation occurs which produces an α' phase [125]. It has been shown that improvements in fatigue properties are achieved with optimal build parameters and heat treatments that favor formation of elongation prior – β grains [136, 137]. Thus, these as-built specimens that were fatigue tested with evidence of having primarily a martensitic α' phase represent the less favorable fatigue strength characteristics and hence providing more conservative results/conclusions. The melt pool geometry was further studied by splitting the specimens in half using EDM and electro-polishing them followed by etching using Kroll's etchant. Figure 60 shows the results where the grain boundaries which appears to be “chequerboard-like” as in other studies of similar builds [147, 148] and melt pools that can be discerned quite well.

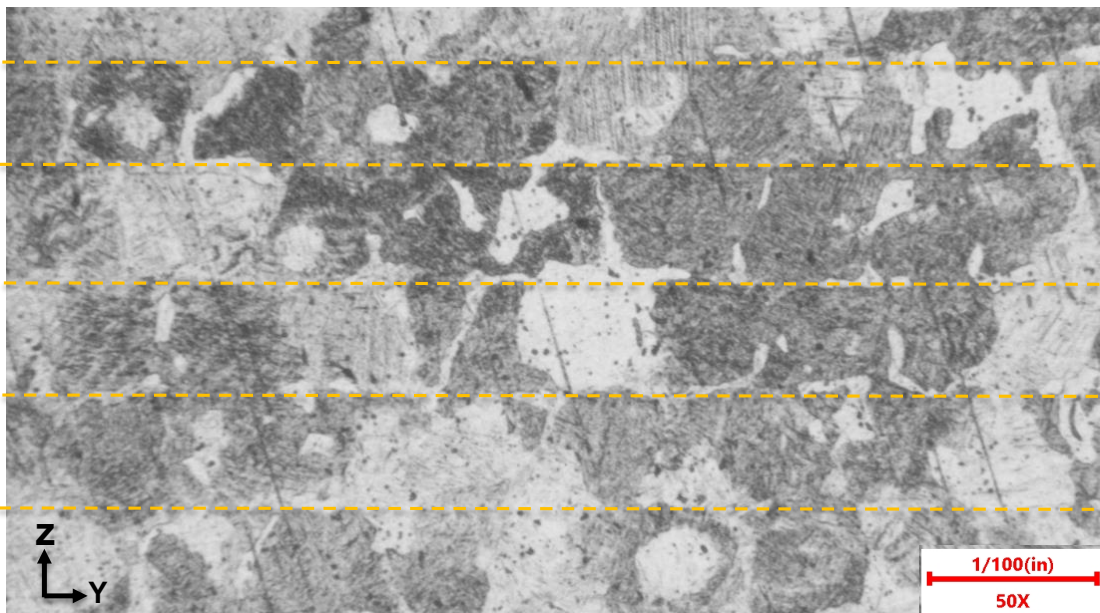


Figure 60. SEM cross-sectional view oriented in Y-Z plane showing grain boundaries

The grain structure is columnar in the Z-build direction and the needle-like structure exhibits primarily martensitic α' phase which is bound to give the lower fatigue properties as expected for this study that seeks the conservative lower-bound allowables since no post-process heat treatments were performed. Mechanical properties are very much dependent on the maximum heat treatment temperature. With rising maximum temperature, yield and ultimate strength decline and the fracture strain rises because of the transformation of the fine α' needles to a coarser mixture of α and β . Overall best results are obtained after 2 h at 850°C, followed by furnace cooling, or 1 h at 940°C, air cooling and tempering for 2 h at 650 °C followed by air cooling. The results for all properties are well above ASTM Standards for forged (ASTM F1472) and cast Ti6Al4V (ASTM F1108). The importance of the initial microstructure cannot be stressed enough. Due to the very fine martensite, the kinetics are completely different as compared to treatment of equiaxed or heavily deformed microstructures.

Consequently, application of standard heat treatments shows that these treatments do not lead to the usual or expected results. For L-PBF Ti-6Al-4V parts , heat treating at intermediate to high temperatures below the β -transus followed by furnace cooling proved to be optimal for an overall optimization of tensile properties [147]. This recommended heat treatment is what was used in the study by Wycisk et. al in the study used for comparison to this study's results.

6 Conclusion

This research successfully characterized the fatigue strength of additively manufactured (AM) Ti-6Al-4V, through fatigue and static tests conducted using specimens with and without recoater blade interference flaws (RBIF), and with and without residual stresses, supporting the enhanced fatigue substantiation methodology for AM parts using combined fatigue strength knock-down-factors (KDF), as also developed in this study.

From the test results using specimens built using an EOS M290 applying the L-PBF process with nominal build parameters as shown in Table 7 and using Ti-6Al-4V Grade 5 powder, we conclude and reject the null hypothesis, H_0 , which claimed that there is no significant reduction in fatigue strength resulting from recoater blade interference flaws, i.e. $KDF \sim 1.0$, and conclude H_a : *there is a significant reduction* in the fatigue strength resulting from recoater blade interference flaws, i.e. $KDF > 1.05$ at $\alpha = 0.05$. The KDF due to recoater blade interference flaws in Ti-6Al-4V, up to 0.020 inches in deep offset, is **2.05**. This KDF is recommended for use with the enhanced fatigue substantiation methodology presented in this study, Section 3.2, and per the additional recommendations below. Additional resulting KDF combinations are presented in Table 13.

6.1 Recommendations

When applying the results of this study to aerospace critical structural components (PSEs etc.), ensure the part was made using optimal EOS M290 L-PBF process parameters, and using virgin Ti-6Al-4V Grade 5 powder, and following the design, materials and process standards established for Ti-6Al-4V L-PBF per [17, 43, 65, 67, 68, 74, 82, 83]. It further recommended that the use of the enhanced fatigue safe-life analysis methodology proposed in Section 3.2, which provides

increased reliability in the applicable loads used in the analysis while simultaneously combining additional reductions to material strength based on the KDFs for surface flaw reductions combined with residual stress (heat treatment) reduction as characterized for Ti-6Al-4V, applies the proposed L-PBF AM process factor (F_{AM}) validated using full-scale fatigue test results for the particular application, while continuing to maintain the following good practices, for the highest AM structural strength reliability in critical structure applications:

- All fatigue critical surfaces on the parts must receive surface finish improvements to achieve at least 63 RMS or better,
- Critical parts must have Hot-Isostatic-Pressure post processing for decreased porosity,
- Residual stress relief heat treatment must elevate temperatures above the β transus temperature for Ti-6Al-4V (882°C) for ideal microstructure development,
- Avoid RBIF and other such flaws by following the build guidelines in Section 33,
- All locations of the parts must be fully inspected using detailed visual, XRD, Eddy Current, Magnetic Particle or Fluorescent Penetrant Inspection and other methods with the appropriate PoD for each considered [74-77].

With the forgoing recommendations applied, a fatigue retirement time may be reliably substantiated for a Ti-6Al-4V L-PBF part, based on the Safe-Life with CDF Method 3 of Table 4, with the enhancement presented in Equation 10, where allowable fatigue stresses considering application of KDFs for RBIF and Residual Stress as summarized in Table 13, with calculation of fatigue damage based on any exceeding stresses using Miner's rule and the Soderberg for condition 4 of Figure 48, is expected to result in adequate structural reliability.

6.2 Future work

For future work, it is proposed to continue the development of full-scale fatigue tests with aerospace critical structural part applications using Ti-6Al-4V and the L-PBF build process, per the recommendations shared in Section 6.1, to validate the theoretical reliability of the fatigue retirement life results calculated using the Ti-6Al-4V material strength characterized with both RBIF and residual strength KDFs and the enhanced safe life approach presented in Section 3.2. Additional studies in characterization of other defects as well as a review of the damage tolerance strength of Ti-6Al-4V with the RBIF and residual stress using the C(T) specimens can be used to further this work and increase the value of this research.

LIST OF REFERENCES

1. Mochache, J., and Taylor, R., A Review of Fatigue and Damage Tolerance Life Prediction Methodologies toward Certification of Additively Manufactured Metallic Principal Structural Elements. AIAA SciTech 2021 Forum. <https://doi.org/10.2514/6.2021-1509>
2. Gibson I., Rosen D., Stucker B., Additive Manufacturing Technologies, 3D Printing, Rapid Prototyping, and Direct Digital Manufacturing, 2nd Edition, New York, 2015.
3. Yang L., Hsu K., Baughman B., Godfrey D., Medina F., Menon M., Wiener S., Additive Manufacturing of Metals: The Technology, Materials, Design and Production, Springer Series in Advanced Manufacturing, 2017
4. Gu D., Laser Additive Manufacturing of High-Performance Materials, Springer 2015
5. <https://www.ge.com/additive/>
6. Wycisk E., Solbach A., Siddique, S., Herzog D., Walther F., and Emmelmann, C., Effects of Defects in Laser Additive Manufactured Ti-6Al-4V on Fatigue Properties 8th International Conference on Photonic Technologies LANE 2014
7. America Makes and ANSI Additive Manufacturing Standardization Collaborative (AMSC), Standardization Roadmap for Additive Manufacturing, Ver. 2.0, June 2018
8. Ristori V., Sara Della Ratta, and François D., Fatigue in Additive Manufactured Aircraft: The Long Way to Make It Fly., In ICAF 2019–Structural Integrity in the Age of Additive Manufacturing: Proceedings of the 30th Symposium of the International Committee on Aeronautical Fatigue, June 2-7, 2019, Krakow, Poland, p. 16. Springer, 2019.
9. Seifi, M., Gorelik, M., Waller, J., Hrabec, N., Shamsaei, N., Daniewicz, S., and Lewandowski, J., Progress Towards Metal Additive Manufacturing Standardization to Support Qualification and Certification, JOM. 69 (2017) 439–455
10. Gorelik, M., Additive manufacturing in the context of structural integrity, International Journal of Fatigue, Vol. 94 (2017), pp. 168–177.
11. United States Code of Federal Regulations, 14 CFR § Part 25 Airworthiness standards: Transport Category Airplanes, US Government Publishing Office
12. United States Code of Federal Regulations, 14 CFR § Part 29 Airworthiness standards: Transport Category Rotorcraft, US Government Publishing Office
13. United States Code of Federal Regulations, 14 CFR § Part 33 Airworthiness standards: Transport Category Aircraft Engines, US Government Publishing Office
14. 3D Printing Industry, The Authority on Additive Manufacturing, <https://3dprintingindustry.com/news/airbus-a350-xwb-takes-off-with-over-1000-3d-printed-parts-48412/>
15. Mardaras, J., Emile, P., Santgerma, A., Airbus approach for F&DT stress justification of Additive Manufacturing parts, Procedia Structural Integrity, Volume 7, 2017, Pages 109-115 and presented at the 3rd International Symposium on Fatigue Design and Material Defects, FDMD 2017, 19-22 September 2017, Lecco, Italy
16. FAA Advisory Circular AC25.571-1D, Damage Tolerance and Fatigue Evaluation of Structure, US Government Publishing Office
17. NASA Marshall Space Flight Center (MSFC), MSFC-STD-3716, Standard for additively manufactured spaceflight hardware by laser powder bed fusion in metals, Alabama, October 2017.
18. JSSG-2006, Department of Defense Joint Services Specification Guide, Aircraft Structures, 1998.
19. MIL-STD-1530C, Department of Defense Standard Practice, Aircraft Structural Integrity Program (ASIP), 2005.
20. FAA Advisory Circular 29-2C, Certification of Transport Category Rotorcraft, July 2014
21. Duprat, D., Practical Fatigue and Damage Tolerance for Aircraft, Feb 2019
22. FAA Advisory Circular AC27-1B MG11, Certification of Normal Category Rotorcraft: Miscellaneous Guidance 11, US Government Publishing Office
23. Krasnowski, B. R., (1991). Reliability requirements for Rotorcraft dynamic components. Journal of the American Helicopter Society, 36(3), 13-22

24. Tucker, B., Mochache, J., Hobbs, R., Yu, R., and Baker, T., Development of a Fatigue Life Management System for Dynamic Components on the OH-58D Kiowa, AHS Forum 62, May 2012.
25. Herman, M., & Besson, J. M. (2016). Application of flaw tolerance methodologies on rotorcraft metallic Principal Structural Elements`
26. Taylor, R. M., Manzo, J., and Flansburg, L., Certification strategy for additively manufactured structural fittings, In Proceedings of the 27th Annual International Solid Freeform Fabrication Symposium, Austin, TX, 2016, pp. 1985-2000.
27. SAE International, Additive Manufacturing Standards Development Brochure 2018, Abbott, D., SAE AMS-AM Chair and Principal Engineer, GE Additive.
28. Shamsaei, N., Yadollahi, A., Bian, L., and Thompson, S. M., An overview of Direct Laser Deposition for additive manufacturing; Part II: Mechanical behavior, process parameter optimization and control. Additive Manufacturing, 8, 12-35, 2015.
29. Chahal, V., and Taylor, R. M., A review of geometric sensitivities in laser metal 3D printing, Virtual and Physical Prototyping, 15(2), 227-241, 2020.
30. Kruth, J. P., Deckers, J., Yasa, E., & Wauthlé, R., Assessing and comparing influencing factors of residual stresses in selective laser melting using a novel analysis method, Proceedings of the institution of mechanical engineers, Part B: Journal of Engineering Manufacture, 226(6), 980-991, 2012.
31. Hodge, N. E., Ferencz, R. M., & Solberg, J. M., Implementation of a thermomechanical model for the simulation of selective laser melting, Computational Mechanics, 54(1), 33-51, 2014.
32. Afazov, S., Denmark, W. A., Toralles, B. L., Holloway, A., & Yaghi, A., Distortion prediction and compensation in selective laser melting, Additive Manufacturing, 17, 15-22, 2017.
33. Yaghi, A., Ayvar-Soberanis, S., Moturu, S., Bilkhu, R., & Afazov, S., Design against distortion for additive manufacturing. Additive Manufacturing, 27, 224-235, 2019.
34. Yadollahi, A., Shamsaei, N., Thompson, S. M., Elwany, A., & Bian, L., Effects of building orientation and heat treatment on fatigue behavior of selective laser melted 17-4 PH stainless steel, International Journal of Fatigue, 94, 218-235, 2017.
35. Yadollahi, A., Shamsaei, N., Thompson, S. M., & Seely, D. W. (2015). Effects of process time interval and heat treatment on the mechanical and microstructural properties of direct laser deposited 316L stainless steel. Materials Science and Engineering: A, 644, 171-183.
36. Bobbio, L.D., Qin, S., Dunbar, A., Michaleris, P. and Beese, A.M., 2017. Characterization of the strength of support structures used in powder bed fusion additive manufacturing of Ti-6Al-4V. Additive Manufacturing, 14, pp.60-68.
37. Carrion, P. E., & Shamsaei, N. (2016). Strain-based fatigue data for Ti-6Al-4V ELI under fully-reversed and mean strain loads. Data in brief, 7, 12-15.
38. Diegel, O., Nordin, A., & Motte, D. (2019). A Practical Guide to Design for Additive Manufacturing. Springer Singapore.
39. Mancisidor, A. M., Garcíandia, F., San Sebastian, M., Álvarez, P., Díaz, J., & Unanue, I. (2016). Reduction of the residual porosity in parts manufactured by selective laser melting using skywriting and high focus offset strategies. Physics Procedia, 83, 864-873.
40. Gockel, J., Beuth, J., & Taminger, K. (2014). Integrated control of solidification microstructure and melt pool dimensions in electron beam wire feed additive manufacturing of Ti-6Al-4V. Additive Manufacturing, 1, 119-126.
41. Morgan, K., & Wells, D. (2016). Overview of fatigue and damage tolerance performance of SLM alloy 718.
42. Gorelik, M., Federal Aviation Administration Additive Manufacturing – A Regulatory Perspective, USNCTAM Meeting April 22, 2016, National Academics Washington, DC
43. NASA Marshall Space Flight Center (MSFC), MSFC-STD-3717 “Standard practices for the Laser Powder Bed Fusion (L-PBF) process”, Alabama, October 2017.
44. U.S. Department of Transportation, Federal Aviation Administration, Advisory Circular AC20-107B, “Composite Aircraft Structure”
45. Khaled, T., Chief Scientist Advisor, Metallurgy FAA, Additive Manufacturing (AM) Rev. A., Presentation at FAA and Air Force Research Laboratory joint workshop on Qualification and Certification of Additively Manufactured Parts, held September 1–3, 2015 in Dayton, Ohio
46. NASA-STD-5019A, Fracture control requirements for spaceflight hardware, March 2018, Ralph R. Roe Jr., NASA Chief Engineer

47. ARP4761, Guidelines and Methods for Conducting the Safety Assessment Process on Civil Airborne Systems and Equipment, SAE International, 12-1-1996.
48. ARP4754A, Guidelines for Development of Civil Aircraft and Systems, SAE International
49. RTCA DO-254 Design Assurance Guidance for Airborne Electronic Hardware, April 2000
50. RTCA DO-178C Software Considerations in Airborne Systems and Equipment Certification, July 2013
51. Cincinnati Incorporated, CI and ORNL Advancing Large-Part Additive Manufacturing, March 2014 Press Release <https://www.e-ci.com/baam>
52. European Aviation Safety Agency (EASA), “Easy Access Rules for Large Rotorcraft (CS-29) (Amendment 1)”, June 2018
53. Yadollahi, A., Mahtabi, M., Doude, H., Newman Jr., J., Prediction of Fatigue Lives in Additively Manufactured Alloys based on the Crack-Growth Concept, Proceedings of the 28th Annual International Solid Freeform Fabrication Symposium, 2017.
54. Romano, S., Bruckner-Foit, A., Brandao, A., Gumpinger, J., Ghidini, T., Beretta, S., Fatigue properties of AlSi10Mg obtained by additive manufacturing: Defect-based modelling and prediction of fatigue strength, Engineering Fracture Mechanics, Volume 187, January 2018, pages 165-189
55. Liu, Y., and Mahadevan, S. (2009). Probabilistic fatigue life prediction using an equivalent initial flaw size distribution. International Journal of Fatigue, 31(3), 476-487
56. Fawaz, S. A. (2000). Equivalent initial flaw size testing and analysis. Air Force Research Lab Wright-Patterson AFB OH Air Vehicles Directorate
57. Muhammad M., Carrion, P., Shamsaei, N., Fatigue Life Prediction of Additive Manufactured Materials Using a Defect Sensitive Model, Solid Freeform Fabrication Symposium 2019, Austin TX.
58. Murakami, Y., and Endo, M., Effects of defects, Inclusions and Inhomogeneities on Fatigue Strength, International Journal of Fatigue, 1994.
59. Murakami, Y., Metal fatigue: Effects of Small Defects and Nonmetallic Inclusions, Oxford, Elsevier, 2002.
60. Yadollahi, A., Shamsaei, N., Additive Manufacturing of Fatigue Resistant Materials: Challenges and Opportunities, Int. J. Fatigue. 98 (2017) 14–31.
61. Romano, S., Bruckner-Foit, A., Brandao, A., Gumpinger, J., Ghidini, T., Beretta, S., “Fatigue properties of AlSi10Mg obtained by additive manufacturing: Defect-based modelling and prediction of fatigue strength,” Engineering Fracture Mechanics, Volume 187, January 2018, pages 165-189
62. Ivan Meneghin, I., Ivetic, G., Stiller, M., Molinari, G., Ristori, V., Ratta, S. D., & Dumont, F., “Fatigue in additive manufactured aircraft: The long way to make it fly.” ICAF-2019 Structural Integrity in the Age of Additive Manufacturing; Niepokolczycki, A., Komorowski, J., Eds, 16-30.
63. Kim, J. H., Chau-Dinh, T., Zi, G., Lee, W. W., & Kong, J. S. (2016). Probabilistic fatigue integrity assessment in multiple crack growth analysis associated with equivalent initial flaw and material variability. Engineering Fracture Mechanics, 156, 182-196.
64. Ocampo, J. D., Crosby, N., & Millwater, H. R. (2017). Probabilistic damage tolerance for aviation fleets using a kriging surrogate model. In 19th AIAA Non-Deterministic Approaches Conference (p. 1567).
65. SAE-AMS AMS7000: Laser-Powder Bed Fusion (L-PBF) Produced Parts, Nickel Alloy, Corrosion and Heat-Resistant, 62Ni-21.5Cr-9.0Mo-3.65Nb Stress Relieved, Hot Isostatic Pressed and Solution Annealed
66. SAE-AMS AMS7001: Nickel Alloy, Corrosion and Heat-Resistant, Powder and Additive Manufacturing, 62Ni-21.5Cr-9.0Mo-3.65Nb
67. SAE-AMS AMS7002: Process requirements for production of metal powder feedstock for use in additive manufacturing of aerospace parts.
68. SAE-AMS “AMS7003: Laser Powder Bed Fusion Process”
69. D. Huston. “Structural sensing, health monitoring, and performance evaluation.” CRC Press, 2010.
70. W.N. MacPherson, D.P. Hand, D. Havermann, J. Matthew and R.R.J. Maier. Measuring residual stresses in metallic components manufactured with Fiber bragg gratings embedded by selective laser melting, International Conference on Optical Fiber Sensors (OFS24), pages 96340T-96340T. International Society for Optics and Photonics, 2015.
71. X. Cheng and X. Li. Micro thin sensor embedded in metal structures for in-situ process monitoring during ultrasonic welding. ASME 2005 International Mechanical Engineering Congress and Exposition, pages 1117-1121
72. H. Choi, W. Cai, J.A. Abell, J. Zhao, H. Li and X. Li. Insertable thin thermo-couples for in-situ transient temperature monitoring in ultrasonic metal welding of battery tabs. Journal of Manufacturing Processes, 15(1):136-140, 2013.

73. A.J. Hehr, P.J. Wolcott, and M.J. Dapino. Optimized Welding Parameters of Al 6061 Ultrasonic Additive Manufactured Structures. *Journal of Materials Research*, 29(18), 2014.
74. NASA-STD-5009, Non-Destructive Evaluation Requirements for Fracture-Critical Metallic Components, April 2008
75. EN-SB-08-012 Rev B, NDI Capability Guidelines for USAF Aircraft Structures, July 2011
76. DOT/FAA/AR-96/94, Visual Inspection Research Project Report on Benchmark Inspection, by F. W. Spencer, Oct. 1996
77. Rummel, W., and Matzkanin, G., Nondestructive Evaluation (NDE) Capabilities Data Book, 3rd Edition, Nov. 1997
78. Hussein, A., Hao, L., Yan, C., Everson, R., & Young, P. (2013). Advanced lattice support structures for metal additive manufacturing. *Journal of Materials Processing Technology*, 213(7), 1019-1026
79. ISO/ASTM Standard 52907:2019, Additive Manufacturing – Feedstock Materials – Methods to Characterize Metal Powders, ISO/TC 261, Nov 2019
80. ASTM WK55610, New Test Methods for the Characterization of Powder Flow Properties for Additive Manufacturing Applications, ASTM International, Conshohocken, PA – Draft, 2020
81. ASTM WK55297, New Guide for Additive Manufacturing – General Principles – Standard Test Artefacts for Additive Manufacturing, ASTM International, Conshohocken, PA – Draft, 2020
82. AWS D20.1/D20.1M:2019, Specification for Fabrication of Metal Components Using Additive Manufacturing, American Welding Society, Feb. 2019.
83. ISO/ASTM 52910-18, Additive manufacturing – Design – Requirements, guidelines and recommendations, ASTM International, Conshohocken, PA, 2018
84. ISO8887-1: 2017, Design for Manufacturing, Assembling, Disassembling and End-Of-Life Processing, ISO/TC 10, Sept. 2017
85. ISO/ASTM CD 52916, Additive manufacturing – Data formats – Standard specification for optimized medical image data, ISO/ASTM – Draft 2020.
86. ASME Y14.46, “Product Definition for Additive Manufacturing, The American Society of Mechanical Engineers, 2017
87. ISO/ASTM 52600, Additive manufacturing – General principles – Terminology,
88. ASTM WK 54856, New Guide for Principles of Design Rules in Additive Manufacturing, American Society for Testing and Materials, Draft 2020.
89. Waller, J., Saulsberry, R., Parker, B., Hodges, K., Burke, E., and Taminger, K., “Summary of NDE of Additive Manufacturing Efforts in NASA,” AIP Conference Proceedings, Vol. 1650, No. 1, American Institute of Physics, 2015
90. Zerbst, U., Hilgenberg, K., Damage development and damage tolerance of structures manufactured by selective laser melting – a review, 3rd International Symposium of Fatigue Design and Material Defects, FDMD 2017, 19-22 September 2017, Lecco, Italy
91. Cross, R. J., Makeev, A., and Armanios, E. (2006). A comparison of predictions from probabilistic crack growth models inferred from Virkler's data. *Journal of ASTM International*, 3(10), 1-11.
92. Virkler, D. A., Hillberry, B. M., and Goel, P. K., The Statistical Nature of Fatigue Crack Propagation, *J. Eng. Mater. Technol.*, Vol. 101, No. 2, 1979, pp. 148–153.
93. Maymon, G., The Problematic Nature of the Application of Stochastic Crack Growth Models in Engineering Design, *Eng. Fract. Mech.*, Vol. 53, No. 6, 1996, pp. 911–916.
94. d'Ippolito, R., Hack, M., Donders, S., Van der Auweraer, H., Tzannetakis, N., Farkas, L., and Desmet, W. (2007). Robust and reliable fatigue design of automotive and aerospace structures. In *Proceedings of 6th International Conference on Durability and Fatigue (Fatigue 2007)*, Cambridge, UK.
95. Li, P., Warner, D. H., Fatemi, A., & Phan, N. (2016). Critical assessment of the fatigue performance of additively manufactured Ti–6Al–4V and perspective for future research. *International Journal of Fatigue*, 85, 130-143.
96. White, P., Molent, L., and Barter, S., Interpreting Fatigue Test Results Using a Probabilistic Fracture Approach, *Int. J. Fatigue*, Vol. 27, No. 7, 2005, pp. 752–767.
97. Fawaz, S., Equivalent Initial Flaw Size Testing and Analysis, Technical Report AFRL-VA-WP-TR- 2000-3024, 2000.
98. Leverant, G., Millwater, H., McClung, R., and Enright, M., A New Tool for Design and Certification of Aircraft Turbine Rotors, *Journal of Eng. Gas Turbines Power*, 126(1), 155-159.
99. Stephens, R., Fatemi, A., and Fuchs, H., *Metal Fatigue in Engineering*. 2000

100. Metallic Material Properties Development and Standardization (MMPDS), Battelle Memorial Institute for the Federal Aviation Administration, William J. Hughes Technical Center, Battelle, Columbus, OH.
101. Composite Materials Handbook, CMH-17-3G, Vol. 3, Chapter 4.
102. ASTM E-399, Standard Test Method for Linear-Elastic Plane-Strain Fracture Toughness K_{Ic} of Metallic Materials, ASTM International, Conshohocken, PA, 2009.
103. ASTM E-466, Standard Practice for Conducting Force Controlled Constant Amplitude Axial Fatigue Tests for Metallic Materials, ASTM International, Conshohocken, PA, 2007.
104. ASTM E-647, Standard Test Method for Measurement of Fatigue Crack Growth Rates, ASTM International, Conshohocken, PA, 2000.
105. AMS4928, Titanium Alloy Bars, Wire, Forgings, Rings and Drawn Shapes 6Al-4V Annealed, SAE Aerospace Material Specification
106. Ning J, Wang W, Zamorano B, and Liang S., Analytical modeling of lack-of-fusion porosity in metal additive manufacturing. *Applied Physics* Nov. 2019
107. Mukherjee T, DebRoy T. Mitigation of lack of fusion defects in powder bed fusion additive manufacturing. *Journal of Manufacturing Process* 2018;36:442–9.
108. Coeck S, Bisht M, Plas J, Verbist F. Prediction of lack of fusion porosity in selective laser melting based on melt pool monitoring data. *Additive Manufacturing* 2019;25:347–56.
109. Kok Y, Tan X, Wang P, Nai M, Loh N, Liu E, et al. Anisotropy and heterogeneity of microstructure and mechanical properties in metal additive manufacturing: a critical review. *Material Design* 2018;139:565–86.
110. Lewandowski JJ, Seifi M. Metal additive manufacturing: a review of mechanical properties. *Annu Rev Mater Res* 2016;46(1):151–86.
111. Mukherjee T., Zhang W., DebRoy T. An improved prediction of residual stresses and distortion in additive manufacturing. *Computer Material Science* 2017;126:360–72.
112. Megahed M., Mindt H-W, N'Dri N, Duan H., Desmaison O. Metal additive-manufacturing process and residual stress modeling. *Integr Mater Manuf Innov* 2016;5(1):61–93.
113. Pegues J., Roach M., Williamson R., S, Shamsaei N., Surface roughness effects on the fatigue strength of additively manufactured Ti-6Al-4V. *International Journal of Fatigue* 2018;116:543–52.
114. ASTM E206, Standard Definitions of Terms Relating to Fatigue Testing and Statistical Analysis of Data, ASTM International, Conshohocken, PA, 2009.
115. Forman, R., Study of Fatigue Crack Initiation from Flaws Using Fracture Mechanics Theory,
116. Fatemi, A., and Yang, L., Cumulative Fatigue Damage and Life Prediction Theories; A Survey of the State of The Art for Homogenous Materials, *International Journal of Fatigue* Vol. 20, pg. 9-34, 1998
117. Miner, A., Cumulative Damage in Fatigue, *Journal of Applied Mechanics*, Vol. 67, pg.339 Sept 1945
118. Kauzlarich, J., The Palmgren-Miner Rule Derived, *Tribological Design of Machine Elements*, Vol 14, Pg 175-179
119. Mrozinski, S., Energy-Based Method of Fatigue Damage Cumulation, *International Journal of Fatigue*, Vol. 121, April 2019
120. Zion, L., Some Simple Approaches to Reliable Fatigue Damage Prediction, *Journal of American Helicopter Society*, Jan 1997
121. Hibbler, R., *Engineering Mechanics, Statics*, 10th Edition, Prentice Hall, January 2004
122. Palmgren, A., Durability of Ball Bearings, *ZDVEDI*, Vol. 68, No. 14, p. 339
123. Materialise, Metal 3D Printing: How to counter the Impact of Recoaters, https://www.materialise.com/system/files/resources/Paper_Metal_3DPrinting_Recoaters.pdf
124. Chastand, V., Quaegebeur, P., Maia, W., Charkaluk, E., Comparative Study of Fatigue Properties of Ti-6Al-4V specimens built by electron beam melting (EBM) and selective laser melting (SLM), *Material Characterization*, Elsevier, March 2018
125. Huber F, Rasch M, Schmidt M. Laser Powder Bed Fusion (PBF-LB/M) Process Strategies for In-Situ Alloy Formation with High-Melting Elements. *Metals*. 2021
126. Pegues, J. W., Shao, S., Shamsaei, N., Sanaei, N., Fatemi, A., Warner, D. H., ... & Phan, N. (2020). Fatigue of additive manufactured Ti-6Al-4V, Part I: The effects of powder feedstock, manufacturing, and post-process conditions on the resulting microstructure and defects. *International Journal of Fatigue*, 132, 105358.
127. Molaei, R., Fatemi, A., Sanaei, N., Pegues, J., Shamsaei, N., Shao, S., ... & Phan, N. (2020). Fatigue of additive manufactured Ti-6Al-4V, Part II: The relationship between microstructure, material cyclic properties, and component performance. *International Journal of Fatigue*, 132, 105363.

128. Hooper, P.A. Melt pool temperature and cooling rates in laser powder bed fusion. *Addit. Manuf.* 2018, 22, 548–559.
129. Cao S., Zou Y., Voon C., Lim S., and Wu X., Review of laser powder bed fusion (L-PBF) fabricated Ti-6Al-4V: process, post-process treatment, microstructure, and property[J]. *Light: Advanced Manufacturing*, 2021, 2(3): 313-332.
130. Khorasani, A., Gibson, I., Veetil, J. K., & Ghasemi, A. H. (2020). A review of technological improvements in laser-based powder bed fusion of metal printers. *The International Journal of Advanced Manufacturing Technology*, 108(1), 191-209.
131. EOS GmbH, EOS M290 Simply Production of Metal Parts, <https://www.eos.info/en/additive-manufacturing/3d-printing-metal/eos-metal-systems/eos-m-290>
132. FAA Website: www.faa.gov Technical Discipline: Fatigue and Damage Tolerance – Section by Dr. Michael Gorelick, FAA’s Chief Scientific and Technical Advisor for F&DT
133. Shimizu, S., Fujii, H., Sato, Y., Kokawa, H., Sriraman, M., and Babu, S., Mechanism of Weld Formation during Very-high-power Ultrasonic Additive Manufacturing of Al alloy 6061, *Acta Materialia* 74 (2014)
134. Lutjering G, Williams J., *Titanium*. Springer; 2003
135. EOS GmbH, EOS Titanium Ti64 Grade 5 Material Data Sheet
136. Hall J., Fatigue Crack Initiation in alpha-beta Titanium Alloys, *Int. Journal of Fatigue*, 1997
137. Al-Bermani, S., Blackmore, M., Zhang, W. *et al.* The Origin of Microstructural Diversity, Texture, and Mechanical Properties in Electron Beam Melted Ti-6Al-4V. *Metall Mater Trans A* **41**, 3422–3434 (2010).
138. Gouge, M., and Michaleris, P., Autodesk Inc. Netfabb Simulation Capabilities, Recoater Blade Interference, <https://www.metal-am.com/articles/distortion-in-metal-3d-printing-modelling-and-mitigation/>
139. Krasnowski, B., and Viswanathan, S., Design, Analysis and Testing Considerations of Fatigue-Critical Rotorcraft Components, Presented at National Technical Specialists Meeting on Advanced Rotorcraft Structures, AHS, Williamsburg VA, Oct. 1988.
140. Prucha, T. Development of Sand Cast E357 Design Allowables for Incorporation Into MMPDS. (2012)
141. Rae, W., Thermo-metallo-mechanical modelling of heat treatment induced residual stress in Ti-6Al-4V alloy, *Materials Science and Technology*, (2019) 35:7, 747-766
142. Teixeira Ó, Silva FJG, Ferreira LP, Atzeni E. A Review of Heat Treatments on Improving the Quality and Residual Stresses of the Ti-6Al-4V Parts Produced by Additive Manufacturing. *Metals*. 2020; 10(8):1006
143. Zion, L., Safe Life Reliability: Evaluation of New Statistical Methods, Presented at the 47th AHS Annual Forum, May 1991, Phoenix, AZ
144. Titanium Use in Aeroplanes, <https://www.northsteel.com/2018/11/05/titanium-use-in-aeroplanes/>
145. Shayesteh, N., Lecture Slides for Session 3 Additive Manufacturing Process Chain, ME 5390 Class, Advanced Metal Additive Manufacturing Class, Fall 2020, University of Texas at Arlington
146. Cain, V., Thijs, L., Humbeeck, van J., Hooreweder, van B., Knutsen, R., Crack propagation and fracture toughness of Ti6Al4V alloy produced by selective laser melting, *Additive Manufacturing*, Vol 5., 2015 Pages 68-76
147. Kok, Y., Tan, X. P., Wang, P., Nai, M. L. S., Loh, N. H., Liu, E., & Tor, S. B. (2018). Anisotropy and heterogeneity of microstructure and mechanical properties in metal additive manufacturing: A critical review. *Materials & Design*, 139, 565-586.
148. Vrancken, B., Thijs, L., Kruth, J P., Humbeeck, J V., Heat treatment of Ti6Al4V produced by Selective Laser Melting: Microstructure and mechanical properties, *Journal of Alloys and Compounds*, Volume 541, 2012, Pages 177-185

Appendix A – Static Test Result Certificate

Tensile Test Certificate
ASTM E8-21 Rounded Per ASTM E 29-22
Prime: General ID: N/A

Joshua Mocache
AADFW, Inc.
1350 Westpark Way
Eules, TX 76040

Date Issued : 07/26/2022
Lab Number : L22226024
PO Number : VERBAL
Location: AADFW Lab
Date Tested : 02/07/2022
File Number : 0125110-00
Rev Date : Rev: 00

PH: (817) 540-0153

Part #: N/S

Equipment

Tensile: Satec 120 HVL, SN:1290

Method

ASTM E8

REV

21

Bar Type: Round

Yield Criterion: 0.2 % Offset

Gage Length: 1.0 "

Specification: N/A

Rev:

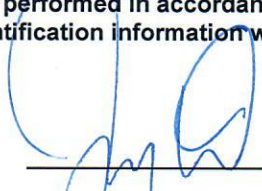
Material:

Elongation: % in 4D

Sample Req:	----- Dimensions (in) -----			---- Ultimate ----		-----Yield -----		Elong	R. A.	Hard.
	Dia.	Dia Final		(lbs)	(ksi)	(lbs)	(ksi)	(pct)	(pct)	
F	0.269	0.267		8746	154	7627	134	1.3	1.5	
NF	0.270	0.243		10633	186	8766	153	8.0	19	

Disposition: For Review Only, based only on test data reported above. Nadcap requirement: Strain Rate prior to yield is .003 - .007 in/in/min; strain rate after yield is approximately .125 in/in/min. I certify that these are accurate and true results of the indicated tests performed in accordance with the AADFW applicable test procedures and relate only to the samples tested. All sample identification information was supplied by the customer.

AADFW, Inc.



Jeremy Wilson, M. Eng., P.E., C.W.I., Metallurgist

Uncertainty of the results is not considered when making pass/fail decision unless otherwise noted. Test specimens and/or unused sample material will be retained for 2 months from date of report, except by prior written agreement. Our letters and reports apply to the sample tested and/or inspected and are not necessarily indicative of the qualities of apparently identical or similar products. All measurements, testing, and opinions are subject to change upon receipt of additional information, testing, or measurements. Reproduction except in full is reserved pending written approval. The recording of false, fictitious, or fraudulent statements or entries on this certificate may be punishable as a felony under Federal law.

Appendix B – Fatigue Test Result Certificate

FATIGUE TEST CERTIFICATE

Page 1 of 1

Attention: Joshua Mocache

To: AADFW, Inc.
1350 Westpark Way
Euless, TX 76040

Phone: (817) 540-0153

Date Issued: 07/21/2022

Lab. Number: L22226024

P.O. Number: 0179230

Date Tested: 04/04/2022

Disk No.: F-0959

File No.: 226024

Rev. Date:

Rev. No.:

Specification: Customer P.O.

Equipment: Satec TC-25, S/N: 1063

Test Method: ASTM F 466 -21

Material: Titanium

Test Results:

"No Flaw" Samples				"Flaw" Samples			
Sample ID	Test Load Max/Min (lbs.)	Fracture Location	Test Duration (cycles)	Sample ID	Test Load Max/Min (lbs.)	Fracture Location	Test Duration (cycles)
1	4500/450	Reduced Section	6,932	1	4500/450	Reduced Section	589
2	3800/380	Reduced Section	9,345	2	4500/450	Reduced Section	1,186
3	2000/200	Reduced Section	84,295	3	2000/200	Reduced Section	12,474
4	1500/150	Reduced Section	180,532	4	1500/150	Reduced Section	38,099
5	500/50	Reduced Section	7,319,219	5	500/50	Reduced Section	3,490,716

Test Speed: 30 Hz

DISPOSITION: For Review Only, based only on test data reported.

I certify that these are accurate and true results of the indicated tests performed in accordance with the AADFW QA Manual and Test Procedures.

AADFW, Inc.  _____ Jeremy Wilson, M. Eng., P.E., C.W.I., Metallurgist